INFORMATION TO USERS

Flexible Dynamic Modeling and Control for the Remote Manipulator System

Xie Haipeng

A Thesis

in

The Department

of

Electrical and Computer Engineering

Presented in Partial Fulfillment of the Requirements

for the Degree of Master of Applied Science at

Concordia University

Montreal, Quebec, Canada

December 1996

The author has granted a non-exclusive licence allowing the National Library of Canada to reproduce, loan, distribute or sell copies of this thesis in microform, paper or electronic formats.

The author retains ownership of the copyright in this thesis. Neither the thesis nor substantial extracts from it may be printed or otherwise reproduced without the author's permission.

L'auteur a accordé une licence non exclusive permettant à la Bibliothèque nationale du Canada de reproduire, prêter, distribuer ou vendre des copies de cette thèse sous la forme de microfiche/film, de reproduction sur papier ou sur format électronique.

L'auteur conserve la propriété du droit d'auteur qui protège cette thèse. Ni la thèse ni des extraits substantiels de celle-ci ne doivent être imprimés ou autrement reproduits sans son autorisation.

0-612-26007-0

Canada

Abstract

Flexible Dynamic Modeling and Control for the Remote Manipulator System

Xie Haipeng

Master of Applied Science (Electrical Engineering)

Concordia University, 1996

This thesis focuses on modeling and controller design for the Space Shuttle Remote Manipulator System (RMS). A dynamic model of the RMS is derived using Book's recursive Lagrangian method. This model has six degree-of-freedom rigid dynamics, joint flexibility dynamics, link transverse elastic dynamics and torsional elastic dynamics. A computationally efficient control approach for addressing joint and boom flexibility of the RMS is investigated. The control strategy consists essentially of four parts. The first part involves pre-shaping the joint trajectories in order to reduce the excitation of link flexibility. The second part is a rigid model based inverse dynamics control which is used to obtain the desired joint torque. The third part is a flexible-joint control loop which is based on a perturbation technique. The last part is a pulse active damping (PAD) control loop which is applied to damp out the system residual vibrations in a fast manner. The integrated control strategy leads to fast end-effector trajectory tracking with less end-effector vibration and fast damping of residual vibrations.

To my mother, XiaoBao, and my father, HongLin

Acknowledgments

I wish to express my profound thanks to Professor Dr. R.V. Patel and Dr. S. Kalaycioglu for their invaluable guidance, significant support and technical assistance during my studies, research work, experiment and creation of this thesis.

Most important, I would like to extend my appreciation to my family and my girlfriend, Cui Jing who have always been a source of strength to me in all of my endeavors.

Contents

List of Figures

List of Tables

Nomenclature

"In-plane" 2D plane which is perpendicular to the motion joint axis

"Out-of-plane" 2D plane on which the motion joint lies

RMS   Remote Manipulator System

a_{i-1} The distance from Z_{i-1} to Z_i measured along X_{i-1}

A_j The joint transformation matrix for joint j

d_i The distance from X_{i-1} to X_i measured along Z_i

E_{j-1} The link transformation matrix for link j-1 between joints j-1 and j

E_{yi} Young's modulus of link i

f_l Link side friction

f_m Servo shaft side friction

G_{si} Shear modulus of link i

J_m Motor shaft inertia

K Gearbox stiffness

k_d Gain factor in link control

k_p Gain factor in link control

k_{pp} Gain factor in joint control

k_v Gain factor in joint control

l_i Length of link i

m_{ai} Mass of link i

m_i Number of elastic modes of link i

N Gear ratio

O_j Coordinate, $[X_j, Y_j, Z_j]$ which is fixed to the joint of link j

$\hat{O}_j$ Coordinate, $[\hat{X}_j, \hat{Y}_j, \hat{Z}_j]$ which is fixed to the distal end of link j, and with no

deflection, $[\hat{X}_j, \hat{Y}_j, \hat{Z}_j]$ is parallel to $[X_j, Y_j, Z_j]$, with X_j coincident with $\hat{X}_j$

$T_r\{M\}$ Trace of matrix M

w_{j-1} Cumulative transformation from base coordinates to O_{j-1} at the joint of link j-1

$\hat{w}_{j-1}$ Cumulative transformation from base coordinates to $\hat{O}_{j-1}$ at the distal end of

link j-1

α_{i-1} The angle between Z_{i-1} and Z_i measured along X_{i-1}

δ_{ij} The jth elastic mode coordinate of link i

Θ_{xi} The torsional elastic deflection of link i

θ_d Commanded joint position at link side

θ_i The angle between X_{i-1} and X_i measured along Z_i

θ_l Joint position measured at link side after gear box

θ_m Joint position measured at motor shaft

μ_i Mass per unit length of link i, $\mu_i = \dfrac{m_{ai}}{l_i}$

ρ_i Mass volume density of link i

τ_l Link side torque

τ_m Motor generated torque

ϕ_{ij} The jth elastic mode shape of link i

φ_{yi} The in-plane elastic deflection of link i

φ_{zi} The out-of-plane elastic deflection of link i

Chapter 1

Introduction

1.1 The Remote Manipulator System (RMS)

Canada designed and developed the Remote Manipulator System (RMS) as part of the Canadian contribution to the NASA Space Shuttle Program in 1974. The project is being undertaken by Canadian industry under contract from the National Research Council of Canada. The RMS is designed for a 10 year, 100 mission operational life. The RMS itself comprises the main portion of the payload deployment and retrieval system of the orbiter. With it, payloads may be extracted from the cargo bay, maneuvered to an appropriate release position and deployed, either automatically or by an operator. Similarly, payloads that have already been deployed in space may be captured and replaced in the cargo bay for servicing or for their subsequent return to earth. Special purpose end-effectors which may be attached to the RMS, also allow the RMS to be utilized in a variety of ancillary functions. RMS can reach and manipulate payloads with masses of up to 65,000lb (29,500 Kg) within a maximum range of 50 feet (15.2 m) from the attach point of the manipulator arm to the orbiter.
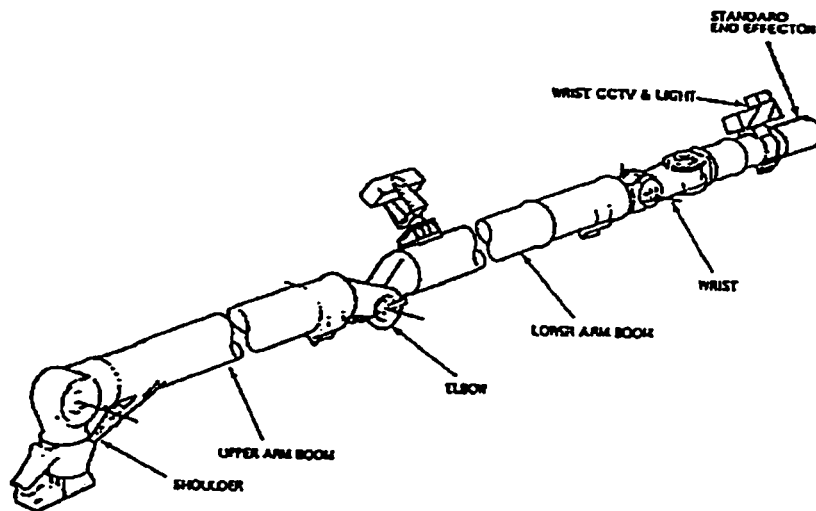
Figure 1.1 Remote manipulator system

As the manipulator arm is only to be operated in the zero-gravity (0-g) environment of space, many of the structural strength requirements which, in a 1-g environment, would need to be imposed to allow the arm to withstand loads due to gravitational forces, can be relaxed. Indeed, the arm cannot support its own weight in a 1-g environment let alone that of a 65,000 lb. (29,500 Kg) mass. Such reductions in strength requirements are, however, accompanied by the generation of unique demands on the manipulator arm control system, which arise from the ensuing, widely-varying dynamic characteristics.

Figure 1.1 shows the schematic of the SRMS. As can be seen there are two long booms from the shoulder pitch to elbow pitch, and from the elbow pitch to the wrist pitch.

The RMS is an electromechanical system. In essence, its mechanical arm assembly consists of two long, hollow links, with circular cross sections, manufactured from a carbon composite material. These links are connected to the orbiter structure through three joints. One is the manipulator positioning mechanism which configures the arm for operation, and the others consist of the shoulder yaw and pitch joints which are controlled during arm

2

manipulation. The links are connected through the elbow pitch joint and are attached, through the wrist pitch, yaw and roll joints to the end-effector with which the target is grasped.

All six orthogonally oriented joints, namely, shoulder yaw, shoulder pitch, elbow pitch, wrist pitch, wrist yaw, and wrist roll are controlled through six D.C. electric servo motors. The motor output-shaft speed is geared down to levels appropriate for the control task by an epicyclic gear train. (The maximum gear ratio, which is that of the shoulder joints, is 1842:1). The control of the manipulator arm is normally through an orbiter general purpose computer in which the control laws reside and which has full control authority.

The light-weight construction used in the design of the joints and the booms cause greater mechanical compliance than typical industrial manipulators. Modal analysis of the vibrational properties of this arm indicates that joint flexibility contributes low frequency modes while higher frequency modes are due to bending of the booms [1].

1.2 Joint and Link Flexibility

Modeling and control of flexible manipulators have received more attention in recent years [4][5][8][25][23]. Most of the work is still at the academic research and/or laboratory experimentation level. The RMS is one of the better known practical examples. Due to its light weight (around 360Kg) and its capability to carry a heavy payload (29,500Kg), there are significant amounts of joint flexibility and link flexibility. This leads to degradation of end-effector tracking.

The methods for modeling flexible-link manipulators can be grouped into a number of categories [12]:

(1) Lagrange's equation and modal expansion
(2) Lagrange's equation and finite elements
(3) Newton-Euler equation and modal expansion

3

(4) Newton-Euler equation and finite elements

(5) Singular perturbation and frequency domain techniques

An accurate finite element model [56], [57], [58] requires an appropriately large number of elements. For multi-link flexible manipulator, the system order of the resulting model can be very high.

The Lagrangian/modal expansion, or Ritz-Kantorovitch method, appears to be the most widely used. In this approach, the deflection of a link is represented as a summation of modes. The modes are products of two terms, a function of the distance along the beam and a function of time

$$w(x, t) = \sum_{i}^{m_i} \phi_i(x)\delta_i(t) \qquad (1.2.1)$$

where x denotes the position along the beam, ϕ_i the mode shape function of position x, δ_i the normal coordinate which is a function of time, t.

Strictly speaking, the summation is infinite ($i=1,...,\infty$). In practice, however, a small number of modes is used, typically $i \le 10$. Introducing higher order modes into a model does not necessarily lead to an improvement in accuracy [12].

Various sets of mode shapes $\phi_i(x)$ can be chosen. However, they must all satisfy the following conditions [33]:

(1) They must form a complete coordinate basis, that is it must be possible to express any link profile in terms of the assumed modes.

(2) They must satisfy the geometric boundary conditions of the system. For flexural vibrations, these boundary conditions correspond to the slope and deflection at the ends of the link.

(3) They must be differentiable over the domain of definition, at least to the degree of the

partial differential equation modeling the flexible arm dynamics.

Functions satisfying these conditions are referred to as admissible functions. In addition to the properties mentioned above, practical mode shapes almost invariably possess certain orthogonality properties with respect to one another which can be used to reduce the number of cross-terms (between the modes) in the model.

Using n modes effectively reduces the distributed parameter system to an nth order discrete system. The total kinetic and potential energies for the arm can be expressed in terms of the mode shapes and modal coordinates. Inserting these terms in Lagrange's equation (1.2.2) and taking the modal coordinates $\delta_i(t)$ as the set of generalized coordinates, leads to a set of coupled differential equations relating the modal responses to the applied forces.

$$\frac{d}{dt}\left(\frac{\partial L}{\partial \dot{q}_i}\right) - \frac{\partial L}{\partial q_i} = \tau_i \qquad (1.2.2)$$

where, L = Kinetic Energy - Potential Energy and q_i is the generalized coordinate.

Euler-Bernoulli beam theory is used almost universally as the starting point for analytic modal models. The assumed modes method can also be applied to multi-link flexible arms. The cantilever modes of the links together with the joint angles, θ_i, provide a suitable set of generalized coordinates. This coordinate basis has the additional advantage of partitioning the rigid-body and flexible dynamics, and the model can be expressed in the form:

$$\begin{bmatrix} M_r & M_c \\ M_c & M_e \end{bmatrix}\begin{bmatrix} \ddot{\theta} \\ \ddot{\delta} \end{bmatrix} + \begin{bmatrix} C_r & C_c \\ C_c & C_e \end{bmatrix}\begin{bmatrix} \dot{\theta} \\ \dot{\delta} \end{bmatrix} + \begin{bmatrix} 0 & 0 \\ 0 & K_e \end{bmatrix}\begin{bmatrix} \theta \\ \delta \end{bmatrix} = \begin{bmatrix} T \\ 0 \end{bmatrix} \qquad (1.2.3)$$

where T is the vector of joint torques. The off-diagonal sub-matrices represent the coupling effects between the rigid-body and elastic dynamics. The elements of the M and C matrices are nonlinear functions of the generalized coordinates and velocities. In general, therefore, the dynamics of a multi-link arm are not only coupled but highly nonlinear.

Book and Cetinkunt [7] provided a recursive algorithm which derives the full nonlinear dynamic equations of multi-link flexible manipulators based on the assumed modes

5

method. The purpose of our model is to simulate the major characteristics of the RMS. However our controller design will not base on this model.

Most controller designs for flexible-link manipulators are based on:

(1) Independent Joint Control under the assumption of rigid links. At present, the RMS basically use independent joint PID control. It is designed based on the fact that the RMS operates in a relatively slow maneuvering motion.

(2) General Rigid Control again assuming rigid links but this time including dynamic interactions between the links. This gives a simple controller design [23] but may not be effective in handling large link flexibility.

(3) Flexible Feedback Control involving feedback of the flexible state variables as well as the joint variables. Some advanced and adaptive control algorithms have been developed [27], [48], [49], [53] and have good control performance. However, these methods have complicate control laws and are computationally expensive.

(4) Signal Pre-Shaping of the trajectory or the control command to reduce the excitation of vibrations. While this approach [39], [43], [44], 29], [30], [34] is highly efficient in reducing excitation of vibrations and is easy implement, the major drawback is its open loop characteristic. The performance depends on a knowledge of the system's natural frequency and damping ratio. Complete filtering can not be achieved for motion with large variations in configuration.

Joint flexibility mostly comes from the gearbox, and is especially serious for harmonic drives which are generally used on systems with high gear ratio requirements such as the RMS. This flexibility is usually modeled as a spring with a stiffness constant K. Nonlinear joint flexibility is not addressed in our model, however, its impact is an open area for research.

Several advanced schemes for controlling joint flexibility have been developed [22] [46]. Some simple and efficient algorithms [14] [9] have also been proposed to control less flexible joints.

1.3 Design Objectives and Motivation

The RMS has been used extensively by the shuttle crew for such tasks as deployment and retrieval of satellites, inspection and servicing of spacecraft and transfer of men and equipment. While the RMS has performed reliably for all of these tasks, because of the presence of flexibility, these operations are sometimes delayed while operators wait for oscillations to die out. In the future, the RMS and similar lightweight flexible arms are likely to play an important role in a variety of demanding on-orbit assembly and maintenance tasks including the construction of the Space Station. In a recent study, it was estimated that the initial phases of space station assembly would require about 47 hours of RMS operation time. Of this total, it was estimated the 30 percent of the cumulative time would be expended to allow the oscillation in the RMS's to die out. Therefore, a controller design which ensures fast and accurate end-point tracking, while exciting less vibration, involving less waiting time, and providing fast damping of residual vibrations is necessary for efficient operation of the RMS.

There are some physical limitations existing for the RMS:

(1) Limit on servo generated torques due to the small size of the servo and limited power supply in space operations, which results in a limit on the motion speed and the use of some "chattering like" control methods.

(2) The small servo and high gear ratios also introduce serious joint flexibility, especially at the shoulder pitch and shoulder yaw joints.

(3) The highly coupled, nonlinear system limits the use of any complicated advanced control method such as adaptive control. Complicated online system identification may not be practical from the point of view of safety and reliability.

All these limitations lead to a requirement that the control should have low computational cost, be continuous and smooth. Several techniques such as signal pre-shaping [39] and perturbation control for flexible joint manipulators [9] are adapted to our design because of their simple implementation and high efficiency. A so called pulse active damping control

7

method which is presently under research for solar panel control is implemented here to rapidly damped out the residual vibrations.

The integrated controller design in this thesis leads to lower end-effector vibrations, and fast damping of residual vibrations. The pulse active damping control approach itself can help the astronaut in damping out the residual vibrations of the RMS and eventually reduce the waiting time in RMS operations.

1.4 Contribution of the Thesis

This thesis addresses a practical problem arising from the need to control vibrations in the RMS as a result of its link and joint elasticity. The main contribution of the thesis are as follow:

(1) In order to accomplish the main objectives of this research, we developed an extensive simulation of the dynamic behavior of the RMS. This simulation models the in--plane, out-of-plane and torsional elasticity of the two long links of the RMS. It is based on the assumed mode approach and uses Book's recursive algorithm.

(2) The control of vibrations in the RMS was achieved by application of control strategies developed using:

�֍ Signal pre-shaping and pulse active damping for reducing / eliminating vibrations due to link flexibility.

✖ A perturbation technique for controlling the effect of joint flexibility.

1.5 Organization of the Thesis

In Chapter 2, the RMS dynamic model is derived by applying Book's Lagrangian Recursive method. The RMS is modeled with three in-plane, three out-of-plane transverse elastic

modes and three torsional elastic modes for each of two long RMS links. Then, some impulse response simulations are done on this dynamic model to demonstrate the effect of link flexibility. In Chapter 3, a control architecture is introduced to handle link flexibility. It consists of two parts, signal pre-shaping on the desired trajectories, and rigid body based inverse dynamics control. Small range movement simulations are carried out at the end of this chapter to verify the proposed control ideas. Chapter 4 introduces the flexible-joint perturbation control algorithm to address RMS's joint flexibility. This control approach is verified by small motion range simulations at the end of Chapter 4. In Chapter 5, a new control algorithm, called Pulse Active Damping control is developed. This attempts to quickly damp out residual vibrations. Some small range movement simulations are also carried out to demonstrate the efficiency and robustness of the proposed control approach. In Chapter 6, a 5000Kg payload transportation task is simulated with the integrated control approach developed previously. The RMS starts from a typical payload retrieval grasping configuration with a 5000Kg payload and transports it back to the cargo bay. For comparison, simulations without Pulse Active Damping are also carried out for the same task.

Chapter 2

A Dynamic Model of the RMS

In modeling the dynamics of the RMS, we adopt Book's recursive Lagrangian method which uses homogeneous transformation matrices to generate full coupled non-linear dynamics of a multi-link flexible manipulator. It models the RMS rigid dynamics, in-plane, out-of-plane transverse link elastic dynamics and torsional elastic dynamics. Some derivation details of the dynamic equations are given in Appendices A-C.

Figure 2.1 shows a block diagram of our model of the RMS. This includes link level and motor shaft level dynamics.

In the following sections, 2.1-2.5, we will apply the Euler-Lagrangian method to derive the RMS link dynamic equations. Euler-Lagrangian equation is given by

$$\frac{d}{dt}\left(\frac{\partial L}{\partial \dot{q}_i}\right) - \frac{\partial L}{\partial q_i} = \tau_i \qquad (2.1)$$

where L = System Kinetic Energy - System Potential Energy

and τ_i denotes the generalized force, q_i the generalized coordinate of the system.
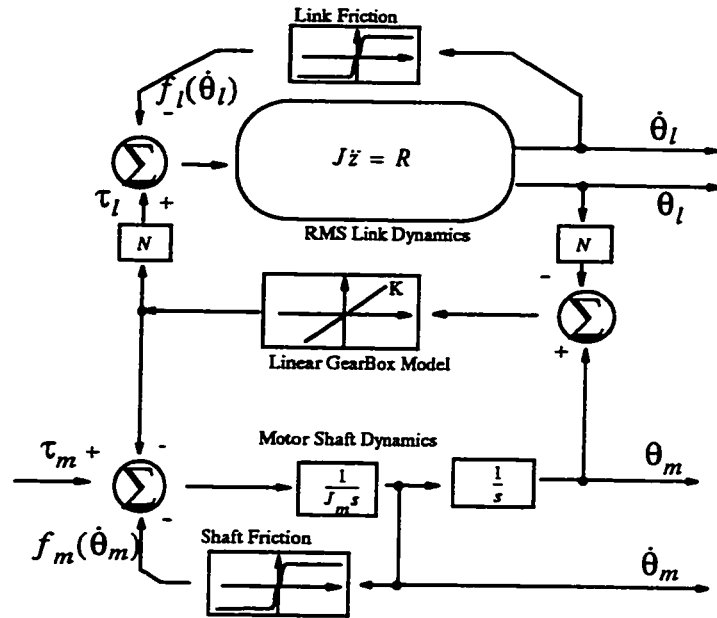
Figure 2.1 RMS dynamic model

Before deriving the system dynamics, we define the system kinematics.

2.1 RMS Kinematic Coordinates

The Denavit-Hartenberg convention [10] is used to describe the kinematics of the RMS. Frame {i} is attached to link i and has its origin lying on joint axis i as shown in Figure 2.2.

The following is a summary of the link frame attachment procedure [10]:

(1) Identify the joint axes and imagine (or draw) infinite lines along them. For steps 2 through 5 below, consider two of these neighboring lines (at axes i and $i+1$).

(2) Identify the common perpendicular between them, or point of intersection. At the point of intersection, or at the point where the common perpendicular meets the ith axis, assign

the link frame origin.

(3) Assign the Z_i axis pointing along the ith joint axis.

(4) Assign the X_i axis pointing along the common perpendicular, or if the axes intersect, assign X_i to be normal to the plane containing the two axes.

(5) Assign the Y_i axis to complete a right-hand coordinate system.

(6) Assign {0} to match {1} when the first joint variable is zero. For {N} choose an origin location and X_N direction freely, but generally so as to cause as many linkage parameters as possible to become zero.
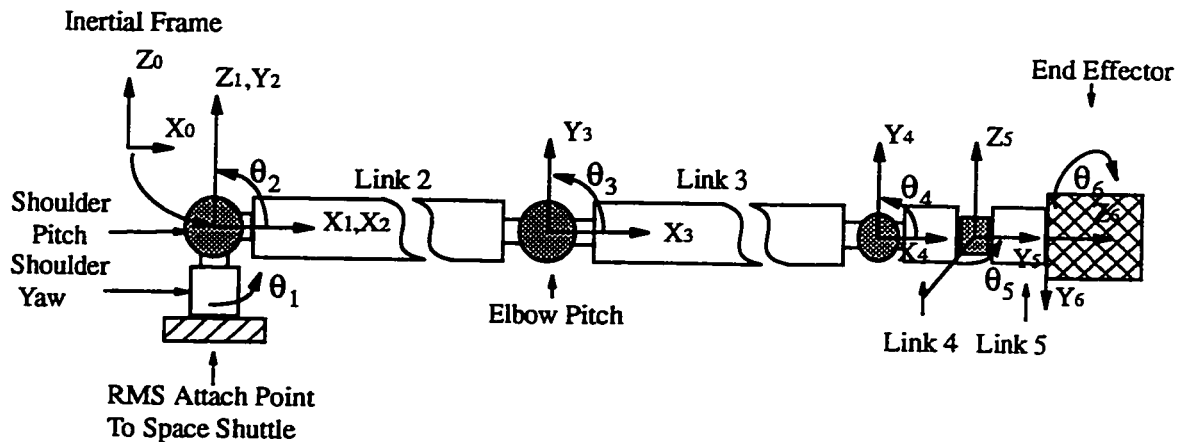
Figure 2.2 RMS kinematic coordinates

With this convention, a table of Denavit Hartenberg parameters is obtained by defining:

α_{i-1} : The angle between Z_{i-1} and Z_i measured along X_{i-1} ;

a_{i-1} : The distance from Z_{i-1} to Z_i measured along X_{i-1} ;

θ_i : The angle between X_{i-1} and X_i measured along Z_i ;

d_i : The distance from X_{i-1} to X_i measured along Z_i ;

Table 2.1 D-H table

i	α_{i-1} (rad)	a_{i-1} (m)	d_i (m)	θ_i (rad)
1	0	0	0	θ_1
2	$\dfrac{\pi}{2}$	0	0	θ_2
3	0	$l_2 = 6.378$	0	θ_3
4	0	$l_3 = 7.062$	0	θ_4
5	$-\dfrac{\pi}{2}$	$l_4 = 0.4572$	0	θ_5
6	$-\dfrac{\pi}{2}$	0	$l_5 = 0.7620$	θ_6
7	0	0	$l_6 = 0.6604$	0

Note: The configuration shown in Figure 2.2 is not at the so called "zero" configuration, instead, θ_5 is equal to $-\dfrac{\pi}{2}$ at the configuration shown.

2.2 Vibration Mode Functions for Elastic Links

The dynamic model developed here is intended to explore the flexible dynamics which result from the light weight arm structure and heavy payload. The assumed mode approach for modeling link flexibilities is adopted here. The two long and less rigid links of RMS (numbered as Link 2 and Link 3 here) are modeled as flexible links. Referring to Figure 2.3, each of these two elastic links is modeled with one rigid, three in-plane, three out-of-plane and three torsional modes, i.e. 9 vibration modes will be used in modeling the

13

elasticity of one flexible link in this model.

By assuming small deflections of the arm, which is valid for the RMS operations, the transverse vibrations can be decoupled into 2 vibration planes, in-plane and out-of-plane, which are perpendicular to each other.
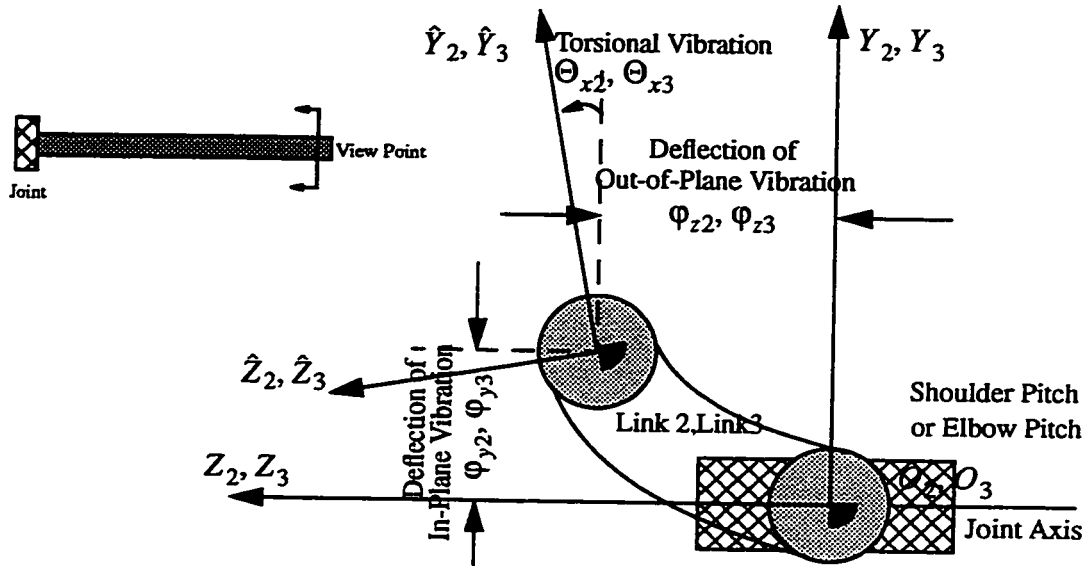
Figure 2.3 Model of elastic deflections
(viewed from end of the link to the joint)

Given that the Z direction is defined to be coincident with the joint axis, we define in-plane vibrations lying in the plane XOY, out-of-plane vibrations lying in the plane XOZ. Three vibration modes will be modeled in each plane for the transverse deflection in our simulation.

Torsional vibrations along X (given the small deflection assumption) is modeled by another three clamped-free vibration modes.

By applying the assumed mode approach to model the link flexibilities[12], [33], [15], the elastic deflection along the link is a function of time and position along the X axis. Referring to Figure 2.3, they are defined in our model as

14

In-plane:

$$\varphi_{yi}(x) = \sum_{j=1}^{3} \phi_{ij}(x)\delta_{ij}(t) \qquad (2.2.1)$$

Out-of-plane:

$$\varphi_{zi}(x) = \sum_{j=4}^{6} \phi_{ij}(x)\delta_{ij}(t) \qquad (2.2.2)$$

Torsional:

$$\Theta_{xi}(x) = \sum_{j=7}^{9} \phi_{ij}(x)\delta_{ij}(t) \qquad (2.2.3)$$

where δ_{ij} denotes the jth generalized coordinate of link i and ϕ_{ij} is the jth mode shape function (admissible function) of link i.

Note: Here, we assign the in-plane vibration modes as the first 3 modes (j=1,2,3), out-of plane vibration modes as the second 3 modes (j=4,5,6), and torsional vibration modes as the last 3 modes (j=7,8,9). This convention applies to the elastic links, i.e., links 2 and 3.

There are several different kinds of admissible functions that can be used in modeling link flexibility [7], [13]. Theoretically, the only constraint on the assumed mode shapes is that they must satisfy the geometric boundary conditions, but not neccessarily the natural boundary conditions nor the governing differential equations. The controlled end of each link, driven by a high gain feedback controller, behaves more like a clamped end. The other end condition of the intermediate links should be approximated by a mass with rotary inertia due to other links of the serial structure and payload. However, for different structures and even for different payloads the resultant simple beam analysis will give different mode shapes. Given the fact that these are natural boundary conditions and will be approximately satisfied even if the assumed mode shapes do not satisfy them, a clamped-free simple beam mode shape would be appropriate for the assumed modes used in the model. "Clamped-free" vibration mode functions assume that the beam vibrates with one end being clamped and the other end free, which gives the following boundary condition

at $x = 0$

$$\phi_i = 0 \qquad\qquad \frac{d\phi_i}{dx} = 0$$

Therefore, we have the transverse vibration "clamped-free" mode functions (for a cantilever beam) as [12], [13]

$$\phi_{ij}(x) = l_i(\cosh\lambda_{ij}x - \cos\lambda_{ij}x - k_{ij}(\sinh\lambda_{ij}x - \sin\lambda_{ij}x)) \qquad (2.2.4)$$

where

$$k_{ij} = \frac{\cos\lambda_{ij}l_i + \cosh\lambda_{ij}l_i}{\sin\lambda_{ij}l_i + \sinh\lambda_{ij}l_i} \qquad (2.2.5)$$

and λ_{ij} 's are the roots of

$$1 + \cos\lambda_{ij}l_i\cosh\lambda_{ij}l_i = 0 \qquad (2.2.6)$$

This gives the following natural frequencies for link i

$$\omega_{ij} = (\lambda_{ij}l_i)^2\sqrt{\frac{E_{yi}I_i}{\mu_i l_i}} = (\lambda_{ij}l_i)^2\sqrt{\frac{E_{yi}I_i}{m_{ai}l_i^3}} \qquad j = 1...3 \qquad (2.2.7)$$

where $\mu_i = \dfrac{m_{ai}}{l_i}$ denotes the mass per unit length of link i, m_{ai} the mass of link i, l_i the length of link i, E_{yi} Young's modulus of link i.

Mode shape functions also satisfy the orthogonality condition

$$\frac{1}{2}\int_0^{l_i}\phi_{ij}(x)\phi_{ik}(x)\mu_i dx = \frac{1}{2}\mu_i l_i^3\zeta_{jk} \qquad \zeta_{jk} = \begin{cases} 1 & j = k \\ 0 & j \ne k \end{cases} \qquad (2.2.8)$$

By assuming that the structural characteristics of each elastic link are identical in the Y

16

and Z directions, we choose identical mode shape function sets for in-plane and out-of-plane vibrations for one link, i.e., $\phi_{i1} = \phi_{i4}, \phi_{i2} = \phi_{i5}, \phi_{i3} = \phi_{i6}$.

Torsional vibration mode shape functions have the form

$$\phi_{ij} = \sin \omega_{ij} t \left\{ A_{ij} \sin \left(\omega_{ij} x \sqrt{\frac{\rho_i}{G_{si}}} \right) + B_{ij} \cos \left(\omega_{ij} x \sqrt{\frac{\rho_i}{G_{si}}} \right) \right\} \qquad (2.2.9)$$

where $\rho_i = \dfrac{m_{ai}}{v_i}$ is the mass volume density, G_{si} the shear modulus of material of link i.

With the "clamped-free" assumption, we have

$$\omega_{ij} l_i \sqrt{\frac{\rho_i}{G_{si}}} = \left(j - 7 + \frac{1}{2} \right) \pi \qquad j = 7...9 \qquad (2.2.10)$$

$$B_{ij} = 0 \qquad A_{ij} = 1$$

Therefore, the torsional deflections in (2.2.3) can be described as

$$\Theta_{xi} = \sum_{j=7}^{9} \delta_{ij}(t) \sin \left(\omega_{ij} x \sqrt{\frac{\rho_i}{G_{si}}} \right) = \delta_{i7} \sin \left(\frac{\pi x}{2 l_i} \right) + \delta_{i8} \sin \left(\frac{3 \pi x}{2 l_i} \right) + \delta_{i9} \sin \left(\frac{5 \pi x}{2 l_i} \right)$$

$$(2.2.11)$$

2.3 Extended D-H 4X4 Homogeneous Transformations

The kinematics described by the conventional Denavit and Hartenberg 4X4 homogeneous transformation matrices do not involve the link deflection caused by bending. We need to extend the conventional D-H 4X4 homogeneous transformation matrix notation to deformational kinematics of flexible links connected by rotary joints. The transformation due to the joint is separated from the one due to the flexible link as shown in Figure 2.4.

The position of a point on link i is given by

$$^{0}h_i(x) = {}^{0}w_i {}^{i}h_i(x)$$
$$^{0}w_i = {}^{0}w_{i-1}E_{i-1}A_i$$

(2.3.1)

where:

A_j is the joint transformation matrix for joint j;

E_{j-1} is the link transformation matrix for link $j-1$ between joints $j-1$ and j;

$\hat{w}_{j-1}$ is the cumulative transformation from base coordinates to $\hat{O}_{j-1}$ at the distal end of link j-1;

w_{j-1} is the cumulative transformation from base coordinates to O_{j-1} at the joint of link j-1;

The origin $\hat{O}_j$ of coordinate system $[\hat{X}_j, \hat{Y}_j, \hat{Z}_j]$ is fixed to the distal end of link j;

The origin O_j of coordinate system $[X_j, Y_j, Z_j]$ is fixed to the joint of link j, and with no deflection, $[\hat{X}_j, \hat{Y}_j, \hat{Z}_j]$ is parallel to $[X_j, Y_j, Z_j]$, with X_j coincident with $\hat{X}_j$.
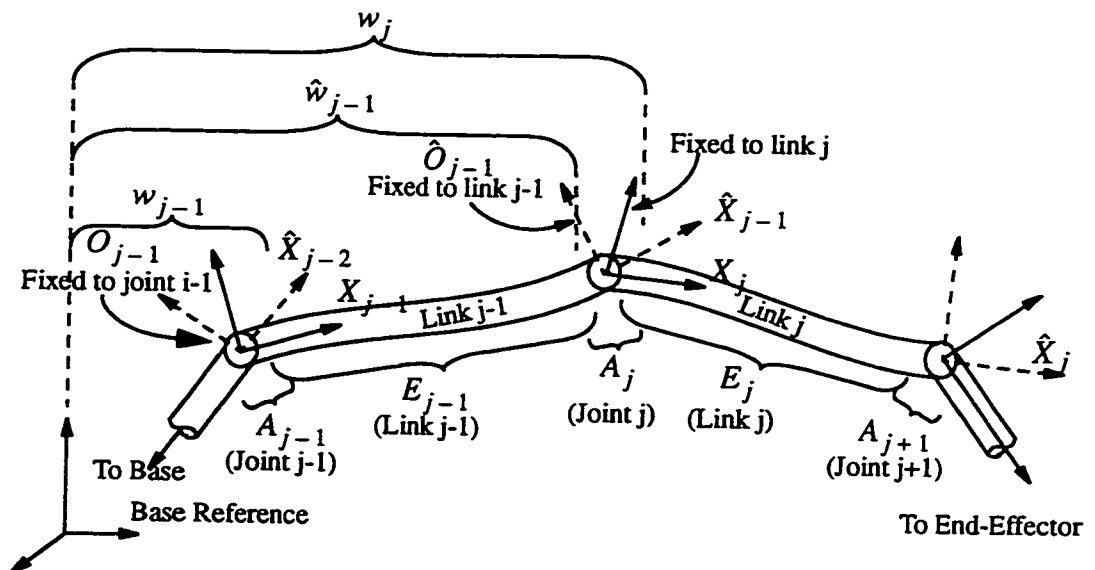
Figure 2.4 Joint transformation and flexible-link transformation

Incorporating the deflection,

$$
{}^{i}h_i(x) = \begin{bmatrix} x \\ 0 \\ 0 \\ 1 \end{bmatrix} + \sum_{j=1}^{m_i} \delta_{ij}(t) \begin{bmatrix} x_{ij}(x) \\ y_{ij}(x) \\ z_{ij}(x) \\ 0 \end{bmatrix}
\qquad (2.3.2)
$$

where

x_{ij}, y_{ij}, z_{ij} denote the displacement components of mode j of link i in the X, Y, Z directions respectively;

δ_{ij} denotes the elastic coordinate of mode j of link i;

m_i is the number of modes used to describe the elastic deflection of link i, i.e., $m_i = 9$ in our model for $i = 2, 3$

Assuming small deflections, here we only model the two long links as flexible links, i.e., i=2,3. The transverse deflections are modeled as in-plane and out-of-plane vibrations, so that the displacement component of mode j of link i can be described as

$$
x_{ij}(x) = 0
$$

$$
y_{ij}(x) = \phi_{ij}(x) \qquad\qquad j = 1, 2, 3
$$

$$
z_{ij}(x) = \phi_{ij}(x) \qquad\qquad j = 4, 5, 6 \qquad (2.3.3)
$$

The link transformation E_i incorporates the link deflection of link i

$$
E_i = \begin{bmatrix} 1 & 0 & 0 & l_i \\ 0 & 1 & 0 & 0 \\ 0 & 0 & 1 & 0 \\ 0 & 0 & 0 & 1 \end{bmatrix} + \sum_{j=1}^{m_i} \delta_{ij}(t) \begin{bmatrix} 0 & -\Theta_{zij} & \Theta_{yij} & x_{ij} \\ \Theta_{zij} & 0 & -\Theta_{xij} & y_{ij} \\ -\Theta_{yij} & \Theta_{xij} & 0 & z_{ij} \\ 0 & 0 & 0 & 0 \end{bmatrix}
\qquad (2.3.4)
$$

where all variables in bracket are evaluated at $x = l_i$ and $\Theta_{xij}, \Theta_{yij}, \Theta_{zij}$ are rotational

components along X, Y, Z of link i, respectively.

In our model

$$\Theta_{zi}(l_i) = \frac{\partial}{\partial x} w_{yi}(x)\bigg|_{x = l_i} = \sum_{j=1}^{3} \phi_{ij}'(x)\big|_{x = l_i} \delta_{ij}(t) = \sum_{j=1}^{3} \Theta_{zij}\delta_{ij}(t) \qquad (2.3.5)$$

$$\Theta_{yi}(l_i) = -\frac{\partial}{\partial x} w_{zi}(x)\bigg|_{x = l_i} = -\sum_{j=4}^{6} \phi_{ij}'(x)\big|_{x = l_i} \delta_{ij}(t) = -\sum_{j=4}^{6} \Theta_{yij}\delta_{ij}(t) \qquad (2.3.6)$$

$$\Theta_{xi}(l_i) = \sum_{j=7}^{9} \phi_{ij}(x)\big|_{x = l_i} \delta_{ij}(t) = \sum_{j=7}^{9} \Theta_{xij}\delta_{ij}(t) \qquad (2.3.7)$$

Links 1,4,5 and 6 are assumed to be rigid. Therefore, for these joints, we have link transformations

$$E_1 = \begin{bmatrix} 1 & 0 & 0 & 0 \\ 0 & 1 & 0 & 0 \\ 0 & 0 & 1 & 0 \\ 0 & 0 & 0 & 1 \end{bmatrix} \quad E_4 = \begin{bmatrix} 1 & 0 & 0 & l_4 \\ 0 & 1 & 0 & 0 \\ 0 & 0 & 1 & 0 \\ 0 & 0 & 0 & 1 \end{bmatrix} \quad E_5 = \begin{bmatrix} 1 & 0 & 0 & 0 \\ 0 & 1 & 0 & l_5 \\ 0 & 0 & 1 & 0 \\ 0 & 0 & 0 & 1 \end{bmatrix} \quad E_6 = \begin{bmatrix} 1 & 0 & 0 & 0 \\ 0 & 1 & 0 & 0 \\ 0 & 0 & 1 & l_6 \\ 0 & 0 & 0 & 1 \end{bmatrix} \qquad (2.3.8)$$

For all joints, we have joint transformations

$$A_i = \begin{bmatrix} \cos\theta_i & -\sin\theta_i & 0 & 0 \\ \sin\theta_i\cos\alpha_{i-1} & \cos\theta_i\cos\alpha_{i-1} & -\sin\alpha_{i-1} & 0 \\ \sin\theta_i\sin\alpha_{i-1} & \cos\theta_i\sin\alpha_{i-1} & \cos\alpha_{i-1} & 0 \\ 0 & 0 & 0 & 1 \end{bmatrix} \qquad (2.3.9)$$

The overall forward kinematics can be written as

$$^0h_6(x) = A_1 E_1 A_2 E_2 A_3 E_3 A_4 E_4 A_5 E_5 A_6 {}^6h_6(x)$$

20

2.4 Kinetic & Potential Energy

In order to apply Lagrange's equation (2.1) to derive the RMS dynamic equations, we need to find out the kinetic and potential energy of the system first.

Kinetic Energy

The system kinetic energy consists of translational kinetic energy and rotational kinetic energy, i.e.,

$$K_{total} = K_{translational} + K_{rotational}$$

The derivation details of the equations are given in Appendix A. From Appendix A, we obtain the total kinetic energy of the system in the form

$$K_{Total} = \sum_{i=1}^{n} T_r \{ \dot{w}_i B_{3i} \dot{w}_i^T + 2\dot{w}_i B_{2i} w_i^T + w_i B_{1i} w_i^T \} \tag{2.4.1}$$

where T_r denotes "trace" of matrix. For the flexible links, (links 2 and 3)

$$B_{1i} = \sum_{j=1}^{m_i} \sum_{k=1}^{m_i} \dot{\delta}_{ij} \dot{\delta}_{ik} C_{ikj} \tag{2.4.2}$$

$$C_{ikj} = \frac{1}{2} \int_0^{l_i} \mu_i \begin{bmatrix} 0 & x_{ik} & y_{ik} & z_{ik} \end{bmatrix}^T \begin{bmatrix} 0 & x_{ik} & y_{ik} & z_{ik} \end{bmatrix} dx \tag{2.4.3}$$

$$B_{2i} = \sum_{j=1}^{m_i} \dot{\delta}_{ij} C_{ij} + \sum_{k=1}^{m_i} \sum_{j=1}^{m_i} \delta_{ik} \dot{\delta}_{ij} C_{ikj} \tag{2.4.4}$$

$$C_{ij} = \frac{1}{2} \int_0^{l_i} \mu_i \begin{bmatrix} 1 & x & 0 & 0 \end{bmatrix}^T \begin{bmatrix} 0 & x_{ik} & y_{ik} & z_{ik} \end{bmatrix} dx \tag{2.4.5}$$

21

$$B_{3i} = C_i + \sum_{j=1}^{m_i} \delta_{ij}[C_{ij} + C_{ij}^T] + \sum_{k=1}^{m_i} \sum_{j=1}^{m_i} \delta_{ik}\delta_{ij}C_{ikj} \qquad (2.4.6)$$

and for all rigid links (links 1,4,5 and 6), we have

$$B_{1i}, B_{2i} = 0$$

$$B_{3i} = C_i = \frac{1}{2}\int_v \rho_i \, {}^i h_i \, {}^i h_i^T dv = \frac{1}{2}\int_v \rho_i \begin{bmatrix} x \\ y \\ z \\ 1 \end{bmatrix} \begin{bmatrix} x & y & z & 1 \end{bmatrix} dv = \frac{\rho_i}{2}\int_v \begin{bmatrix} x^2 & xy & xz & x \\ xy & y^2 & yz & y \\ xz & yz & z^2 & z \\ x & y & z & 1 \end{bmatrix} dv \quad (2.4.7)$$

Potential Energy

The system potential energy is derived in Appendix B, from where, we have

$$V_e = \frac{1}{2}\sum_{i=2}^{3}\sum_{j=1}^{9} K_{ij}\delta_{ij}^2 \qquad (2.4.8)$$

where

$$K_{ij} = \int_0^{l_i} E_{yi}I_{zi}(\phi_{ij}''(l_i))^2 dx \qquad j = 1, 2, 3 \qquad (2.4.9)$$

$$K_{ij} = \int_0^{l_i} E_{yi}I_{yi}(\phi_{ij}''(l_i))^2 dx \qquad j = 4, 5, 6 \qquad (2.4.10)$$

$$K_{ij} = \int_0^{l_i} G_{si}I_{xi}(\phi_{ij}'(l_i))^2 dx \qquad j = 7, 8, 9 \qquad (2.4.11)$$

2.5 Dynamic Equations

By applying the Euler-Lagrangian equation (2.1), we finally obtain the RMS link dynamic equations. Details of the derivation are given in Appendix C.

$$\frac{d}{dt}\left(\frac{\partial K_{total}}{\partial \dot{\theta}_j}\right) - \frac{\partial K_{total}}{\partial \theta_j} = \sum_{i=j}^{n} 2Tr\left\{\frac{\partial w_i}{\partial \theta_j}\left[\left[C_i + \sum_{j=1}^{m_i} \delta_{ij}\left(C_{ij} + C_{ij}^T + \sum_{k=1}^{m_i} \delta_{ik}C_{ikj}\right)\right]\ddot{w}_i^T + \right.\right.$$

$$\left.\left.\left[\sum_{j=1}^{m_i} \ddot{\delta}_{ij}\left(C_{ij} + \sum_{k=1}^{m_i} \delta_{ik}C_{ikj}\right)\right]w_i^T + \left[2\sum_{j=1}^{m_i} \dot{\delta}_{ij}\left(C_{ij} + \sum_{k=1}^{m_i} \delta_{ik}C_{ikj}\right)\right]\dot{w}_i^T\right]\right\}$$

$$= \sum_{i=j}^{n} 2T_r\left\{\frac{\partial w_i}{\partial \theta_j}\left[G_i\ddot{w}_i^T + \sum_{k=1}^{m_i} \ddot{\delta}_{ik}D_{ik}w_i^T + 2\sum_{k=1}^{m_i} \dot{\delta}_{ik}D_{ik}\dot{w}_i^T\right]\right\} \qquad (2.5.1)$$

where

$$D_{ij} = C_{ij} + \sum_{k=1}^{m_i} \delta_{ik}C_{ikj} \qquad (2.5.2)$$

and

$$G_i = C_i + \sum_{j=1}^{m_i} \delta_{ij}\left(C_{ij} + C_{ij}^T + \sum_{k=1}^{m_i} \delta_{ik}C_{ikj}\right) \qquad (2.5.3)$$

and

$$\frac{d}{dt}\left(\frac{\partial K_{total}}{\partial \dot{\delta}_{jf}}\right) - \frac{\partial K_{total}}{\partial \delta_{jf}} = 2\sum_{i=j+1}^{n} T_r\left\{\frac{\partial w_i}{\partial \delta_{jf}}\left[G_i\ddot{w}_i^T + \sum_{k=1}^{m_i} \ddot{\delta}_{ik}D_{ik}w_i^T + 2\sum_{k=1}^{m_i} \dot{\delta}_{ik}D_{ik}\dot{w}_i^T\right]\right\}$$

$$+ T_r\left\{2\left[\ddot{w}_jD_{jf} + 2\dot{w}_j\sum_{k=1}^{m_i} \dot{\delta}_{jk}C_{jkf} + w_j\sum_{k=1}^{m_i} \ddot{\delta}_{jk}C_{jkf}\right]w_j^T\right\}$$

$$(2.5.4)$$

The part contributed by potential energy in (2.1) is

$$\frac{\partial V_e}{\partial \delta_{im}} = K_{im}\delta_{im} \qquad i = 2, 3 \qquad (2.5.5)$$

Next, we apply the Euler Lagrange equation(2.1) where $L = K_{total} - V_e$. If we separate

23

(2.1) into two groups according to the type of coordinates on which the differentiation is applied, we can have one group of equations where the differentiation is applied on rigid coordinates θ_j and the other group of equations where the differentiation is applied on elastic coordinates δ_{jf}.

Joint Equations "*j*"

Where the differentiation is applied on rigid coordinates θ_j, RMS is a six joint robot, we have $j = 1...6$

$$\frac{d}{dt}\left(\frac{\partial K_{total}}{\partial \dot{\theta}_j}\right) - \frac{\partial K_{total}}{\partial \theta_j} + \frac{\partial V_e}{\partial \theta_j} = F_j \qquad (2.5.6)$$

Deflection Equations "*jf*"

where the differentiation is applied on elastic δ_{jf}.

Since link 2 and link 3 are the only flexible links in our model, $j = 2, 3$ and $f = 1...9$

$$\frac{d}{dt}\left(\frac{\partial K_{total}}{\partial \dot{\delta}_{jf}}\right) - \frac{\partial K_{total}}{\partial \delta_{jf}} + \frac{\partial V_e}{\partial \delta_{jf}} = 0 \qquad (2.5.7)$$

We can re-write (2.5.6) and (2.5.7) by collecting all the $\ddot{\theta}, \ddot{\delta}$ terms so that (2.5.6) becomes

$$\sum_{h=1}^{6} J_{jh}\ddot{\theta}_h + \sum_{l=1}^{9} J_{j2l}\ddot{\delta}_{2l} + \sum_{l=1}^{9} J_{j3l}\ddot{\delta}_{3l} = R_j \qquad j = 1...6$$

$$(2.5.8)$$

and (2.5.7) becomes

$$\sum_{h=1}^{6} J_{2fh}\ddot{\theta}_h + \sum_{l=1}^{9} J_{2f2l}\ddot{\delta}_{2l} + \sum_{l=1}^{9} J_{2f3l}\ddot{\delta}_{3l} = R_{2f} \qquad f = 1...9$$

$$\sum_{h=1}^{6} J_{3fh}\ddot{\theta}_h + \sum_{l=1}^{9} J_{3f2l}\ddot{\delta}_{2l} + \sum_{l=1}^{9} J_{3f3l}\ddot{\delta}_{3l} = R_{3f} \qquad f = 1...9$$

$$(2.5.9)$$

We write the complete dynamics equations in the form

$$J\ddot{z} = R$$

where the inertial matrix

$$J = \begin{bmatrix} \begin{bmatrix} J_{11} & J_{12} & \cdots & J_{16} \\ J_{21} & J_{22} & & \\ \vdots & & & \\ J_{61} & & & J_{66} \end{bmatrix} & \begin{bmatrix} J_{121} & J_{122} & \cdots & J_{129} \\ J_{221} & & & \\ \vdots & & & \\ J_{621} & & & J_{629} \end{bmatrix} & \begin{bmatrix} J_{131} & J_{132} & \cdots & J_{139} \\ J_{231} & & & \\ \vdots & & & \\ J_{631} & & & J_{639} \end{bmatrix} \\ \begin{bmatrix} J_{211} & J_{212} & \cdots & J_{216} \\ J_{221} & & & \\ \vdots & & & \\ J_{291} & & & J_{296} \end{bmatrix} & \begin{bmatrix} J_{2121} & J_{2122} & \cdots & J_{2129} \\ J_{2221} & & & \\ \vdots & & & \\ J_{2921} & & & J_{2929} \end{bmatrix} & \begin{bmatrix} J_{2131} & J_{2132} & \cdots & J_{2139} \\ J_{2231} & & & \\ \vdots & & & \\ J_{2931} & & & J_{2939} \end{bmatrix} \\ \begin{bmatrix} J_{311} & J_{312} & \cdots & J_{316} \\ J_{321} & & & \\ \vdots & & & \\ J_{391} & & & J_{396} \end{bmatrix} & \begin{bmatrix} J_{3121} & J_{3122} & \cdots & J_{3129} \\ J_{3221} & & & \\ \vdots & & & \\ J_{3921} & & & J_{3929} \end{bmatrix} & \begin{bmatrix} J_{3131} & J_{3132} & \cdots & J_{3139} \\ J_{3231} & & & \\ \vdots & & & \\ J_{3931} & & & J_{3939} \end{bmatrix} \end{bmatrix}$$

$$(2.5.10)$$

and z is the vector of the generalized coordinates

$$z = [\theta_1, \theta_2, \theta_3, \theta_4, \theta_5, \theta_6, \delta_{21}, \delta_{22}, ..., \delta_{29}, \delta_{31}, \delta_{32}, ..., \delta_{39}]^T$$

The term R is of the form $R = [R_1, R_2, R_3, R_4, R_5, R_6, R_{21}, R_{22}, ..., R_{29}, R_{31}, ..., R_{39}]^T$ which contains the remaining dynamics.

Inertia coefficients of joint variables in the joint equations

The coefficients of $\ddot{\theta}_h$ in joint equation "j" are

$$J_{jh} = 2T_r\{\hat{w}_{j-1}U_j{}^{j}\tilde{F}_h U_h^T \hat{w}_{h-1}^T\} \qquad (2.5.11)$$

where ${}^{j}\tilde{F}_h = \sum_{i=max(h,j)}^{n} ({}^{j}\tilde{w}_i G_i{}^{h}\tilde{w}_i^T)$ and $U_j = \dfrac{\partial A_j}{\partial \theta_j}$.

Inertial coefficients of the deflection variables in the joint equations

The coefficients of $\ddot{\delta}_{hl}$ in joint equation "j"

(1) $h = 2, 3, \ j = 1...h$

$$J_{jhl} = 2T_r\{\hat{w}_{j-1}U_j({}^{j}F_h M_{hl}^T + {}^{j}\tilde{w}_h D_{hl})w_h^T\} \qquad (2.5.12)$$

where ${}^{j}F_n = \sum_{i=max(h+1,j)}^{n} ({}^{j}\tilde{w}_i G_i{}^{h}w_i^T)$

(2) $h = 2, 3, \ j = h+1...n$

$$J_{jhl} = 2\sum_{i=max(h+1,j)}^{n} T_r\left\{\frac{\partial w_i}{\partial \theta_j}G_i(w_h M_{hl}{}^{h}w_i\ddot{\delta}_{hl})^T\right\} = 2T_r\{\hat{w}_{j-1}U_j[{}^{j}F_h M_{hl}^T w_h^T]\}$$

$$(2.5.13)$$

Note: The inertia coefficients for joint variables $\ddot{\theta}_j$ in the deflection equation "hl" are the same as the inertia coefficients for $\ddot{\delta}_{hl}$ in the joint equation j due to the symmetry property of inertial matrix J, i.e., $J_{jhl} = J_{hlj}$.

Inertia coefficients of the deflection variables in the deflection equations

The coefficients of δ_{hk} in deflection equation "jf"

(1) $j = h = 2, 3$

$$J_{jfhk} = 2T_r\{w_j M_{jf} {}^j\Phi_j M_{jk}^T w_j^T + C_{jkf}\} \qquad (2.5.14)$$

where ${}^j\Phi_h = \sum_{i = max(h+1, j+1)}^{n} {}^j w_i G_i^{\ h} w_i^T$

(2) $j = 2, h = 3$

$$J_{jfhk} = 2\dot{T}_r\{w_j M_{jf} ({}^j\Phi_h M_{hk}^T + {}^j w_h D_{hk}) w_h^T\} \qquad (2.5.15)$$

Due to the symmetry property of inertial matrix J, we have $J_{jfhk} = J_{hkjf}$.

The remaining dynamics in (2.5.9)

$$R_1 = -2T_r\{u_1 Q_1\} + F_1 \qquad (2.5.16)$$

$$R_j = -2T_r\{\hat{w}_{j-1} u_j Q_j\} + F_j \qquad j = 2\ldots6 \qquad (2.5.17)$$

with

$$Q_n = G_n \ddot{w}_{vn}^T + 2\left(\sum_{k=1}^{m_n} \dot{\delta}_{nk} D_{nk}\right) \dot{w}_n^T \qquad (2.5.18)$$

$$Q_j = G_j \ddot{w}_{vj}^T + 2\left(\sum_{k=1}^{m_j} \dot{\delta}_{jk} D_{jk}\right) \dot{w}_j^T + E_j A_{j+1} Q_{j+1} \qquad (2.5.19)$$

and

$$R_{jf} = -2T_r\left\{w_j M_{jf} A_{j+1} Q_{j+1} + \left[\ddot{w}_{vj} D_{jf} + 2\dot{w}_j \sum_{k=1}^{m_i} \dot{\delta}_{jk} C_{jkf}\right] w_j^T\right\} - \delta_{jf} K_{jf}$$

$$j = 2, 3 \qquad f = 1\ldots9 \qquad (2.5.20)$$

2.6 Demonstration of the RMS Link Flexibility

To demonstrate the effect of link flexibility, we apply an impulse torque signal at the shoulder yaw while locking all other joints of the RMS in two of the three typical configurations of the RMS (as shown in Figure 2.5, 2.6 and 2.7) without payload, with 500Kg payload and with 29,500Kg payload. The same simulation is repeated for shoulder pitch and elbow pitch. We consider three typical configurations of the RMS:

Configuration A: All links are extended, the distance from the arm attachment point to the end-effector is at its maximum.

Configuration A: $\qquad \theta = \left[0, 0, 0, 0, -\frac{\pi}{2}, 0 \right]$
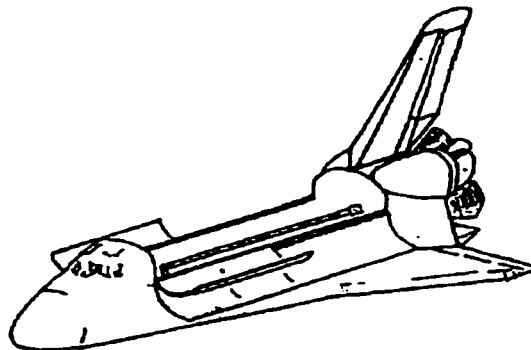
Figure 2.5 RMS Configuration A

Configuration B: The arm is in a typical payload grappling configuration with the effector positioned over the orbiter cockpit overhead window.

Configuration B: $\theta = \left[\dfrac{\pi}{2}, \dfrac{2\pi}{3}, -\dfrac{2\pi}{3}, 0, -\dfrac{\pi}{2}, 0\right]$

Figure 2.6 RMS Configuration B

Configuration C: The end-effector is at the point corresponding to where the payload would be placed in the cargo bay.

Configuration C: $\theta = \left[\dfrac{\pi}{4}, \dfrac{\pi}{3}, -\dfrac{\pi}{2}, 0, -\dfrac{\pi}{2}, 0\right]$
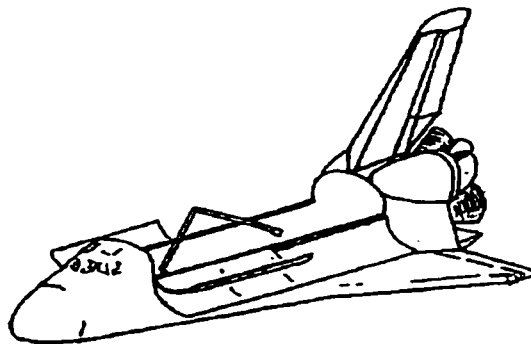
Figure 2.7 RMS Configuration C

At Configuration A, without payload and with *the Shoulder Yaw* being excited, the simulation results are plotted in Figure 2.8.a showing the end-effector displacement (with respect to the inertial frame) in the Y direction, and in Figure 2.8.b showing the first "out-of-plane" transverse vibration coordinates for elastic links, i.e., δ_{24}, δ_{34} which are excited by the Shoulder Yaw joint motion.

Figure 2.8.a Without payload, Shoulder Yaw excited, end-effector displacements in Y direction
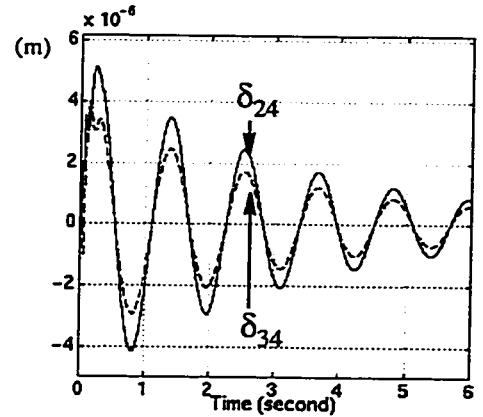
Figure 2.8.b Without payload, Shoulder Yaw excited, "out-of-plane" first vibration mode coordinates for links 2 and 3

The simulation results in configuration A without payload with *Shoulder Pitch* being excited are plotted in Figure 2.9.a showing the end-effector displacement (with respect to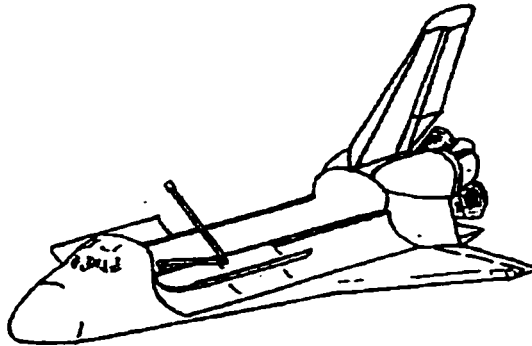 the inertial frame) in the Z direction, and in Figure 2.9.b showing the first "in-plane" transverse vibrations coordinates for elastic links, i.e., δ_{21}, δ_{31}, which are excited by the Shoulder Pitch joint motion.

Figure 2.9.a Without payload, Shoulder Pitch excited, end-effector displacements in Z direction
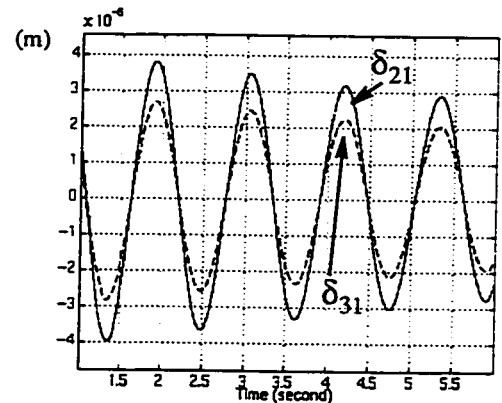
Figure 2.9.b Without payload, Shoulder Pitch excited, "in-plane" first vibration mode coordinates for links 2 and 3

30

When carrying a 500Kg payload (point mass), in Configuration A, the simulation results are plotted in Figure 2.10.a, and Figure 2.10.b for Shoulder Yaw excitation and in Figure 2.11.a, and Figure 2.11.b for Shoulder Pitch excitation.
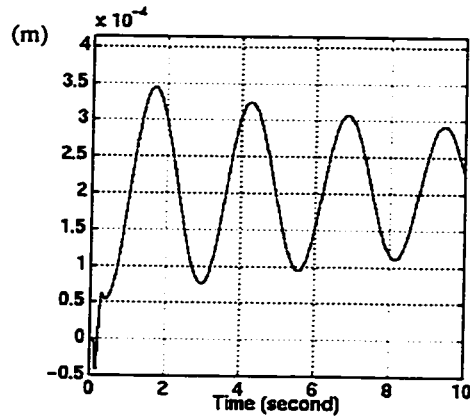
Figure 2.10.a With 500Kg payload, Shoulder Yaw excited, end-effector displacements in Y direction
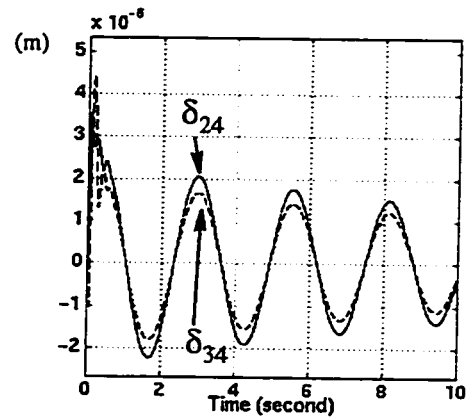
Figure 2.10.b With 500Kg payload, Shoulder Yaw excited, "out-of- plane" first vibration mode coordinates for links 2 and 3
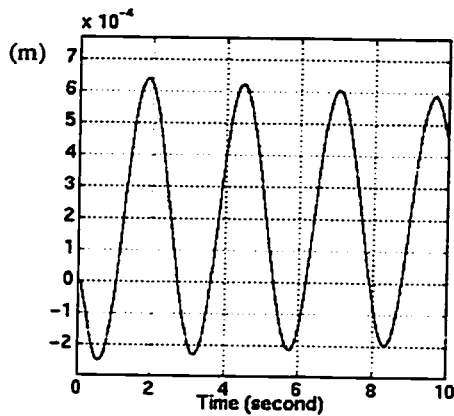
Figure 2.11.a With 500Kg payload, Shoulder Pitch excited, end-effector displacements in Z direction
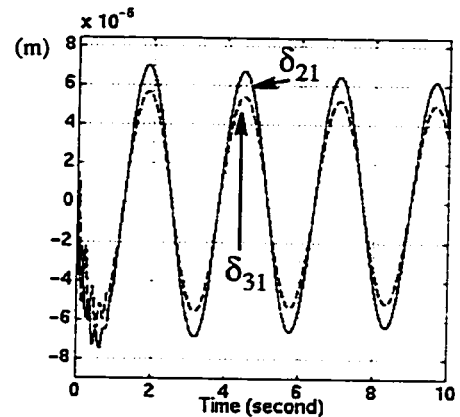
Figure 2.11.b With 500Kg payload, Shoulder Pitch excited, "in- plane" first vibration mode coordinates for links 2 and 3

When carrying a 29,500Kg payload (point mass), in Configuration A, the simulation results are plotted in Figure 2.12.a and Figure 2.12.b for Shoulder Yaw excitation, and in Figure 2.13.a and Figure 2.13.b for Shoulder Pitch excitation.
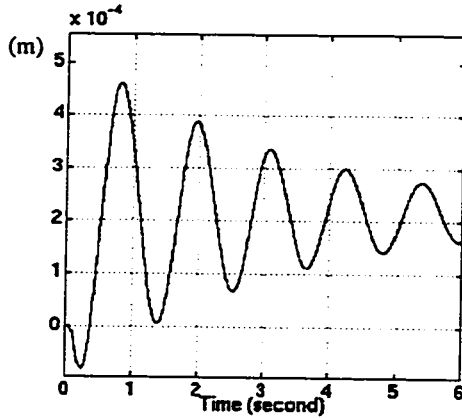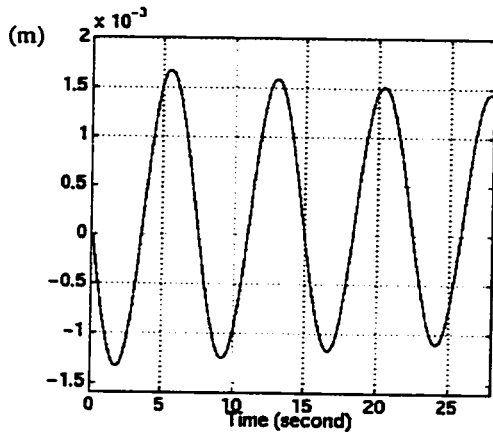
Figure 2.12.a With 500Kg payload, Shoulder Yaw excited, end-effector displacements in Y direction
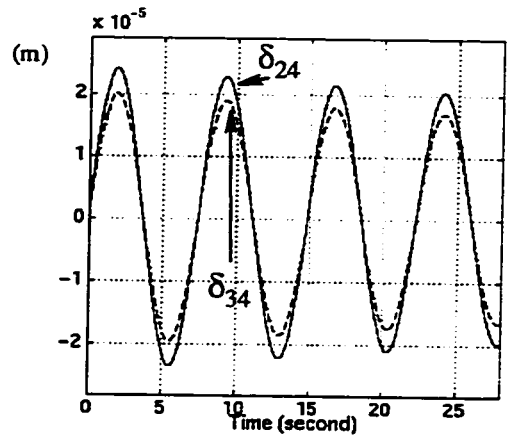
Figure 2.12.b With 500Kg payload, Shoulder Yaw excited, "out-of- plane" first vibration mode coordinates for links 2 and 3

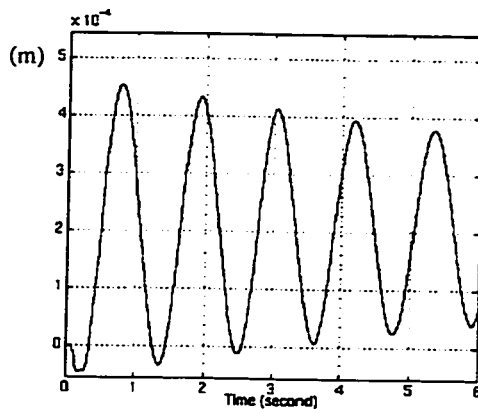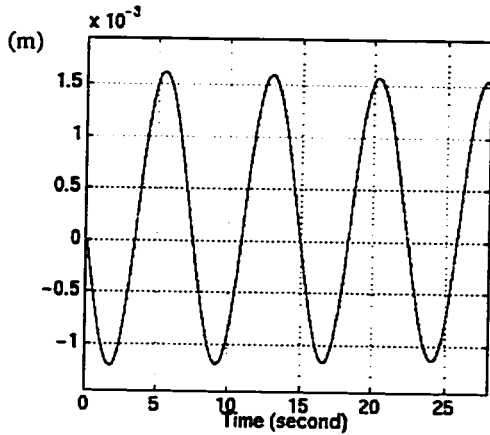Figure 2.13.a With 500Kg payload, Shoulder Pitch excited, end-effector displacements in Z direction
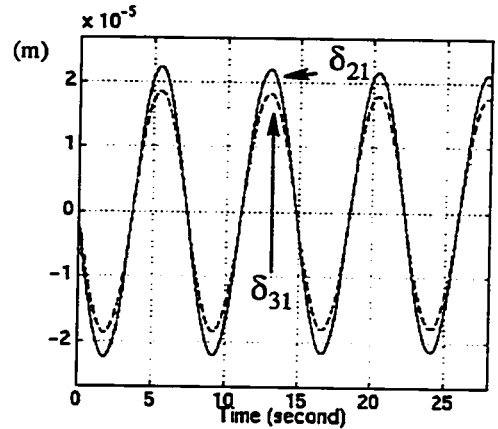
Figure 2.13.b With 500Kg payload, Shoulder Pitch excited, "in- plane" first vibration mode coordinates for links 2 and 3

The same simulations are carried out while the Elbow Pitch joint is excited. After that, all simulations are repeated in Configuration B. The simulation results demonstrate the fact that vibration frequencies vary with the change of configuration and payload. As expected, a heavier payload reduces the vibration frequencies. Here we list the measured end-effector vibration frequencies in Table 2.2, Table 2.3 and Table 2.4.

Table 2.2 End-effector vibration frequencies
excited from shoulder yaw (unit: rad/sec)

Configuration	Without Payload	With 500Kg Payload	With 29,500Kg Payload
A	4.29	2.500	0.347
B	5.35	2.24	0.379

Table 2.3 End-effector vibration frequencies
excited from shoulder pitch (unit: rad/sec)

Configuration	Without Payload	With 500Kg Payload	With 29,500Kg Payload
A	4.29	2.42	0.353
B	6.70	2.96	0.433

Table 2.4 End-effector vibration frequencies
excited from elbow pitch (unit: rad/sec)

Configuration	Without Payload	With 500Kg Payload	With 29,500Kg Payload
A	5.45	2.42	0.356
B	8.06	1.5	0.221

According to the real flight test data, the RMS tip oscillation frequency ranges from 0.5 to 2 Hz and when carrying a full payload, the oscillation frequency drops by a factor of 10-20 times. In our simulation, the tip vibration frequency is about 1 Hz and when carrying full payload, it drops to less than 0.1 Hz. It matches the real flight data with respect to the system oscillation frequency.

2.7 Servo Dynamics and Gearbox Characteristics

So far, we have obtained the system dynamics of the RMS up to link level. Now we add the servo motor shaft dynamics, gearbox dynamics and friction terms to complete the system dynamics model as shown in Figure 2.1.

2.7.1 Servo Shaft Dynamics

The motor shaft dynamics can be written as

$$J_m \ddot{\theta}_m + f_m(\dot{\theta}_m) = \tau_m \qquad (2.7.1)$$

where $f_m(\dot{\theta}_m)$ is the shaft friction, and is described in section 2.7.3.

2.7.2 Linear Gearbox characteristics

Referring to the model of a flexible joint shown in Figure 2.15, joint flexibility is modeled with linear stiffness K. Table 2.5 lists the stiffness K constant on the motor side for all six joints.
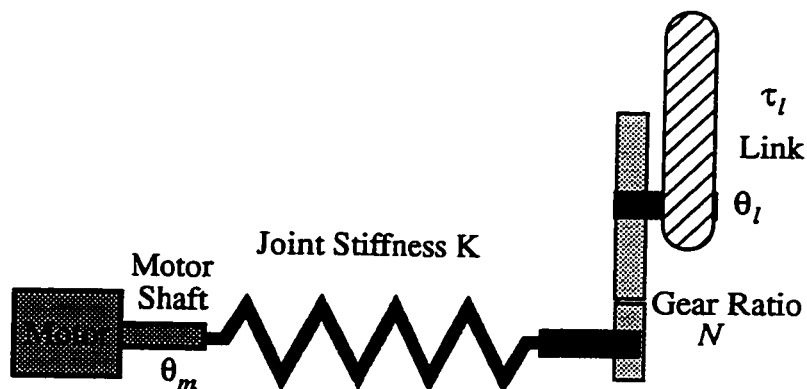
Figure 2.14 Flexible-joint model

34

Table 2.5 Gearbox linear stiffness K

	Shoulder Yaw	Shoulder Pitch	Elbow Pitch	Wrist Pitch	Wrist Yaw	Wrist Roll
K (N.m/rad)	0.47165	0.84242	1.6222	2.6162	2.6092	2.6162

We have the delivered torque at link side

$$\tau_l = K(\theta_m - \theta_l N)N \qquad (2.7.2)$$

where N is the gear ratio.

2.7.3 Friction Model

At this point, the friction is modeled as a continue function for simplicity, further references can be found in [3], [6].

$$f_m(\dot{\theta}_m) = F_s\left(1 - e^{-\left(\frac{\dot{\theta}_m}{v_s}\right)^2}\right)sign(\dot{\theta}_m) \qquad f_l(\dot{\theta}_l) = F_s\left(1 - e^{-\left(\frac{\dot{\theta}_l}{v_s}\right)^2}\right)(sign(\dot{\theta}_l)) \qquad (2.7.3)$$

where v_s is a constant.
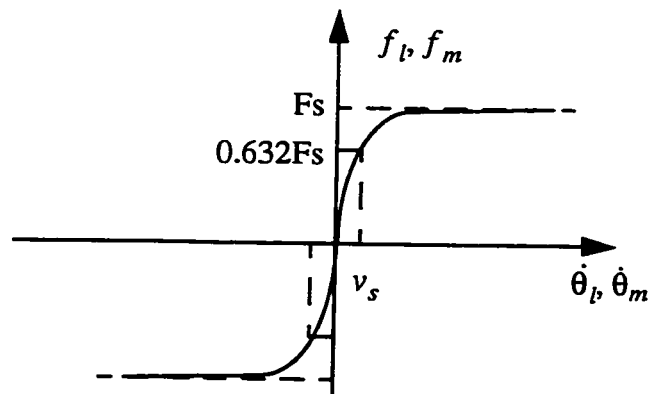
Figure 2.15 Friction model

35

The values of v_s used in link side friction models are listed in Table 2.6, and those used in motor side friction models are listed in Table 2.7.

Table 2.6 Link side friction model parameters

	Shoulder Yaw	Shoulder Pitch	Elbow Pitch	Wrist Pitch	Wrist Yaw	Wrist Roll
F_s (N.m)	54.96	51.42	37.16	21.51	21.54	21.51
v_s (rad/sec)	0.001	0.001	0.001	0.001	0.001	0.001

Table 2.7 Motor shaft friction model parameters

	Shoulder Yaw	Shoulder Pitch	Elbow Pitch	Wrist Pitch	Wrist Yaw	Wrist Roll
F_s (N.m)	0.02821	0.02821	0.02821	0.02821	0.02821	0.02821
v_s (rad/sec)	0.1	0.1	0.1	0.1	0.1	0.1

Chapter 3

RMS Link Control

Figure 3.1 shows the detailed model of the existing SRMS joint rate feedback control system of a typical joint [35]. As is evident, this is a hybrid control system with both digital and analog rate feedback control loops. An integral mode controller is added to reduce tracking errors in a line tracking trajectory mode. Obviously, there is no special control strategy for addressing the effect of link or joint flexibility.

The control architecture of our proposed controller design as shown in Figure 3.2 basically consists of four major parts:

(1) Signal pre-shaping is applied to the joint level trajectories to reduce the excitation of link flexibility.

(2) Rigid model based inverse dynamics control is applied to obtain the desired joint torques.

(3) The desired joint torques calculated in part 2 are generated by a motor torque command which is computed by applying a perturbation technique for compensating for joint flexibility.

(4) Pulse active damping is used for the residual oscillations. This part of the control operates only at the end of RMS maneuver and aims to rapidly damp out the residual vibrations.

Figure 3.1 Existing servo control model of RMS [35]

38

The first two parts aim to reduce the effect of link flexibility while the third part solves the flexible-joint problem and the last part aims to eliminate residual vibrations. The integrated control architecture combining all these parts will lead to less vibration excitation and fast damping of residual vibrations.

The first two parts will be covered in this chapter, the third part will be given in Chapter 4 and the last part will be addressed in Chapter 5.
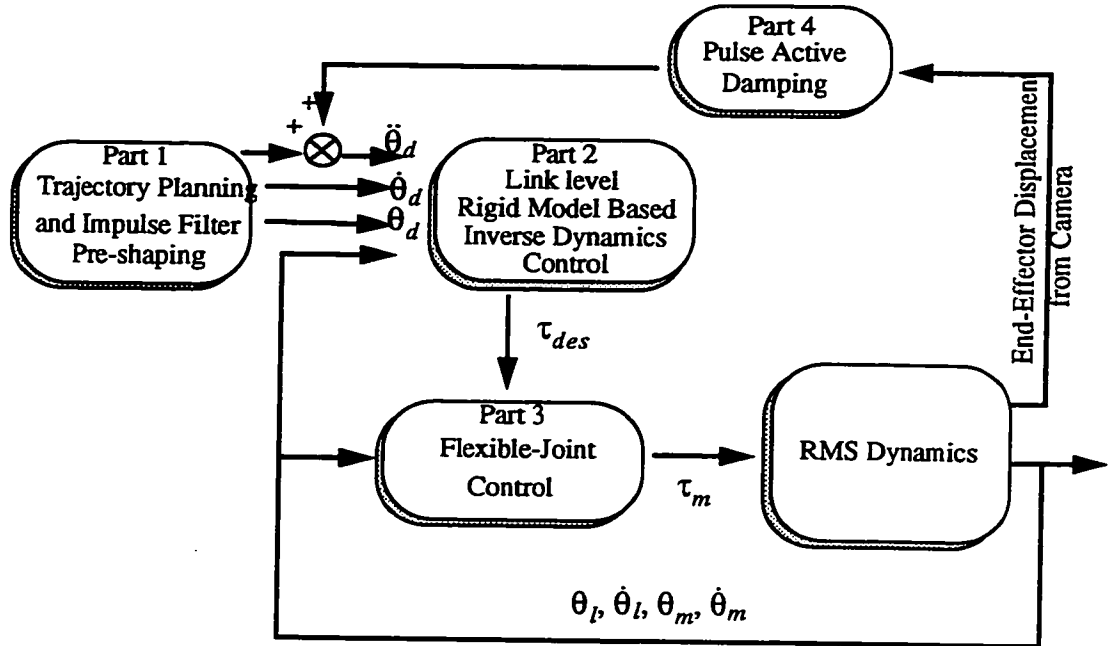
Figure 3.2 Integrated control architecture

3.1 Signal Pre-Shaping

This method was developed by [39] and later further improved or modified by several authors [34], [51], [29], [30]. Basically, by pre-shaping the input signals such as torque commands and tracking trajectories of a system using specially designed pulse filters, the frequency components close to the natural vibration frequencies are filtered out so that less vibration is observed at the system outputs. The design of these pulse filters is addressed below. The derivation is based on linear system theory. The first step towards generating a system input which results in a vibration-free system output is to specify the system

response to an impulse input. An uncoupled, linear, vibratory system of any order can be specified as a cascaded set of second-order poles with the decaying sinusoidal response:

$$y(t) = \left[A_p \frac{\omega_0}{\sqrt{1.0 - \zeta^2}} e^{-\zeta\omega_0(t - t_0)} \right] \sin(\omega_0\sqrt{1 - \zeta^2}(t - t_0)) \qquad (3.1.1)$$

where A_p is the amplitude of the impulse, ω_0 is the undamped natural frequency of the plant, ζ is the damping ratio of the plant, t is time, and t_0 is the application time of the impulse input. The impulse is usually a torque or velocity command to an actuator. Equation (3.1.1) specifies the acceleration or velocity response, $y(t)$, at some point of interest in the system.

Mathematically adding two impulse responses each described by (3.1.1), expressing the result for all time greater than the duration of the input and using the trigonometric relation

$$B_1 \sin(\alpha t + \phi_1) + B_2 \sin(\alpha t + \phi_2) = A_{amp} \sin(\alpha t + \psi) \qquad (3.1.2)$$

where

$$A_{amp} = \sqrt{(B_1 \cos\phi_1 + B_2 \cos\phi_2)^2 + (B_1 \sin\phi_1 + B_2 \sin\phi_2)^2} \qquad (3.1.3)$$

$$\psi = \tan^{-1}\left(\frac{B_1 \cos\phi_1 + B_2 \cos\phi_2}{B_1 \sin\phi_1 + B_2 \sin\phi_2}\right) , \qquad (3.1.4)$$

elimination of vibration after the second input has ended requires that the expression for (3.1.3) should equal zero at the time at which the input ends, t_2. This is true if both squared terms in (3.1.3) are independently zero, yielding:

$$B_1 \cos\phi_1 + B_2 \cos\phi_2 = 0$$
$$B_1 \sin\phi_1 + B_2 \sin\phi_2 = 0 \qquad (3.1.5)$$

40

where from (3.1.1)

$$B_j = A_{pj} \frac{\omega_0}{\sqrt{1.0 - \zeta^2}} e^{-\zeta\omega_0(t_2 - t_j)} \quad , j = 1, 2 \qquad (3.1.6)$$

with A_{pj} the amplitude of the jth impulse, t_j is the time of the jth impulse, and t_2 is the time at which the sequence ends (time of the last impulse).

By selecting $t = 0$ for the time of the first impulse, i.e., $t_1 = 0$, and 1 for the sum of the amplitudes A_1 and A_2, i.e., $A_1 + A_2 = 1$, and setting ω_0 (the expected natural frequency), two equations (with two unknowns A_2 and t_2) result. A_2 scales linearly for other values of A_1. The solution of these two equations produces the input sequence shown in Figure 3.3.

where

$$k = e^{-\frac{\zeta\pi}{\sqrt{1 - \zeta^2}}} \qquad (3.1.7)$$

$$\Delta t = \frac{\pi}{\omega_0\sqrt{1 - \zeta^2}} \qquad (3.1.8)$$

$$A_0 = \frac{1}{1 + k} \qquad A_1 = \frac{k}{1 + k}$$
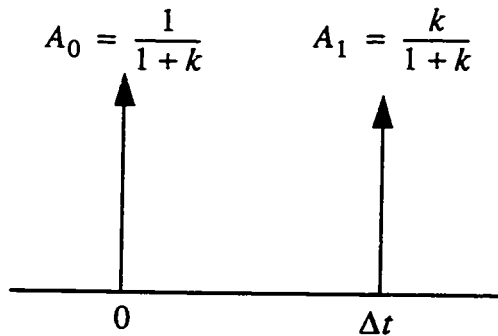
Figure 3.3 Two impulse sequence

The same impulse sequence can be obtained in the frequency domain by considering a compensator that delivers only a portion of the input to a lightly damped system and then delays the remaining portion by one-half the oscillation period to cancel the vibratory

41

motion generated by the first input [29], [30]. The compensation filter can be written as:

$$F_2 = A_1 + (1 - A_1)e^{-s\frac{\pi}{\omega_0\sqrt{1-\zeta^2}}}$$

(3.1.9)

where A_1 is a constant that always lies between one-half and one, ω_0 is the natural frequency of the system and ζ is the damping ratio. Solving for the zeros of the filter, the first pair reside at the complex conjugate pole locations of a second-order system. The resulting value of A_1 is

$$A_1 = \frac{e^{-\frac{\zeta\pi}{\sqrt{1-\zeta^2}}}}{1 + e^{-\frac{\zeta\pi}{\sqrt{1-\zeta^2}}}}$$

(3.1.10)

If we define $k = e^{-\frac{\zeta\pi}{\sqrt{1-\zeta^2}}}$ as in (3.1.7) we have $A_1 = \frac{k}{1+k}$, which shows that (3.1.9) is the same as the sequence shown in Figure 3.3.

The Two-Impulse filter can be described as:

$$\frac{1}{1+k} + \frac{ke^{-s\Delta t}}{1+k}$$

(3.1.11)

By taking the z transform of (3.1.11) the filter can be described as:

$$G_2(z) = \frac{z+k}{z(1+k)}$$

(3.1.12)

where $z = \Delta t$ which depends on the system natural frequency (3.1.8). If the vibration frequencies are not known exactly, the vibrations will not be completely eliminated after the input has ended. To increase the robustness to uncertainty in frequency and damping of the system, a three or higher order impulse sequence can be used [Singer 1989]. Without hav-

ing to solve the extra constraint equations developed by Singer and Seering, one can derive the higher order filter by placing multiple zeros at the assumed pole location as in [29]

$$F_n = (F_2(s))^{n-1} \tag{3.1.13}$$

or

$$G_n(z) = (G_2(z))^{n-1} \tag{3.1.14}$$

Therefore, a three, four impulse sequence can be easily found to be

$$G_3 = \frac{z^2 + 2kz + k^2}{z^2(1 + 2k + k^2)} \tag{3.1.15}$$

$$G_4 = \frac{z^3 + 3kz^2 + 3k^2z + k^3}{z^3(1 + 3k + 3k^2 + k^3)} \tag{3.1.16}$$

A higher-order impulse filter gives greater robustness to inaccurate natural frequency and damping ratio identification. This has been demonstrated in [39] as shown in Figure 3.4 and Figure 3.5 for robustness to uncertainty in the natural frequency.
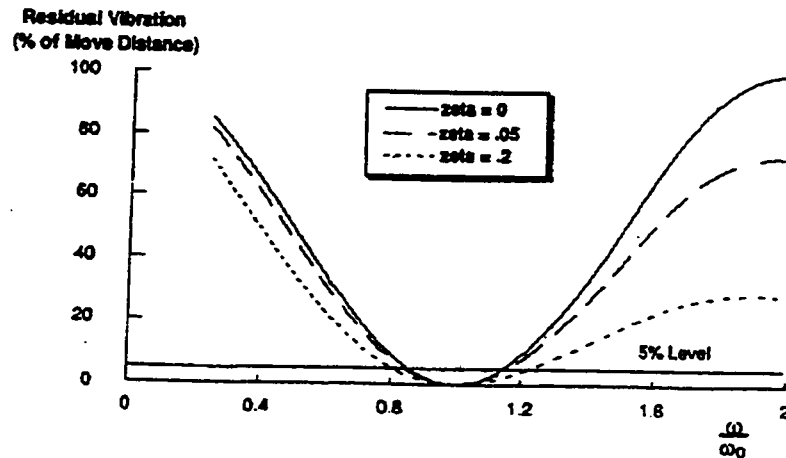
Figure 3.4: Residual vibration vs. system natural frequency for three systems with $\zeta = 0, 0.05, 0.2$ excited by a three-impulse sequence [39]
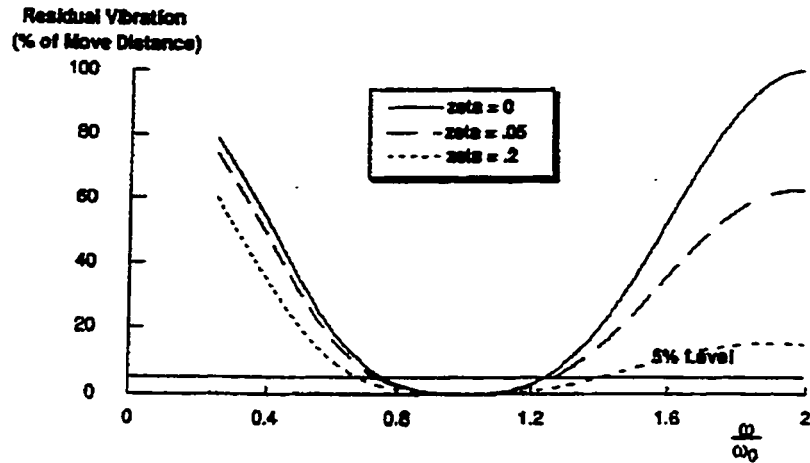
Figure 3.5 Residual vibration vs. system natural frequency for three systems
with ζ = 0, 0.05, 0.2 excited by a four-impulse sequence [39]

Figure 3.4 shows the residual vibration excited by a three-impulse sequence as a function of the system natural frequency for three systems with damping ratios ζ =0, 0.05 and 0.2. Figure 3.5 shows the residual vibration excited by a four-impulse sequence as a function of the system natural frequency for three systems with damping ratios ζ =0, 0.05 and 0.2. Damping ratio robustness was shown in [39] via Figure 3.6 that compares two-, three- and four-impulse sequences.
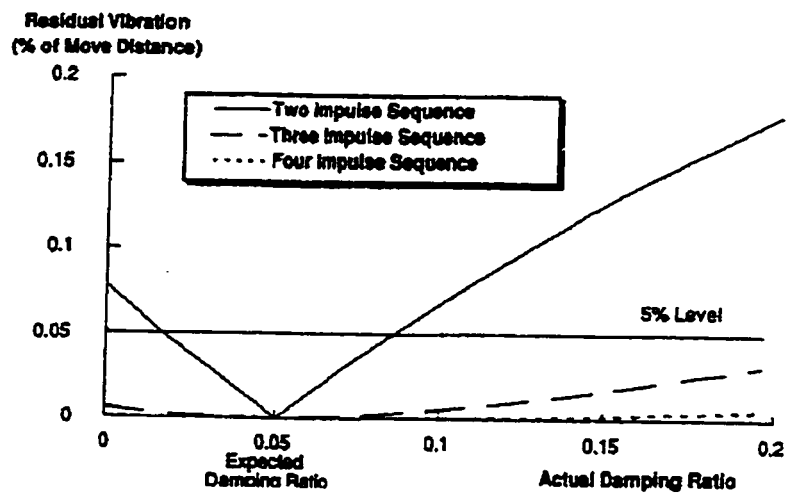
Figure 3.6 Residual vibration vs. damping ratio for two-, three- and four-impulse
inputs with ζ = 0.05 [39]

The most obvious shortcoming of an input shaping pre-compensation scheme alone is its open loop nature. That is, with such a scheme there is essentially no robustness to external disturbances, and little effective robustness to modeling uncertainties. On the other hand, input-shaping control has been shown to be an effective method for eliminating vibrational motion in small angle movements. In these movements, the frequencies of the vibrational modes do not vary greatly during the course of motion, making it possible to design impulse sequences for nominal operating point frequencies. For larger angle movements, however, the frequencies of the modes of vibration can vary significantly, and complete elimination of oscillations is not possible.

In our controller design, the proposed inverse dynamics control results in dynamics that are close to those of linear system for each joint locally. The torque to tip vibration transfer function is approximately independent of other link motion [23]. This reduces the dependence on configuration and allows off-line vibration frequency identification for excitation of each joint. The identified dominating vibration frequencies along the task trajectories can be used to update the shaping filter along the task trajectory [50]. Alternatively, a higher (4th or 5th) order filter can be applied along the trajectories if the frequency variation does not exceed the robustness bandwidth (which is the case in our approach). However, zero residual oscillations will not be observed at the end of maneuver. This will be solved by the pulse active damping algorithm described in Chapter 6.

3.2 Link Level Control with Rigid Model based Inverse Dynamics Control

At this point, when we design the link level control to compensate for link flexibility, we assume no joint flexibility. We apply inverse dynamics control which has been successfully used in rigid robot control.

45

3.2.1 Inverse Dynamics Control

To control a rigid robot manipulator, by applying inverse dynamics control, one can easily decouple the nonlinear dynamic system into a set of single-input, single-output linear systems.

Let the rigid manipulator dynamics be expressed as follows:

$$M(\theta_l)\ddot{\theta}_l + C(\theta_l, \dot{\theta}_l)\dot{\theta}_l + f(\dot{\theta}_l) = \tau_l \tag{3.2.1}$$

where θ_l denotes the joint position at the link side and τ_l the delivered joint torque at the link side. The idea of inverse dynamics control is to seek a nonlinear feedback control law

$$\tau_l = F(\theta_l, \dot{\theta}_l) \tag{3.2.2}$$

which, when substituted into (3.2.1), results in a linear decoupled closed-loop system. For general nonlinear systems such a control law may be quite difficult or impossible to find. In the case of the manipulator dynamic equation (3.2.1), however, the problem is actually easy. If we choose the control τ_l according to the equation

$$\tau_l = M(\theta_l)V + C(\theta_l, \dot{\theta}_l)\dot{\theta}_l + f(\dot{\theta}_l) \tag{3.2.3}$$

then, since the inertia matrix $M(\theta_l)$ is invertible, the combined system (3.2.1) and (3.2.3) reduces to

$$\ddot{\theta}_l = V \tag{3.2.4}$$

The term V represents a new input to the system which is yet to be chosen. (3.2.4) is known as the "double integrator system" as it represents n uncoupled double integrators for the n joints of the manipulator. The nonlinear control law (3.2.3) is called the "Inverse Dynamics Control" or "Computed Torque Control" and achieves a rather remarkable result, namely that the "new" system (3.2.4) is linear, and decoupled. This means that each input V_i can be designed to control a scalar linear system. Moreover, assuming that V_i is

a function only of θ_l and $\dot{\theta}_l$, then V_i will affect the θ_l independently of the motion of the other links.

Since V_i can now be designed to control a simple linear second order system, the obvious choice is to set

$$V = \ddot{\theta}_d + k_d(\dot{\theta}_d - \dot{\theta}_l) + k_p(\theta_d - \theta_l) \qquad (3.2.5)$$

where θ_d is the desired tracking trajectory. Then the tracking error

$$e(t) = \theta_d - \theta_l \qquad (3.2.6)$$

satisfies

$$\ddot{e}(t) + k_d\dot{e}(t) + k_p e(t) = 0 \qquad (3.2.7)$$

An obvious choice for the gain matrices k_p, k_d is

$$\begin{aligned}
k_p &= diag[\omega_1^2, \omega_2^2, ..., \omega_n^2] \\
k_d &= diag[2\omega_1, 2\omega_2, ..., 2\omega_n]
\end{aligned} \qquad (3.2.8)$$

which results in a closed-loop system which is globally decoupled, with each joint response equal to the response of a critically damped linear second order system with natural frequency ω_i.

Practical implementation of the inverse dynamic control law (3.2.3) requires both the system parameters in the dynamic model of the system be known precisely and the complete equations of motion be computable in real time.

Practically speaking, there will always be inexact cancellation of the non-linearities in the system due to model uncertainty and computational round off.

47

3.2.2 Application of Inverse Dynamics Control for a Flexible-Link Manipulator

By adding the friction term in (1.2.3), let us write the equation for a flexible-link manipulator dynamic model:

$$
\begin{bmatrix} M_r & M_c \\ M_c & M_e \end{bmatrix} \begin{bmatrix} \ddot{\theta}_l \\ \ddot{\delta} \end{bmatrix} + \begin{bmatrix} C_r & C_c \\ C_c & C_e \end{bmatrix} \begin{bmatrix} \dot{\theta}_l \\ \dot{\delta} \end{bmatrix} + \begin{bmatrix} 0 & 0 \\ 0 & K_e \end{bmatrix} \begin{bmatrix} \theta_l \\ \delta \end{bmatrix} + \begin{bmatrix} f_l(\dot{\theta}_l) \\ 0 \end{bmatrix} = \begin{bmatrix} \tau_l \\ 0 \end{bmatrix} \qquad (3.2.9)
$$

where δ denotes the elastic coordinates.

The presence of the elastic variables δ makes it impossible to use exact inverse dynamics control for flexible manipulator. However, if the elastic effects in (1.3) are small compared to the rigid motion, (which is the case in this design because of the slow maneuvering speed), the elastic effects can be treated as model uncertainties or disturbances. The system can then be controlled by a rigid model based inverse dynamics controller, i.e., the inverse dynamics corresponds to the manipulator rigid dynamics only. Some works [23], [21] has shown successful control designs for flexible-link manipulators using inverse dynamics control based on reduced-order or rigid dynamic models only. This approach is adopted in this thesis.

We rewrite the upper part of (1.3) which is associated with the joint states:

$$
M_r \ddot{\theta}_l + C_r \dot{\theta}_l + M_c \ddot{\delta} + C_c \dot{\delta} + f_l(\dot{\theta}_l) = \tau_l \qquad (3.2.10)
$$

Next, we define

$$
\eta(\delta, \dot{\delta}, \ddot{\delta}) = M_c \ddot{\delta} + C_c \dot{\delta} \qquad (3.2.11)
$$

and design the nonlinear control law based on the manipulator rigid dynamics

$$\tau_l = \widehat{M}_r(\theta_l)V + \widehat{C}_r(\theta_l, \dot{\theta}_l)\dot{\theta}_l + \widehat{f}_l(\dot{\theta}_l) \tag{3.2.12}$$

where, $\widehat{M}_r$, $\widehat{C}_r$ denote the terms corresponding to M_r and C_r in the rigid dynamic model. We can define the model error as

$$\Delta M_r = \widehat{M}_r - M_r \quad \Delta C_r = (\widehat{C}_r - C_r)\dot{\theta}_l \quad \Delta f_r = \widehat{f}_r - f_r$$

thus $\ddot{\theta}_l$ can be expressed as

$$\ddot{\theta}_l = M_r^{-1}\widehat{M}_r V + M_r^{-1}(\Delta C_r + \Delta f_r) - M_r^{-1}\eta(\delta, \dot{\delta}, \ddot{\delta})$$

$$= V + (M_r^{-1}\widehat{M}_r - I)V + M_r^{-1}(\Delta C_r + \Delta f_r - \eta(\delta, \dot{\delta}, \ddot{\delta})) \tag{3.2.13}$$

With (3.2.5), we can write the above equation for the error $e(t) = \theta_l - \theta_d$ as

$$\ddot{e}(t) + k_d\dot{e}(t) + k_p e(t) = (M_r^{-1}\widehat{M}_r - I)V + M_r^{-1}(\Delta C_r + \Delta f_r - \eta(\delta, \dot{\delta}, \ddot{\delta}))$$

$$= (M_r^{-1}\widehat{M}_r - I)[\ddot{\theta}_d + k_d(\dot{\theta}_d - \dot{\theta}_l) + k_p(\theta_d - \theta_l)] + M_r^{-1}(\Delta C_r + \Delta f_r - \eta(\delta, \dot{\delta}, \ddot{\delta}))$$

$$(3.2.14)$$

The closed-loop system (3.2.14) is still a coupled nonlinear system since the right side of (3.2.14) is a nonlinear function of both rigid variables and elastic variables. Therefore, it is not obvious that the system is stable. The following aspects will help to increase the stability margin:

(1) The rigid model is accurate, i.e. ΔM_r, ΔC_r and Δf_r are sufficiently small;

(2) V is sufficiently small, which implies that $\ddot{\theta}_d$, k_p, k_d should not be large;

(3) Most important, for a flexible manipulator, $\eta(\delta, \dot{\delta}, \ddot{\delta})$ in (3.2.11) should be suffi-

ciently small.

The first two conditions can generally be satisfied by accurate modeling and smooth trajectory planning. The last assumption will depends on the excitation level of the flexibility in the system. There are two facts in our work which satisfy these conditions. They are:

(1) Slow maneuvering speed is required in space tasks for safety and precision;

(2) A smooth trajectory (5th order polynomial trajectory) is used in trajectory generation;

(3) A signal pre-shaping filter is applied on the desired trajectory which effectively reduces the vibration effects as well as $\eta(\delta, \dot{\delta}, \ddot{\delta})$.

3.3 Simulations

Three computer simulations have been done to demonstrate the design idea described above. The proposed control structure is shown in Figure 3.7.
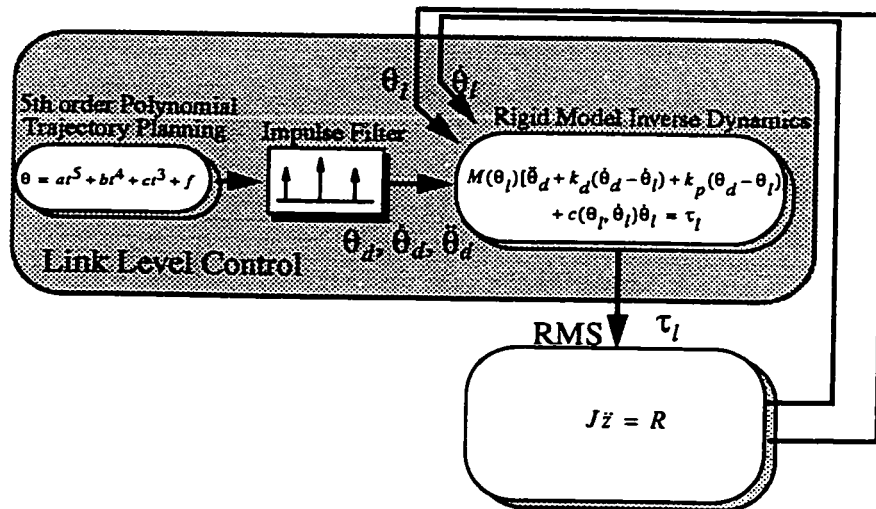

Figure 3.7 Rigid body based inverse dynamics control structure

Simulation with Rigid Inverse Dynamics Link Control (no Pre-shaping)

Around configuration A (refer to Figure 2.5), a slewing motion during which the first three joints move $\frac{\pi}{8}$ rads in 12 seconds using inverse dynamic control is simulated. The commanded trajectories are not filtered.

(1) Without payload: The results are plotted in Figures 3.8.a-c for end-effector errors in the X, Y and Z directions respectively. Figure 3.8.d shows the joint errors, Figure 3.8.e gives plots of the first "in-plane" and "out-of-plane" elastic mode coordinates for links 2 and 3.

(2) with 500Kg payload. The results are plotted in Figure 3.9.a-c, for end-effector errors in the X, Y and Z directions respectively. Figure 3.9.d shows the joint errors, Figure 3.9.e gives plots of the first "in-plane" and "out-of-plane" elastic mode coordinates for links 2 and 3.
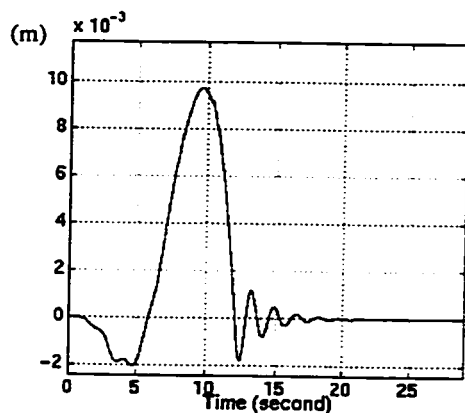
Figure 3.8.a No pre-shaping, no payload, end-effector deflection along X
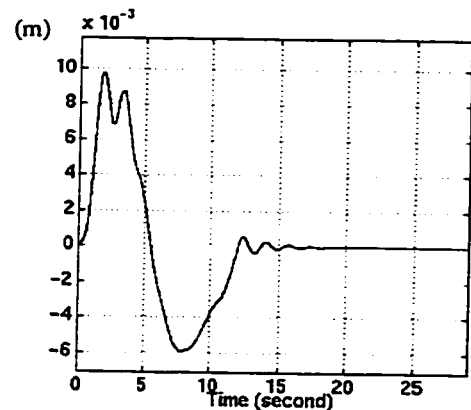
Figure 3.8.b No pre-shaping, no payload, end-effector deflection along Y
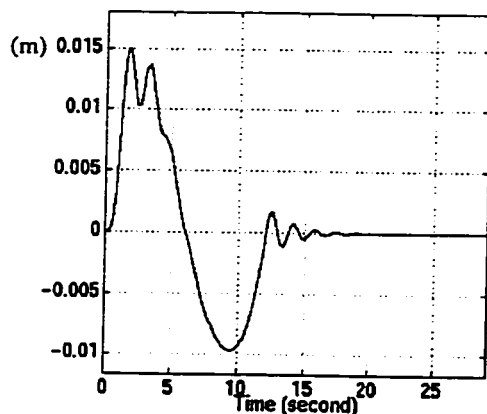
Figure 3.8.c No pre-shaping, no payload, end-effector deflection along Z
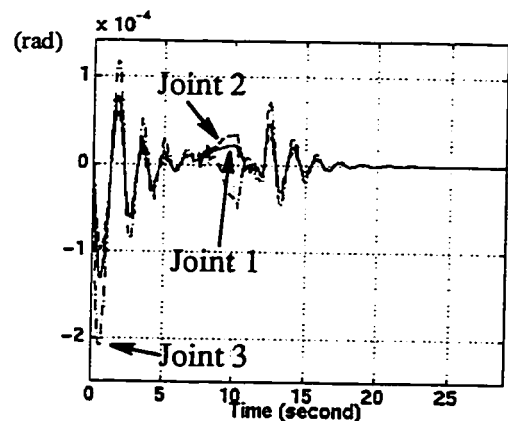
Figure 3.8.d No pre-shaping, no payload, first three joint errors

51
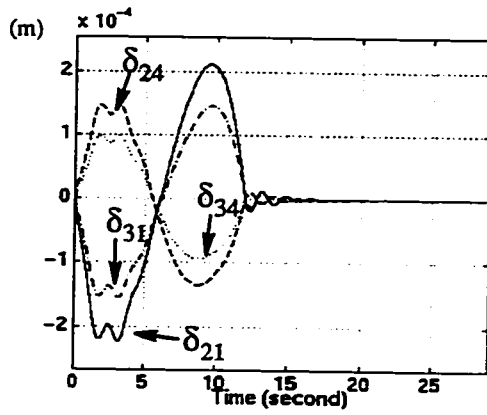
Figure 3.8.e No pre-shaping, no payload,
"in-plane" and "out-of-plane" elastic states

Figure 3.9.a No pre-shaping, 500Kg payload,
end-effector deflection along X

Figure 3.9.b No pre-shaping, 500Kg payload,
end-effector deflection along Y

Figure 3.9.c No pre-shaping, 500Kg payload,
end-effector deflection along Z

Figure 3.9.d No pre-shaping, 500Kg payload,
first three joint errors

Figure 3.9.e No pre-shaping, 500Kg payload,
"in-plane" and "out-of-plane" elastic states

Comparing these simulation results, one can easily see that the residual vibrations for the case with the payload are much larger than for the case without payload. A larger payload introduces larger elastic deflection of the system, and because the structural damping of the elasticity is very small, around 0.001, larger residual vibrations occur at the end of slewing.

Simulation with Rigid Inverse Dynamics Link Control and Trajectory Pre-shaping

In this simulation, with the same maneuvering task and the same link control as above for the 500Kg payload, the joint trajectories are passed through a three-impulse filter.

The filter is designed based on the vibration frequency identification results in Table2.2-2.4. The simulation results are plotted in Figure 3.10.a-c for the end-effector errors in the X, Y and Z directions. Figure 3.10.d shows the joint errors, Figure 3.10.e gives plots of the first "in-plane" and "out-of-plane" elastic mode coordinates for links 2 and 3.

Clearly, by filtering the trajectories with the impulse pre-shaping filters, the most dominant vibration frequency component is filtered out from the trajectory and therefore the vibration excitation of the system is much less than that without pre-shaping (Figures 3.8 and 3.9).
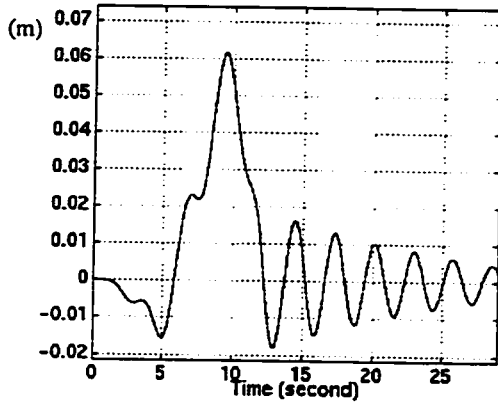
53
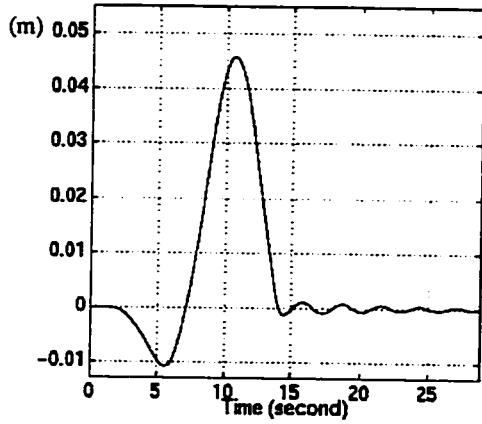
Figure 3.10.a With pre-shaping, 500Kg payload,
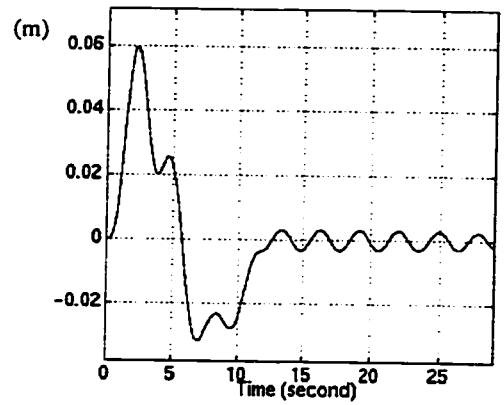end-effector deflection along X
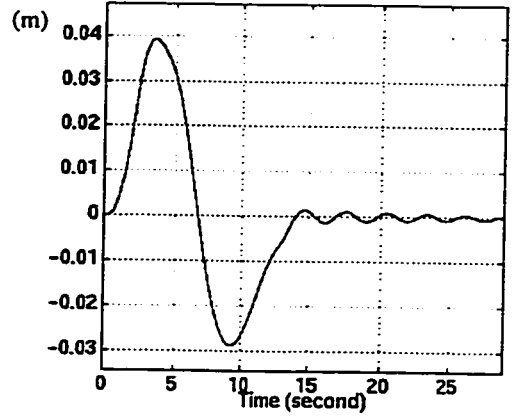
Figure 3.10.b With pre-shaping, 500Kg payload,
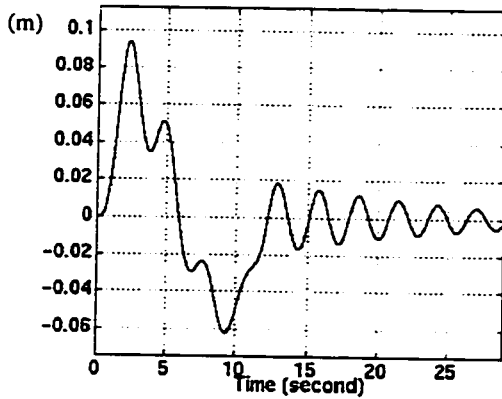end-effector deflection along Y
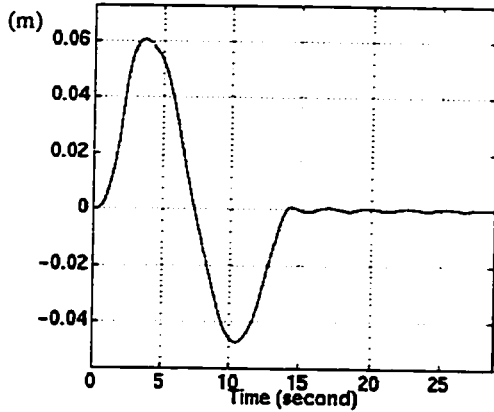
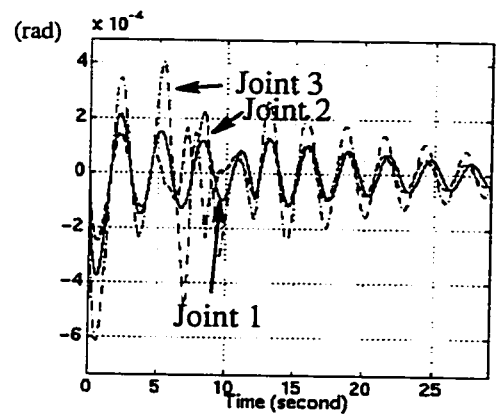Figure 3.10.c With pre-shaping, 500Kg payload,
end-effector deflection along Z

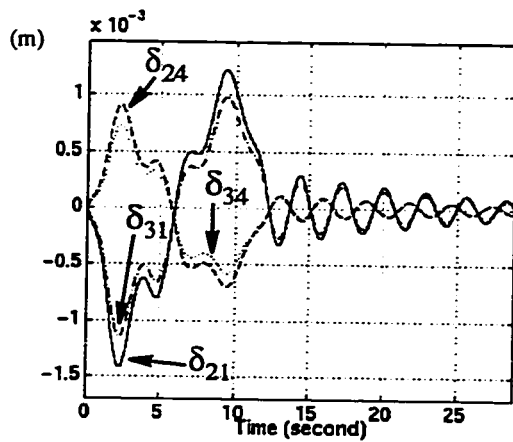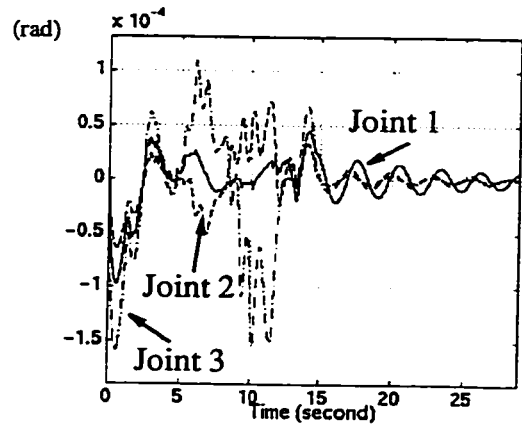Figure 3.10.d With pre-shaping, 500Kg payload,
first three joint error
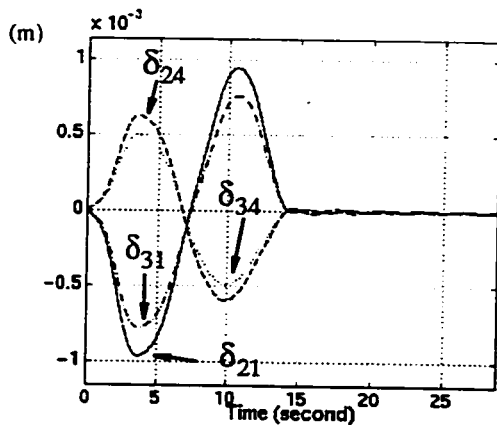
Figure 3.10.e With pre-shaping, 500Kg payload,
"in-plane" and "out-of-plane" elastic states

54

Chapter 4

Flexible-Joint Control

4.1 Perturbation Techniques

In [9], a new control methodology was developed for robotic manipulator with flexible joints using perturbation techniques. Considering the simplicity of this method and the slow speed requirements of the RMS, we have adopted this approach for our controller design.

The flexible-joint mechanism is shown in Figure 4.1 with a unity gear ratio, i.e., $N = 1$. Later, the control design will be extended to deal with non-unity gear ratio. The joint flexibility is modeled as a spring with a constant stiffness K.
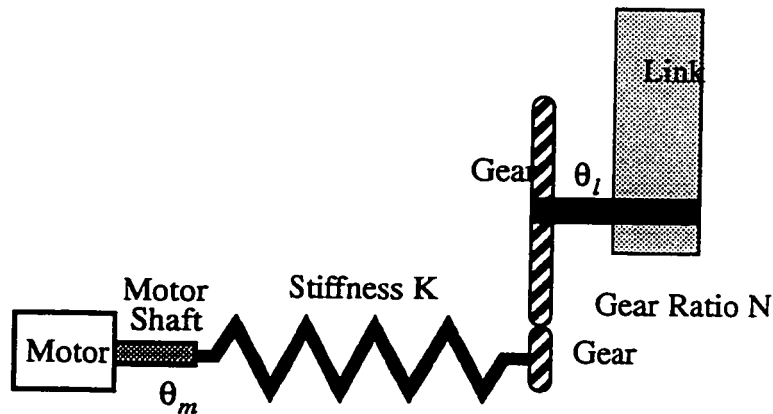
Figure 4.1 Flexible-joint model

The dynamics of a rigid-link manipulator can be written as

$$M(\theta_l)\ddot{\theta}_l + C(\theta_l, \dot{\theta}_l)\dot{\theta}_l + f_l(\dot{\theta}_l) = K(\theta_m - \theta_l) \tag{4.1.1}$$

and by neglecting the shaft friction, the servo shaft dynamics can be written as

$$J_m\ddot{\theta}_m - K(\theta_l - \theta_m) = \tau_m \tag{4.1.2}$$

The friction effect will be compensated by adding an extra term as shown in (4.1.29). In (4.1.1) and (4.1.2), M denotes the manipulator inertia matrix, f_l the joint friction, K the joint stiffness, J_m the motor shaft inertia, θ_m, θ_l the shaft position and link side joint position respectively and τ_m the motor shaft output torque.

The objective here is to design τ_m so that the link torque $K(\theta_m - \theta_l)$ will follow the desired torque profile (3.2.3) and (3.2.5) as designed in the previous chapter based on rigid inverse dynamics control as repeated here:

$$\tau_l = M(\theta_l)V + C(\theta_l, \dot{\theta}_l)\dot{\theta}_l + f_l(\dot{\theta}_l) \tag{3.2.3}$$

where

$$V = \ddot{\theta}_d + k_d(\dot{\theta}_d - \dot{\theta}_l) + k_p(\theta_d - \theta_l) \tag{3.2.5}$$

In [9], it was shown that if the shaft output is in the form

$$\tau_m = \varepsilon^{-2}k_1[\theta_l - \theta_m + u_{des}(\theta_l, \dot{\theta}_l)] + \varepsilon^{-1}k_2[\dot{\theta}_l - \dot{\theta}_m] \tag{4.1.3}$$

where $\varepsilon > 0$ is the so-called singular perturbation parameter which is sufficiently small and $u_{des} = \dfrac{\tau_l}{K}$, we can re-write the (4.1.1) and (4.1.2) as

$$M(\theta_l)\ddot{\theta}_l + C(\theta_l, \dot{\theta}_l)\dot{\theta}_l + f_l(\dot{\theta}_l) = K(\theta_m - \theta_l) \tag{4.1.4}$$

$$J_m\ddot{\theta}_m - K(\theta_l - \theta_m) = \varepsilon^{-2}k_1[\theta_l - \theta_m + u_{des}] + \varepsilon^{-1}k_2[\dot{\theta}_l - \dot{\theta}_m] \tag{4.1.5}$$

Defining $z = \theta_l - \theta_m$, we have

$$J_m(\ddot{\theta}_m - \ddot{\theta}_l) + J_m\ddot{\theta}_l - Kz = \varepsilon^{-2}k_1[z + u_{des}] + \varepsilon^{-1}k_2\dot{z}$$

$$-J_m\ddot{z} + J_m\ddot{\theta}_l - Kz = \varepsilon^{-2}k_1[z + u_{des}] + \varepsilon^{-1}k_2\dot{z} \tag{4.1.6}$$

Equations (4.1.4) and (4.1.5) become

$$M(\theta_l)\ddot{\theta}_l + C(\theta_l, \dot{\theta}_l)\dot{\theta}_l + f_l(\dot{\theta}_l) = -Kz \tag{4.1.7}$$

$$J_m\varepsilon^2\ddot{z} + \varepsilon k_2\dot{z} + k_1 z = -k_1 u_{des} - \varepsilon^2(Kz - J_m\ddot{\theta}_l) \tag{4.1.8}$$

The system of (4.1.7) and (4.1.8) is singularly perturbed. The variables z and $\dot{z}$ have the interpretation of "fast" variables, whereas the link variables $\theta_l, \dot{\theta}_l$ are "slow" variables. Using standard results from singular perturbation theory [26], we may approximate the system (4.1.7) and (4.1.8) by using a quasi-steady-state system and a boundary-layer system as follows. With $\varepsilon \to 0$ (4.1.8) becomes

$$k_1\bar{z} = -k_1\bar{u}_{des} \tag{4.1.9}$$

where the overbars indicate that the variables are defined at $\varepsilon \to 0$.

The quasi-steady-state system can be expressed as

$$M(\bar{\theta}_l)\ddot{\bar{\theta}}_l + C(\bar{\theta}_l, \dot{\bar{\theta}}_l)\dot{\bar{\theta}}_l + f_l(\dot{\bar{\theta}}_l) = -K\bar{u}_{des} \tag{4.1.10}$$

and the "fast" and "slow" variables can be written as functions of the slow time scale t and

57

fast time scale τ

$$z(t) = \bar{z}(t) + \eta(\tau) + O(\varepsilon) \tag{4.1.11}$$

$$\theta_l(t) = \bar{\theta}_l(t) + O(\varepsilon) \tag{4.1.12}$$

$O(\varepsilon)$ denotes terms of order ε or higher, fast time scale $\tau = \dfrac{t}{\varepsilon}$

To find the boundary layer, we have

$$\frac{dz}{d\tau} = \varepsilon\frac{dz}{dt} \qquad\qquad \frac{d^2z}{d\tau^2} = \varepsilon^2\frac{d^2z}{dt^2} \tag{4.1.13}$$

So that (4.1.8) becomes

$$J_m\varepsilon^2\left(\frac{1}{\varepsilon^2}\frac{d^2z}{d\tau^2}\right) + k_2\varepsilon\left(\frac{1}{\varepsilon}\frac{dz}{d\tau}\right) + k_1 z = -k_1 u_{des} - \varepsilon^2(Kz - J_m\ddot{\theta}_l) \tag{4.1.14}$$

Substituting $z(t) = \bar{z}(t) + \eta(\tau)$, equation (4.1.14) can be written as

$$J_m\frac{\partial^2\eta}{\partial\tau^2} + k_2\frac{\partial\eta}{\partial\tau} + k_1\eta + k_1\bar{z} = -k_1 u_{des} - \varepsilon^2(Kz - J_m\ddot{\theta}_l) \tag{4.1.15}$$

With $\varepsilon \to 0$, equation (4.1.15) yields

$$\tag{4.1.16}$$
$$J_m\frac{\partial^2\eta}{\partial\tau^2} + k_2\frac{\partial\eta}{\partial\tau} + k_1\eta = 0.$$

Defining

$$\tag{4.1.17}$$

$$y_1 = \eta, y_2 = \frac{\partial\eta}{\partial\tau},$$

η satisfies the following boundary layer system which is exponentially stable:

$$\begin{bmatrix} y_1' \\ y_2' \end{bmatrix} = \begin{bmatrix} 0 & 1 \\ -J_m^{-1}k_1 & -J_m^{-1}k_2 \end{bmatrix}\begin{bmatrix} y_1 \\ y_2 \end{bmatrix} \tag{4.1.18}$$

To extend the results to systems with gear ratio N, we modify the dynamic equations (4.1.1) and (4.1.2) to

$$M(\theta_l)\ddot{\theta}_l + C(\theta_l, \dot{\theta}_l)\dot{\theta}_l + f_l(\dot{\theta}_l) = NK(\theta_m - \theta_l N) \tag{4.1.19}$$

$$J_m\ddot{\theta}_m = \tau_m - K(\theta_m - \theta_l N) \tag{4.1.20}$$

Then we define some new variables:

$$\tilde{\theta}_m = \frac{\theta_m}{N}, \tilde{\tau}_m = \tau_m N \tag{4.1.21}$$

$$\tilde{J}_m = J_m N^2, \tilde{K} = KN^2 \tag{4.1.22}$$

Equation (4.1.20) becomes

$$J_m\ddot{\tilde{\theta}}_m N = \tau_m - K(N\tilde{\theta}_m - \theta_l N)$$

$$J_m N^2 \ddot{\tilde{\theta}}_m = \tau_m N - KN^2(\tilde{\theta}_m - \theta_l) \tag{4.1.23}$$

$$J_m N^2 \ddot{\tilde{\theta}}_m = \tilde{\tau}_m - KN^2(\tilde{\theta}_m - \theta_l)$$

We can now re-write the system dynamics (4.1.19) and (4.1.20) as

$$M(\theta_l)\ddot{\theta}_l + C(\theta_l, \dot{\theta}_l)\dot{\theta}_l + f_l(\dot{\theta}_l) = \tilde{K}(\tilde{\theta}_m - \theta_l) \tag{4.1.24}$$

$$\tilde{J}_m\ddot{\tilde{\theta}}_m = \tilde{\tau}_m - \tilde{K}(\tilde{\theta}_m - \theta_l) \tag{4.1.25}$$

which is in the same form as (4.1.1) and (4.1.2). Therefore, we can obtain the perturbation flexible-joint control similar to (4.1.3) as

$$\tilde{\tau}_m = \frac{k_1}{\varepsilon^2}\left(\theta_l - \tilde{\theta}_m + \frac{\tau_l}{\tilde{K}}\right) + \frac{k_2}{\varepsilon}[\dot{\theta}_l - \dot{\tilde{\theta}}_m] \tag{4.1.26}$$

where τ_l is defined in (3.2.3) which is the desired link joint torque at link side. Defining

$$k_{pp} = \frac{k_1}{\varepsilon^2}, k_v = \frac{k_2}{\varepsilon} \tag{4.1.27}$$

and with equations (4.1.21) and (4.2.22) we have

$$\tau_m = \frac{k_{pp}\left(\theta_l - \frac{\theta_m}{N} + \frac{\tau_l}{N^2 K}\right) + k_v\left[\dot{\theta}_l - \frac{\dot{\theta}_m}{N}\right]}{N}$$

$$= \frac{k_{pp}\left(N\theta_l - \theta_m + \frac{\tau_l}{NK}\right) + k_v[\dot{\theta}_l N - \dot{\theta}_m]}{N^2} \qquad (4.1.28)$$

To compensate the motor shaft friction, we add a friction compensation term in (4.1.28) and obtain

$$\tau_m = \frac{k_{pp}\left(N\theta_l - \theta_m + \frac{\tau_l}{NK}\right) + k_v[\dot{\theta}_l N - \dot{\theta}_m]}{N^2} + f_m(\dot{\theta}_m) \qquad (4.1.29)$$

4.2 Simulations

At this point, the RMS model was adjusted to incorporate joint flexibility. The simulation was carried out around configuration A (refer to Figure 2.5) with an 800Kg payload. A slewing motion during which the first three joints move through $\frac{\pi}{8}$ rads in 12 seconds is simulated with link inverse dynamics control and flexible-joint perturbation control.

(1) No flexible-joint control

When no flexible-joint control is involved, the control is based on the inverse dynamics control which assumes no joint flexibility. Joint position feedback is obtained from the motor shaft side with gear ratio factoring. With the un-pre-shaped slewing trajectories, we simulate the maneuver and plot the results in Figure 4.2.a-c for the end-effector errors in X, Y and Z directions respectively. Figure 4.2.d shows errors for the first three joints, Figure 4.2.e gives plots of the first order "in-plane" and "out-of-plane" elastic mode coordinates for links 2 and 3, and Figure 4.2.f shows the gear deflection $N\theta_l - \theta_m$.

60

(2) With flexible-joint control

This time around the same configuration and with the same link control parameters as above, the addressed flexible-joint control algorithm is applied with $k_{pp} = 8 \times 10^7$ and $k_v = 5 \times 10^3$ which are tuned by observing the simulation results and by noting that larger k_{pp} and k_v lead to lower joint error but reduce the system stability margin. The simulation results are plotted in Figure 4.3.a-c for the end-effector errors in X, Y and Z directions respectively. Figure 4.3.d shows errors for the first three joints, Figure 4.3.e gives plots of the first order "in-plane" and "out-of-plane" elastic mode coordinates for links 2 and 3, and Figure 4.3.f shows the gear deflection $N\theta_l - \theta_m$.

We find with flexible-joint control, the residual end-effector position errors were not improved significantly because the link vibrations dominate. But clearly, with flexible-joint control, all end-effector position errors, joint errors during maneuver have been improved significantly. The flexible-joint control indeed isolates the joint flexibility effect from the other control problems such as link control. The residual vibrations can be reduced by applying pre-shaping on the trajectory as being addressed in Chapter 3 and completely damped out by the Active Damping Control which will be addressed in Chapter 5.

Figure 4.2.a No flexible-joint control
End-effector error in X direction

Figure 4.2.b No flexible-joint control
End-effector error in Y direction
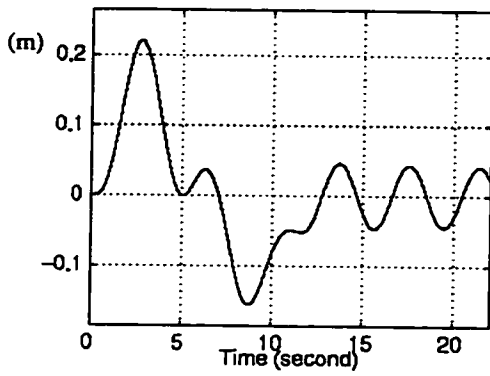
Figure 4.2.c No flexible-joint control
end-effector error in Z direction
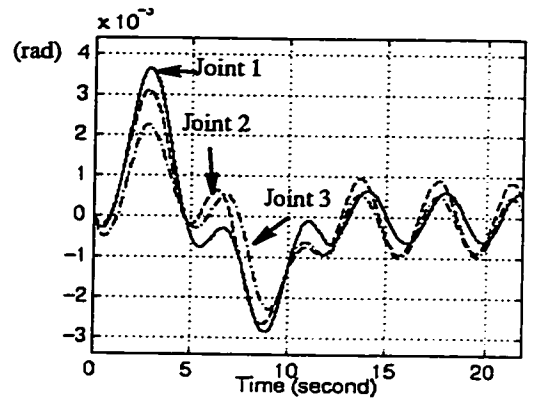
Figure 4.2.d No flexible-joint control
the first three joint errors
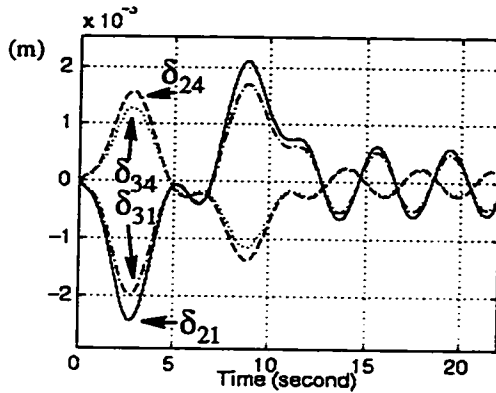
Figure 4.2.e No flexible-joint control
"in-plane" and "out-plane" elastic coordinates
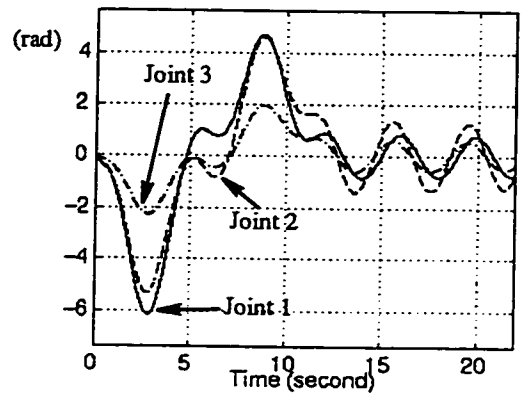
Figure 4.2.f No flexible-joint control
gear deflection
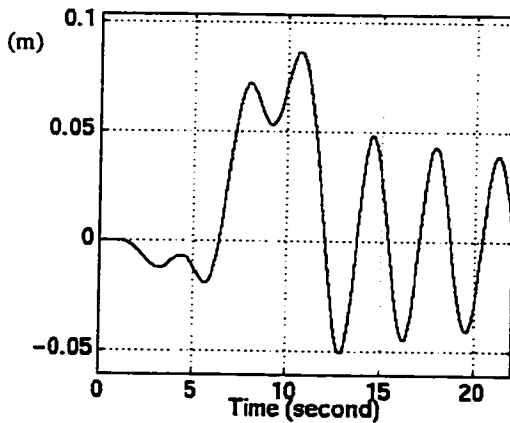
Figure 4.3.a With flexible-joint control
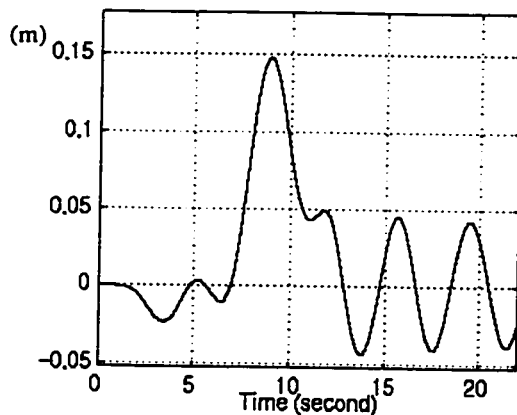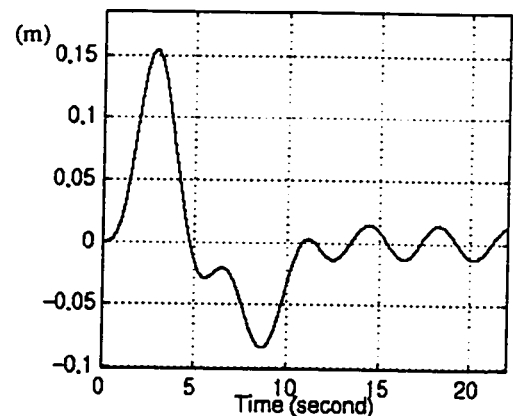End-effector error in X direction
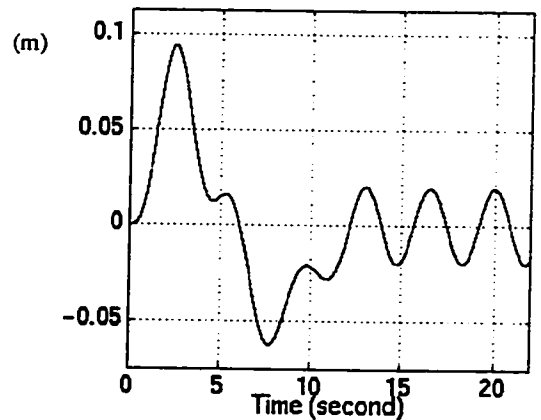
Figure 4.3.b With flexible-joint control
End-effector error in Y direction
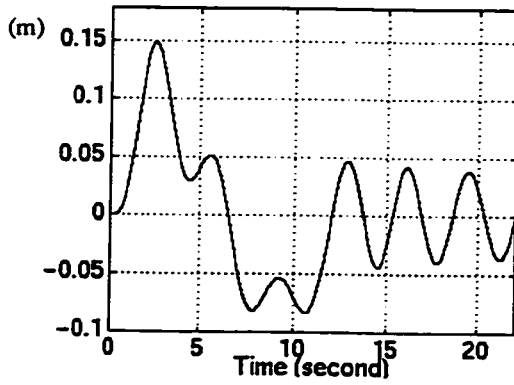
Figure 4.3.c With flexible-joint control
end-effector error in Z direction
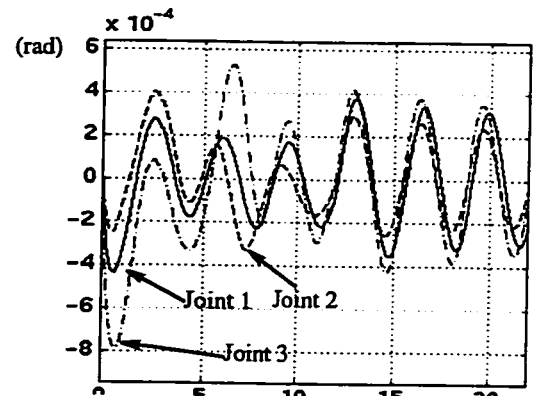
Figure 4.3.d With flexible-joint control
the first three joint errors
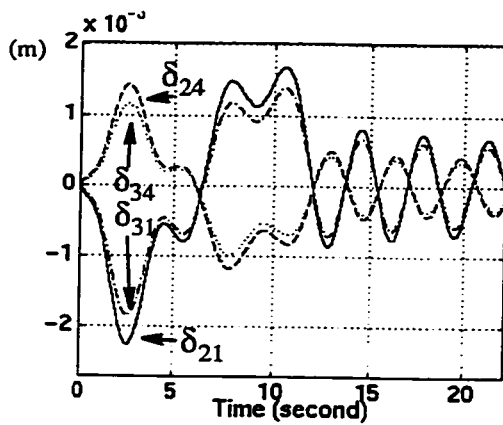
Figure 4.3.e With flexible-joint control
"in-plane" and "out-plane" elastic coordinates
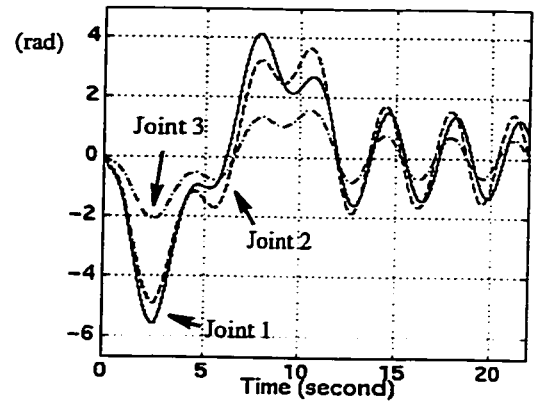
Figure 4.3.f With flexible-joint control
gear deflection

63

Chapter 5

Pulse Active Damping

One of the challenging control problem for RMS is that of controlling the residual vibrations. Due to its low structural damping, a large part of the RMS operation time is expended in waiting for the residual vibrations to die out. As we mentioned in Chapter 3, an efficient method developed recently for handling such vibrations is the input pre-shaping method which was developed in [39]. Several researchers [34] [30] have improved upon this in order to overcome some restrictions and shortcomings of the method. Two of the major restrictions are that the pre-shaping filter is mainly designed for open loop application, and the performance of the pre-shaping filter depends on accurate knowledge of the system's natural frequencies.

In our flexible-link control approach, we apply Singer's pre-shaping method on the desired trajectory in order to filter out most of its vibration exciting components. However, for a task with large configuration variations, inevitably the system natural frequencies will vary along the trajectory. Complete vibration filtering can therefore not be achieved, i.e., zero residual vibrations will not be observed at the end of the motion.

In this chapter, an additional control algorithm called "Pulse Active Damping" is developed. This control scheme is activated after the system reaches the final

configuration and its function is to rapidly damp out the residual vibrations.

5.1 Pulse Active Damping

When the RMS reaches its final configuration with non-zero residual vibrations, one can measure the magnitude of the end-effector tip vibrations using data from the cameras mounted on the RMS. We can model the tip vibrations by a sinusoidal function

$$X_{tip} = \Re e^{-\xi \omega_0 t} \sin(\omega t - \phi) = A e^{-\xi \omega_0 t} \sin(\omega t) + B e^{-\xi \omega_0 t} \cos(\omega t) \qquad (5.1.1)$$

where ω_0 is the undamped natural frequency and ω is the damped natural frequency

$$\omega = \omega_0 \sqrt{1 - \xi^2}$$

Because the first order vibrations generally dominate and the higher order vibrations are damped out more rapidly by the relatively larger structural damping, the second- and higher-order vibration terms are neglected. This is especially true for a slow-motion maneuver of a typical RMS task. However, the proposed pulse control approach is not restricted to handling single frequency vibrations only. The same control can be designed to handle higher frequency vibrations if the higher-order vibrations can be identified.

We can assume the damped system natural frequency ω and structural damping ξ at the final configuration are available via online system identification [20] using camera data or are known *a priori* via off-line computer simulation. During on-line control, we can identify the parameters in (5.1.1) by measuring tip displacement X_{tip}. Assuming that the tip displacement is measured at several sample times $t_i, i = 0, 1, ..., n$, and $t_0 = 0$, we have

$$\begin{bmatrix} A \\ B \end{bmatrix} = (\Psi^T \Psi)^{-1} \Psi^T \overline{X} \qquad (5.1.2)$$

where

$$\Psi = \begin{bmatrix} 0 & 1 \\ \vdots & \vdots \\ e^{-\xi\omega_0 t_n}\sin(\omega t_n) & e^{-\xi\omega_0 t_n}\cos(\omega t_n) \end{bmatrix}, \overline{X} = \begin{bmatrix} X_{tip}(0) \\ \vdots \\ X_{tip}(t_n) \end{bmatrix}$$

Suppose a torque impulse with magnitude P produces tip displacement

$$X_{tip} = Qe^{-\xi\omega_0(t-t_d)}\sin(\omega(t-t_d)) \qquad t > t_d \tag{5.1.3}$$

Then, in order to activate an opposite cancelling vibration, we can apply an impulse at

$t = t_a = \dfrac{\pi+\phi}{\omega} - t_d$ with magnitude equal to

$$K_s \frac{\Re P}{Q} e^{-\xi\omega_0(t_a+t_d)} \tag{5.1.4}$$

if $t_a > t_n$, otherwise we can apply an impulse at $t = t_a = \dfrac{2\pi+\phi}{\omega} - t_d$ with magnitude

equal to

$$-K_s \frac{\Re P}{Q} e^{-\xi\omega_0(t_a+t_d)} \tag{5.1.5}$$

where K_s is a gain factor which is less than 1 and is used to ensure that no over cancellation occurs.

If $K_s = 1$, and we apply an impulse at $t = t_a = \dfrac{\pi+\phi}{\omega} - t_d$, the cancelling tip

vibrations excited by the impulse can be described by

$$\begin{aligned} X_{tip} &= \Re e^{-\xi\omega_0(t_a+t_d)}e^{-\xi\omega_0(t-t_a-t_d)}\sin(\omega(t-t_a-t_d)) \\ &= \Re e^{-\xi\omega_0 t}\sin\left(\omega\left(t-\frac{\pi+\phi}{\omega}\right)\right) = \Re e^{-\xi\omega_0 t}\sin(\omega t-\phi-\pi) \qquad t > t_a + t_d \end{aligned}$$

$$\tag{5.1.6}$$

This has 180° phase difference with the original vibrations (5.1.1), i.e., complete tip

vibration cancellation is achieved at $t = t_a + t_d$ and thereafter.

Perfect cancellation with one impulse application will only occur if we have perfect knowledge of the fundamental natural frequency of the system, damping ratio, transfer function gain and perfectly accurate sensor measurements. However, in practice, we generally do not expect the residual vibrations to be damped out with one impulse application. Instead, we set the safety gain K_s to less than 1. After the first impulse application, we should observe decaying tip vibrations due to the cancellation of vibrations. After a suitable time, we can repeat the above process and decide on the next impulse application to further damp out the residual vibrations.

The transfer function gain $G_t = \dfrac{Q}{P}$ from the input pulse to the tip displacement can be obtained by an off-line simulation before operation and it is not required to be very accurate since we always use a conservative control effort, i.e., $K_s < 1$ for safety reasons.

5.2 Robustness and Two-pulse Control

To improve the robustness of the pulse control to the system natural frequency, we modify our one pulse control algorithm to a two-pulse control algorithm. We apply the first impulse at $t = t_{a1} = \dfrac{\pi + \phi}{\omega} - t_d$ with magnitude equal to

$$2K_s \frac{\Re P}{Q} e^{-\xi \omega_0 (t_{a1} + t_d)}$$

(5.2.1)

and the second impulse at $t_{a2} = \dfrac{2\pi + \phi}{\omega} - t_d$ with magnitude equal to

$$K_s \frac{\Re P}{Q} e^{-\xi \omega_0 (t_{a2} + t_d)} \qquad (5.2.2)$$

if $t_{a1} > t_n$, otherwise we apply the first impulse at $t = t_{a1} = \dfrac{2\pi + \phi}{\omega} - t_d$ with magnitude equal to

$$-2K_s \frac{\Re P}{Q} e^{-\xi \omega_0 (t_{a1} + t_d)} \qquad (5.2.3)$$

and the second impulse at $t = t_{a2} = \dfrac{3\pi + \phi}{\omega} - t_d$ with magnitude equal to

$$-K_s \frac{\Re P}{Q} e^{-\xi \omega_0 (t_{a2} + t_d)} \qquad (5.2.4)$$

The modification here from a one-pulse scheme to a two-pulse scheme is conceptually equivalent to Singer's extension of two-pulse pre-shaping to three-pulse pre-shaping [39]. Robustness to uncertainty in the natural frequency will be verified by a simulation shown later in this chapter.

5.3 Implementation

In practice, it is always a problem for a servo to produce discontinuous torque. To implement the control algorithm described above, we make a modification by using sinusoidal pulses to activate cancelling vibrations instead of impulses. In our control design, because we apply inverse dynamics control, it is easy to produce a sinusoidal like

continuous pulse torque profile by commanding the joint to follow an acceleration trajectory

$$a = K_s \frac{1}{G_t} \Re \left(1 - \cos\left(\frac{t}{t_w} 2\pi\right) \right)$$

(5.3.1)

where t_w is the pulse width which should be much smaller than the first-order vibration period, but not close to any higher-order vibration period; $\Re$ is the measured tip vibration magnitude and $G_t = \frac{Q}{P}$ is the transfer function gain from the commanded acceleration to the tip displacement.

As mentioned above, the transfer function gain G_t can be obtained off-line by a computer simulation. In our simulation, we set up the RMS at the final configuration of the task, i.e. Configuration C (Figure 2.7) carrying a 5000 Kg payload. Inverse dynamics control and flexible-joint control are implemented, and we apply a commanded joint acceleration in shoulder yaw and shoulder pitch as shown in Figure 5.1 while the other joints are locked.

$$a = 0.005\left(1 - \cos\left(\frac{t}{1.4} 2\pi\right) \right)$$
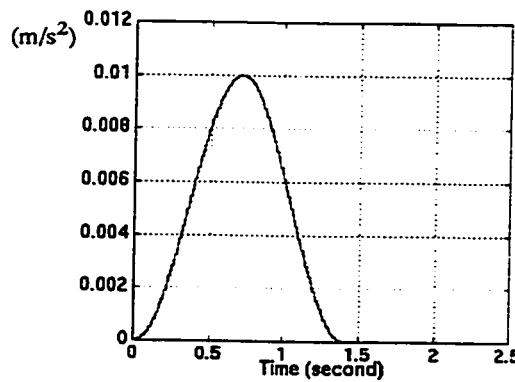
Figure 5.1 Sinusoidal-type pulse function
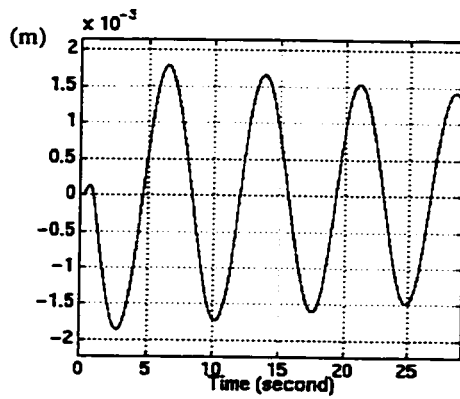
Figure 5.2 End-effector "in-plane" displacement
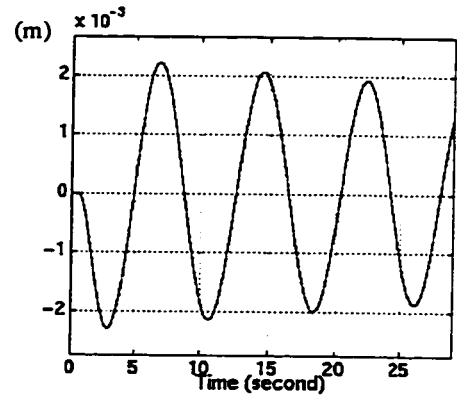
Figure 5.3 End-effector "out-of-plane" displacement

We observe the "in-plane" and "out-of-plane" tip displacements shown in Figure 5.2 and Figure 5.3, and simply calculate the gain G_t as:

Table 5.1 Transfer function gains

	$\frac{1}{G_t}$	G_t
in-plane	2.78	0.36
out-of-plane	2.22	0.44

For the RMS, the link vibrations can be separated into in-plane and out-of-plane vibrations as described in Chapter 2. Both shoulder pitch and elbow pitch joints can excite the in-plane vibrations. It is not straightforward to design an algorithm to excite cancellation vibrations at the end-effector by applying impulses from both joints simultaneously. But if we only apply an impulse at the shoulder pitch joint while keeping the elbow pitch "locked", then the problem is simplified to that for a single link. Due to the limitation on the brake torque of the RMS, we apply a control (servo) lock instead of a brake lock. The elbow is "locked" by commanding zero motion, i.e. zero velocity, zero acceleration for this joint.

70

5.4 Simulations

To demonstrate the efficiency of the pulse active damping control algorithm and the robustness of the two-pulse control scheme, several computer simulations were carried out.

The task to be accomplished is as follows: The RMS with a 5,000 kg payload starts from configuration C and executes a small maneuver, where the shoulder yaw, shoulder pitch and elbow pitch joints rotate $\frac{\pi}{512}$ in 2 seconds. No signal pre-shaping is applied in this simulation.

Without pulse active damping, the first simulation was carried out to demonstrate the residual vibrations after the end of motion at t=2 seconds. Figures 5.4.a and b show the "in-plane" and "out-of-plane" end-effector displacements. Due to the system structural damping ratio ($\xi \approx 0.001$), it is not surprising that the less damped tip oscillations last for a long time after the maneuver has been completed.
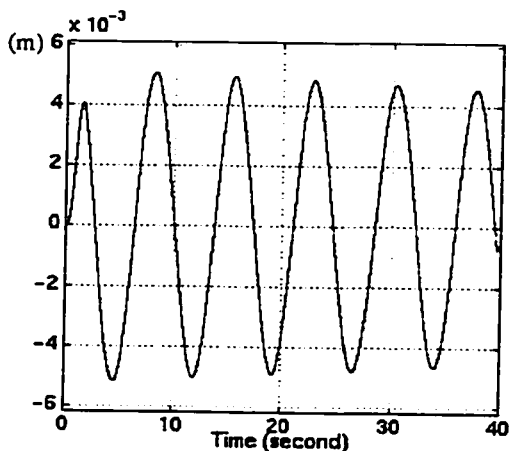
Figure 5.4.a No pulse active damping
End-effector "in-plane" deflection
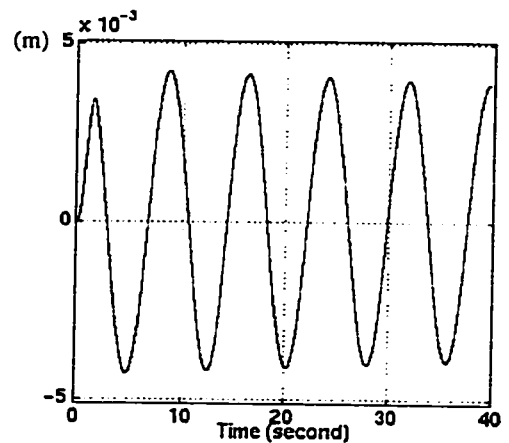
Figure 5.4.b No pulse active damping
End-effector "out-of-plane" deflection

Next, we are going to apply active pulse control in several situations. The gain factor K_s is set to 0.75, i.e. here we apply only 75% effort in cancelling the vibration. For comparison, pulse control is applied only once on the residual vibration. For practical

implementation, we can always re-measure the residual vibration, and decide the next application of control pulse. And this repeating application approach is adopted in next Chapter.

The second simulation was done with one-pulse control assuming that the damped system natural frequency and damping ratio at the configuration are known to be approximately 0.8267 rad/sec and 0.005 respectively, while the true values are ω = 0.8055 and ω = 0.8378 for shoulder yaw and shoulder pitch respectively. Figure 5.5.a and Figure 5.5.b show the "in-plane" and "out-of-plane" end-effector displacements. Around 65-75% of residual vibrations have been damped out by single one-pulse control application. They show the effectiveness of pulse active damping in controlling residual vibrations.
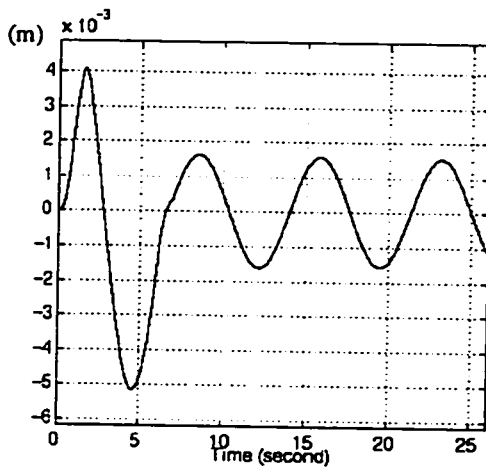
Figure 5.5.a One pulse active damping:
end-effector "in-plane" deflection
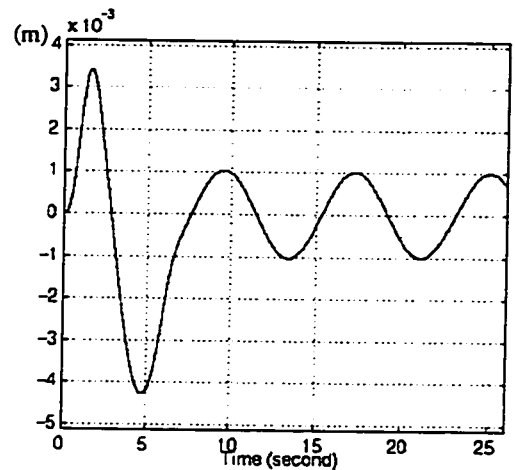
Figure 5.5.b One pulse active damping:
end-effector "out-of-plane" deflection

The third simulation was done with one-pulse control, but assuming that the damped system natural frequency and damping ratio at configuration C are not known precisely, where the estimated damped system natural frequency and damping ratio are ω = 1.047 rad/sec and ξ = 0.01 respectively, i.e., there is more than 20% error in the estimated system frequency for both joints. Figure 5.6.a and Figure 5.6.b show the "in-

plane" and "out-of-plane" end-effector displacements. With a larger error in the estimated system frequency, the one-pulse control does not behave as well as desired, only 30-35% of residual vibrations have been damped out.
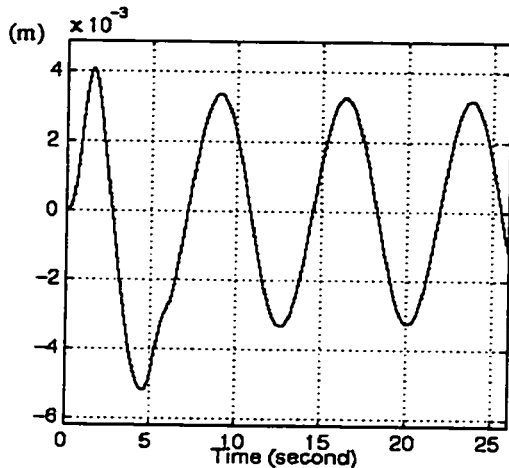
Figure 5.6.a One pulse active damping with 20% error: End-effector "in-plane" deflection
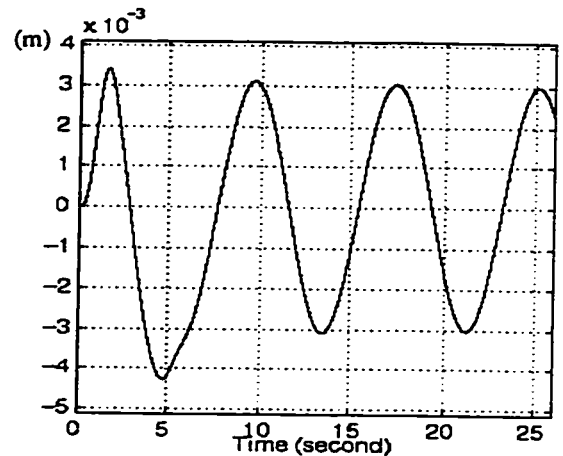
Figure 5.6.b One pulse active damping with 20% error: End-effector "out-of-plane" deflection

The last simulation was done with a two-pulse control, using the same values as in the third simulation, i.e., 20% error in the damped natural frequency. Figure 5.7.a and Figure 5.7.b show the "in-plane" and "out-of-plane" end-effector displacements. 65-70% of residual vibrations have been damped out, which give the similar performance as the one-pulse control without error in natural frequency. This shows the improved robustness of the two-pulse control algorithm.
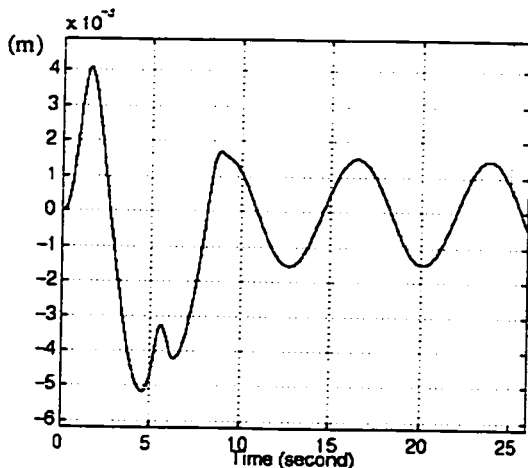
Figure 5.7.a Two pulse active damping with 20% error: End-effector "in-plane" deflection
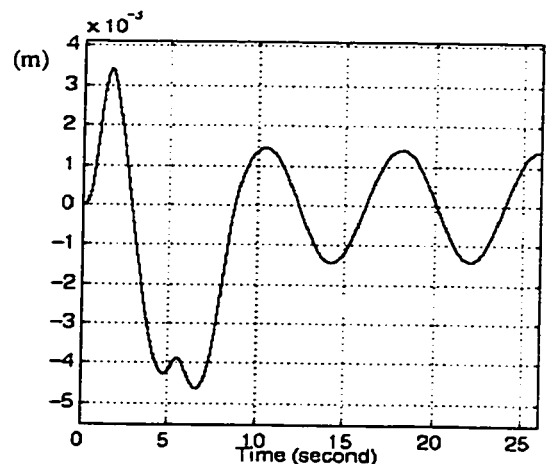
Figure 5.7.b Two pulse active damping with 20% error: End-effector "out-of-plane" deflection

5.5 Experiment

An experiment to demonstrate the one-pulse active damping control strategy was carried out on a TITAN II manipulator holding a highly flexible beam as shown in Figure 5.8. The wrist yaw joint is used to excite beam vibrations and to control the vibrations. The vibrations are measured by the accelerometer attached to the end of the beam.

The beam is first excited by a horizontal motion induced by a wrist yaw pulse as shown in Figure 5.9.a. The resulting tip acceleration is plotted in Figure 5.9.b. It shows that the dominant first-order vibration frequency is around 3.43 rad/sec and the damping is close to zero.
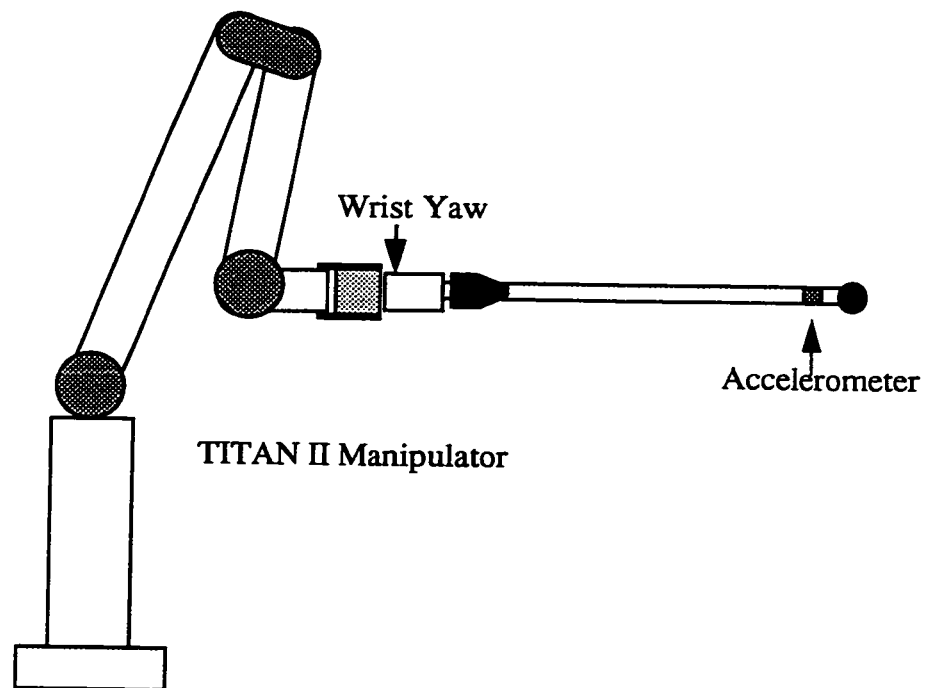
Figure 5.8 Manipulator used for the experiment
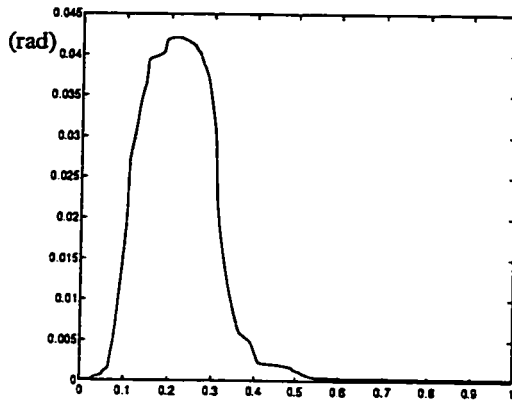
Figure 5.9.a Joint pulse motion
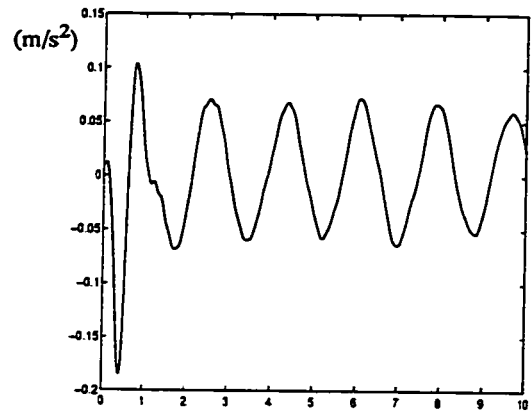
Figure 5.9.b Tip acceleration

Next, we performed another experiment by commanding the wrist yaw joint to produce a cancelling joint motion pulse following the first exciting pulse as shown in Figure 5.10.a. The two pulses are separated by one and half times the period of the natural vibration, i.e. 2.75 seconds. The magnitude of the second pulse is about 90% of the exciting pulse. The measured acceleration of the tip vibration is plotted in 5.10.b which shows that the dominant tip vibration has been successfully damped out.
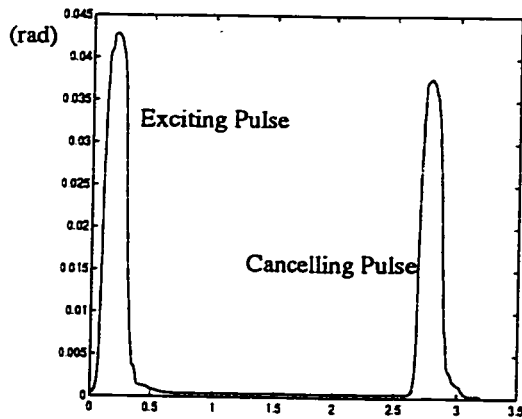
Figure 5.10.a Joint pulse motion
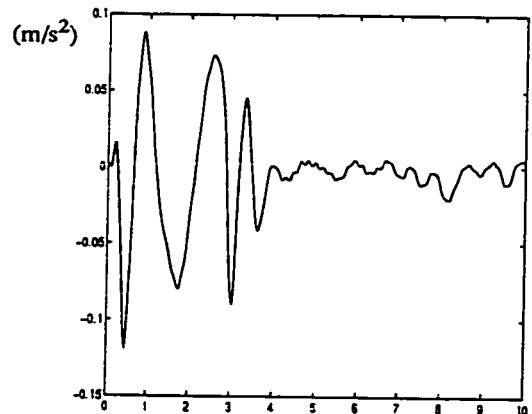
Figure 5.10.b Tip acceleration

Chapter 6

Design Example

In this chapter, control strategies discussed in previous chapters are applied in a controller design example. The integrated control architecture is shown schematically in Figure 6.1.

The task is separated into two parts. Part I of the task for this design is to maneuver the first three links of the RMS with a 500Kg payload from configuration A to configuration B. Part II consists of transporting a 5,000Kg payload from configuration B to configuration C.

.

Table 6.1 Task description

Joint	Part I From A to B		Part II From B to C	
	Start at $t_0 = 0$ sec	End at $t_{end} = 18$ sec	Start at $t_0 = 0$ sec	End at $t_{end} = 18$ sec
Shoulder Yaw (rad)	0	$\dfrac{\pi}{2}$	$\dfrac{\pi}{2}$	$\dfrac{\pi}{4}$
Shoulder Pitch (rad)	0	$\dfrac{2\pi}{3}$	$\dfrac{2\pi}{3}$	$\dfrac{\pi}{3}$
Elbow Pitch (rad)	0	$-\dfrac{2\pi}{3}$	$-\dfrac{2\pi}{3}$	$-\dfrac{\pi}{2}$
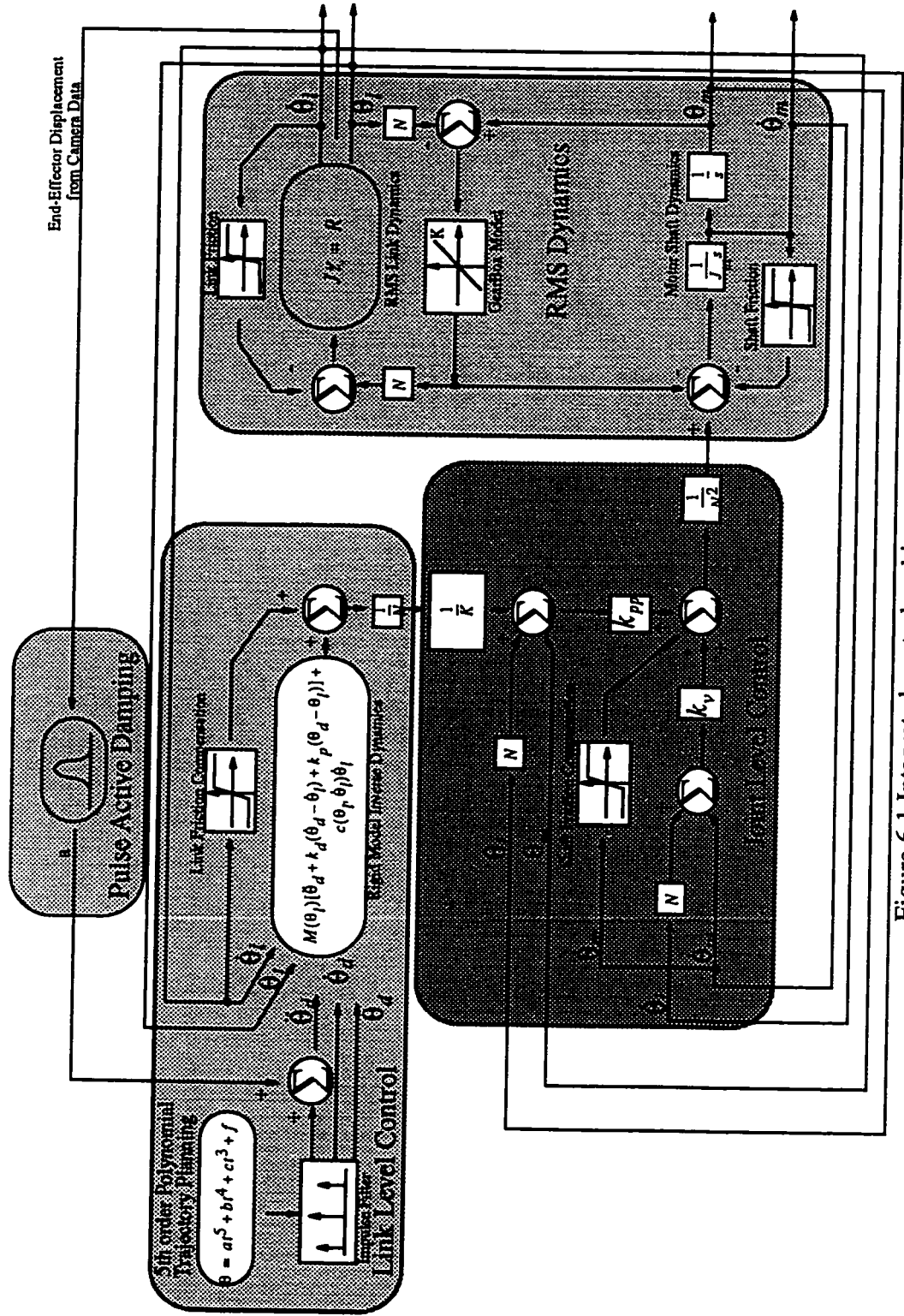
Figure 6.1 Integrated control architecture

The second part of the task is intended to accelerate RMS fast enough to excite large end-effector vibrations. Pulse active damping is applied to damp out the residual vibrations, and its performance is demonstrated.

6.1. Trajectory Planning

A 5th-order polynomial trajectory is calculated to satisfy the desired start and end point positions for each joint as defined in Table 6.1, in addition to the velocity and acceleration constraints of the start and end points:

$$\dot{\theta}_0 = 0 \text{ rad/s} \quad \ddot{\theta}_0 = 0 \text{ rad/s}^2$$

$$\dot{\theta}_{end} = 0 \text{ rad/s} \quad \ddot{\theta}_{end} = 0 \text{ rad/s}^2$$

The resulting trajectory is of the form (6.1.1)

$$\theta(t) = at^5 + bt^4 + ct^3 + \theta_0 \tag{6.1.2}$$

where the coefficients a, b, c are given in Table 6.2.a and b for Part I and II respectively

Table 6.2.a Part I: 5th-order polynomial trajectory coefficients

Joint	a	b	c	θ_0
Shoulder Yaw	0.4988×10^{-5}	-0.2245×10^{-3}	$0.2693 \times 10\text{-}3$	0
Shoulder Pitch	0.6650×10^{-5}	-0.2993×10^{-3}	0.3591×10^{-3}	0
Elbow Pitch	-0.6650×10^{-5}	0.2993×10^{-3}	-0.3591×10^{-3}	0

Table 6.2.b Part II: 5th-order polynomial trajectory coefficients

Joint	a	b	c	θ_0
Shoulder Yaw	-0.2494×10^{-5}	0.1122×10^{-3}	-0.1347×10^{-2}	$\dfrac{\pi}{2}$
Shoulder Pitch	-0.3325×10^{-5}	0.1496×10^{-3}	-0.1796×10^{-2}	$\dfrac{2\pi}{3}$

Joint	a	b	c	θ_0
Elbow Pitch	0.1663×10^{-5}	-0.7482×10^{-4}	0.8978×10^{-3}	$\dfrac{2\pi}{3}$

6.2 Pre-Shaping Filter Design

The design of a pre-shaping filter requires knowledge of the structural natural vibration frequency. We separate the joint work space for each part of the task into four equal regions and measure the impulse response (as in Chapter 2) for each of the first three joints. The results are given in Table 6.3.a for the Part I (A to B) and in Table 6.3.b for Part II (B to C).

Table 6.3.a Vibration frequency (rad/sec) along the trajectory from A to B

Configuration $[\theta_1, \theta_2, \theta_3]$ rad	Shoulder Yaw	Shoulder Pitch	Elbow Pitch
$[0, 0, 0]$	2.5	2.42	2.32
$\left[\dfrac{\pi}{8}, \dfrac{\pi}{6}, -\dfrac{\pi}{6}\right]$	1.8	1.99	2.51
$\left[\dfrac{\pi}{4}, \dfrac{\pi}{3}, -\dfrac{\pi}{3}\right]$	1.5*	2.16	2.68
$\left[\dfrac{3\pi}{8}, \dfrac{\pi}{2}, -\dfrac{\pi}{2}\right]$	2.33	2.56	2.95
$\left[\dfrac{\pi}{2}, \dfrac{2\pi}{3}, -\dfrac{2\pi}{3}\right]$	2.24	2.96	1.5*
Averaged	2.22	2.4	2.64

* data which are dropped off when averaging because they are away from most of the

others.

Table 6.3.b Vibration frequency (rad/sec) along the trajectory from B to C

Configuration $[\theta_1, \theta_2, \theta_3]$ rad	Shoulder Yaw	Shoulder Pitch	Elbow Pitch
$\left[\dfrac{\pi}{2}, \dfrac{2\pi}{3}, -\dfrac{2\pi}{3}\right]$	0.8976	1.244	1.047
$\left[\dfrac{7\pi}{16}, \dfrac{7\pi}{6}, -\dfrac{15\pi}{24}\right]$	0.8976	1.142	1.186
$\left[\dfrac{6\pi}{16}, \dfrac{\pi}{2}, -\dfrac{7\pi}{12}\right]$	0.8727	1.047	1.083
$\left[\dfrac{5\pi}{16}, \dfrac{5\pi}{12}, -\dfrac{13\pi}{24}\right]$	0.8055	0.8976	1.065
$\left[\dfrac{\pi}{4}, \dfrac{\pi}{3}, -\dfrac{\pi}{2}\right]$	0.8055	0.8378	1.030
Averaged	0.8558	1.034	1.0822

In the first part of the simulation, we use the "averaged" vibration frequency along the trajectory to design the pre-shaping filter. For the second part of the task, we demonstrate the effectiveness of the pulse active damping algorithm by taking the estimated vibration frequency at the final configuration C in designing the pre-filter instead of using the averaged frequencies calculated in Table 6.3.b.

Since the vibration frequency varies along the trajectory because of configuration changes, we require the pre-shaping filter to have some degree of robustness [39], [30]. This can be achieved by increasing the filter order, i.e., the number of impulses or by using multi-impulse filters. We use a three-impulse sequence for the first part of the task and a four impulse sequence for the second part of the task. The filter coefficients are listed in Table 6.4.a for Part I and Table 6.4.b for Part II.

Table 6.4.a Three impulse filter coefficients
for Part I

Coefficients	Shoulder Yaw	Shoulder Pitch	Elbow Pitch
Δt	1.4152	1.3091	1.1901
A_0	0.2579	0.2579	0.2579
A_1	0.4999	0.4999	0.4999
A_2	0.2422	0.2422	0.2422

Table 6.4.b Four impulse filter coefficients
for Part II

Coefficient	Shoulder Yaw	Shoulder Pitch	Elbow Pitch
Δt	3.9002	3.7499	3.0501
A_0	0.1280	0.1280	0.1280
A_1	0.3779	0.3779	0.3779
A_2	0.3720	0.3720	0.3720
A_3	0.1221	0.1221	0.1221

6.3 Link Control

In the simulation, the gain factors k_p and k_d in the inverse dynamics control are tuned via simulations to obtain the final values listed in Table 6.5. The values of k_p, k_d are kept small in order to avoid system instability. In particular, when the flexible links start mov-

ing, the velocity and position errors can become large when the applied joint torque is calculated based on a rigid model. Therefore, an experimental approach is to increase the gains from zero at the beginning of the motion to the final desired value through a continuous curve. For example, in task part II, k_p, k_d were adjusted according to quadratic interpolation:

$$k_p = 36 - 0.25(t-12)^2 \qquad k_d = 12 - 0.0833(t-12)^2 \qquad t \le 12$$
$$k_p = 36 \qquad\qquad k_d = 12 \qquad\qquad\qquad t > 12 \qquad (6.3.1)$$

Table 6.5 Link control gains

	Coefficient	Shoulder Yaw	Shoulder Pitch	Elbow Pitch
Part I	k_p	27	27	27
	k_d	6	6	6
Part II	k_p	36	36	36
	k_d	12	12	12

6.4 Joint Control

The gains constants k_{pp} and k_v in (4.1.28) are also tuned by simulations to obtain the values listed in Table 6.6.

Table 6.6 Parameters for the flexible-joint perturbation control scheme

	Coefficient	Shoulder Yaw	Shoulder Pitch	Elbow Pitch
Task Part I	k_{pp}	1×10^7	1×10^7	1×10^7

Table 6.6 Parameters for the flexible-joint perturbation control scheme

	Coefficient	Shoulder Yaw	Shoulder Pitch	Elbow Pitch
	k_v	3×10^3	3×10^3	3×10^3
Task Part II	k_{pp}	1×10^7	1×10^7	1×10^7
	k_v	3×10^3	3×10^3	3×10^3

6.5 Pulse Active Damping

One-pulse control is applied at the end of the motion for Part II. In Part II, due to the heavier payload and fast motion, larger residual vibrations can be observed. The pulse active damping control is necessary to rapidly damp out the residual oscillations. The transfer function gain $G_t = \frac{Q}{P}$ and safety gain K_s are set so that $\frac{K_s}{G_t} = 1.8$ for shoulder yaw and shoulder pitch control.

6.6 Simulation Results

Simulations were performed for the RMS using SIMULINK and the above specified control parameters.

Part I: With a 500Kg payload, moving from A to B, with friction compensation and with three impulse pre-shaping designed using the averaged frequency along the trajectory.

The simulation results are plotted in Figures 6.2.a-c for end-effector errors in the X, Y and Z directions respectively. Figure 6.2.d shows the errors in the first three joints, Figure 6.2.e plots the first-order "in-plane" and "out-of-plane" elastic mode coordinates for links 2 and 3.

Figure 6.2.a Part I:
End-effector error in X direction

Figure 6.2.b Part I:
End-effector error in Y direction

Figure 6.2.c Part I:
End-effector error in Z direction
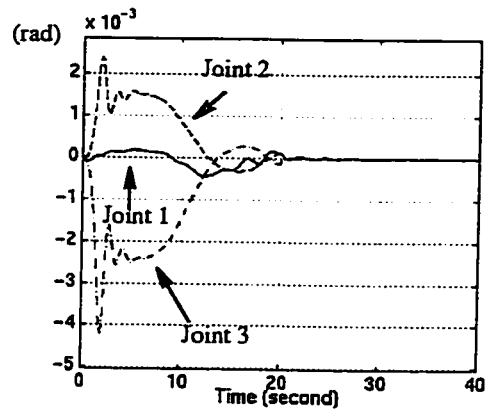
Figure 6.2.d Part I:
Errors in the first three joint

Figure 6.2.e Part I: First-order
"in-plane" and "out-of-plane" elastic coordinates

The simulation results show the efficiency of the integrated controller. Due to the small residual vibrations, pulse active damping is not needed here. But for faster motion and with a large change in the configuration such as that in Part II, pulse active damping becomes necessary.

Part II: A 5,000 Kg payload, moving from B to C with a four-impulse pre-shaping filter designed using the final configuration system frequency and applied on the 5th order polynomial trajectory.

For comparison purposes, several simulations were carried out for Part II:

Case 1: Without signal pre-shaping and without pulse active damping

Only inverse dynamics control and flexible-joint control were implemented. The simulation results are plotted in Figures 6.3.a-c for end-effector errors in the X, Y and Z directions respectively. Figure 6.3.d shows the errors in the first three joints, Figure 6.3.e and Figure 6.3.f plot the first-order and second-order "in-plane" and "out-of-plane" elastic mode coordinates for links 2 and 3 respectively. Large residual vibrations can be seen in these figures.

Figure 6.3.a Part II:
End-effector error in X direction

Figure 6.3.b Part II:
End-effector error in Y direction

Figure 6.3.c Part II:
End-effector error in Z direction

Figure 6.3.d Part II:
Errors in the first three joint

Figure 6.3.e Part II: First order
"in-plane" and "out-of-plane" elastic coordinates

Figure 6.3.f Part II: Second order
"in-plane" and "out-of-plane" elastic coordinates

Case 2: With signal pre-shaping, but without pulse active damping

The four-impulse signal pre-shaping filter was applied on the desired joint trajectories for the first three joints. The simulation results are plotted in Figures 6.4.a-c for end-effector errors in the X, Y and Z directions respectively. Figure 6.4.d shows the errors in the first three joints, Figure 6.4.e and Figure 6.4.f plot the first-order and second-order "in-plane" and "out-of-plane" elastic mode coordinates for links 2 and 3 respectively.
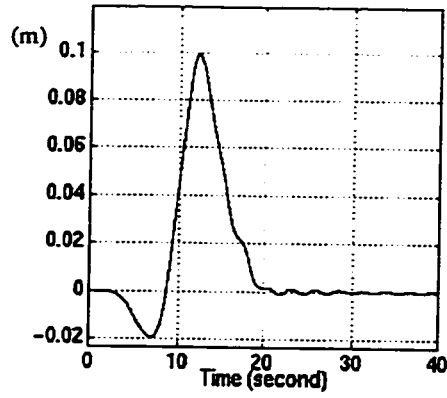
Figure 6.4.a Part II:
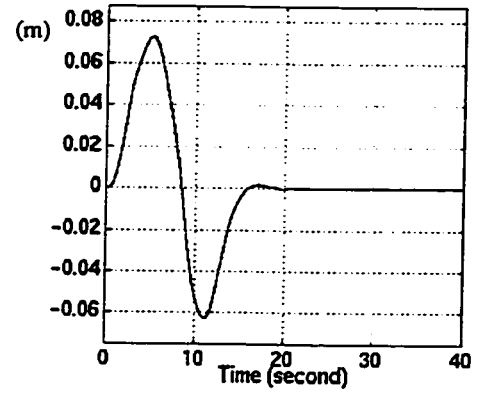End-effector error in X direction

Figure 6.4.b Part II:
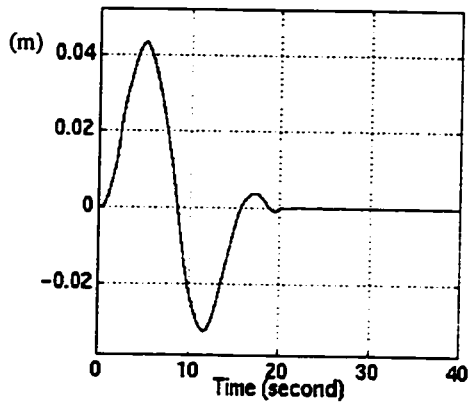End-effector error in Y direction


Figure 6.4.c Part II:
End-effector error in Z direction
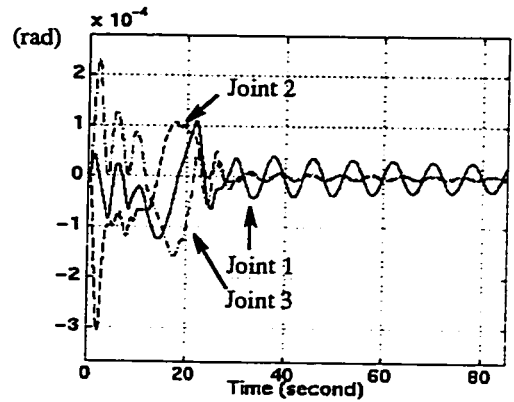
Figure 6.4.d Part II:
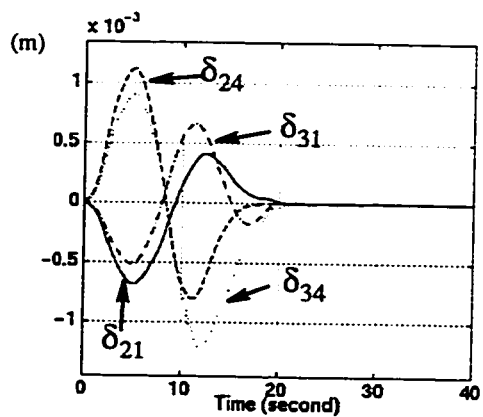Errors in the first three joint
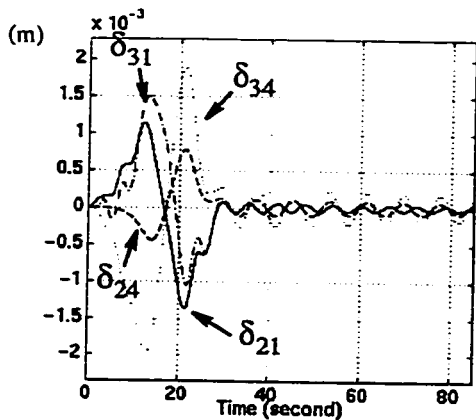
Figure 6.4.e Part II: First-order
"in-plane" and "out-of-plane" elastic coordinates
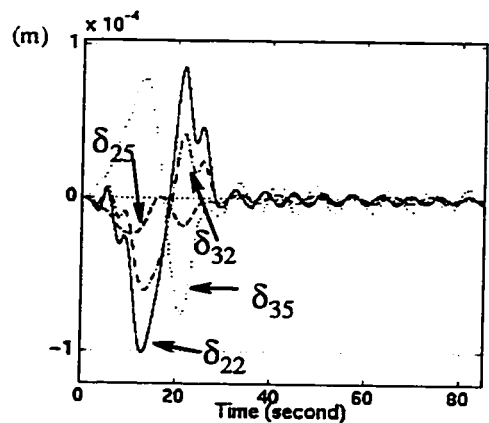
Figure 6.4.f Part II: Second-order
"in-plane" and "out-of-plane" elastic coordinates

87

As can be seen, the residual vibrations are much smaller than in the case without signal pre-shaping applied to the trajectories, and only 20% of the residual vibrations are observed. This shows the effectiveness of the signal pre-shaping algorithm. The remained residual vibrations can still be observed, these can be damped out by pulse active damping control as the next simulation shows.

Case 3: With signal pre-shaping, pulse active damping

Pulse active damping control is activated at the end of the RMS maneuver to rapidly damp out the end effector residual oscillations. The simulation results are plotted in Figures 6.5.a-c for end-effector errors in the X, Y and Z directions respectively. Figure 6.5.d shows the errors in the first three joints, Figure 6.5.e and Figure 6.5.f plot the first-order and second-order "in-plane" and "out-of-plane" elastic mode coordinates for links 2 and 3 respectively.
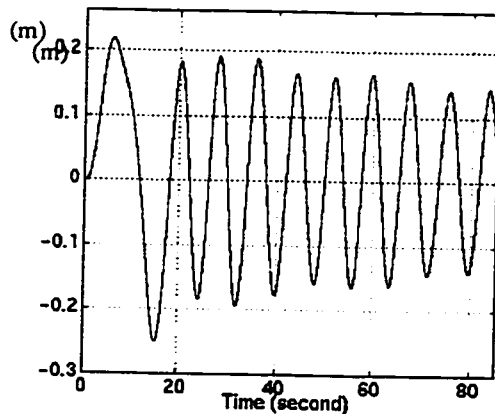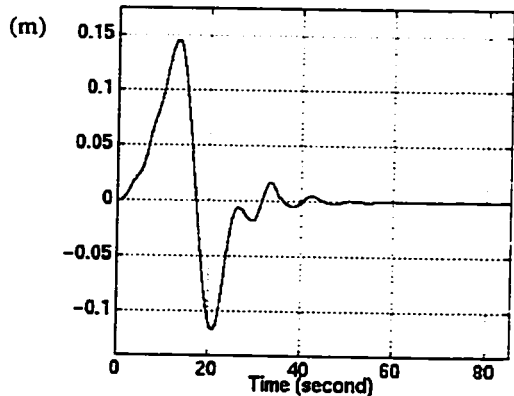

Figure 6.5.a Part II:
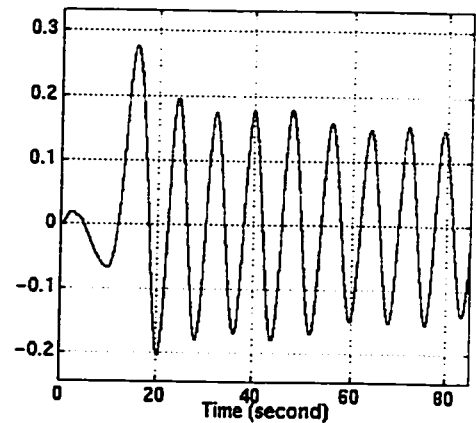End-effector error in X direction
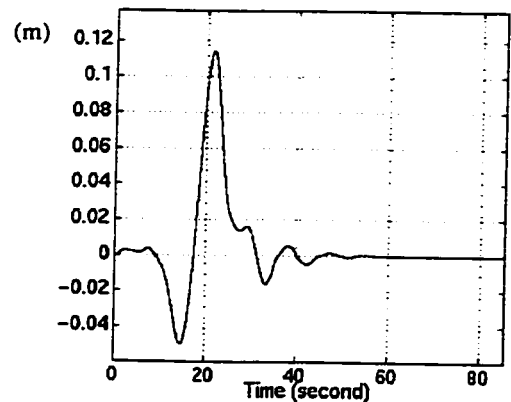
Figure 6.5.b Part II:
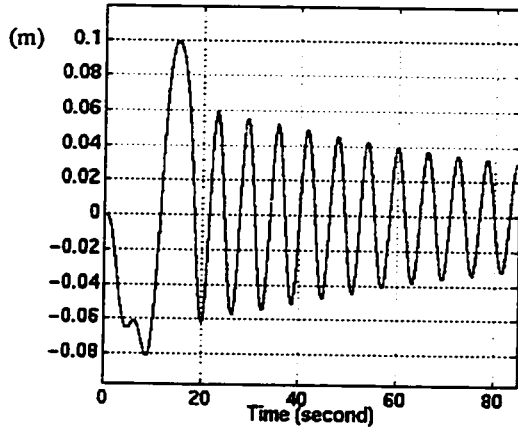End-effector error in Y direction
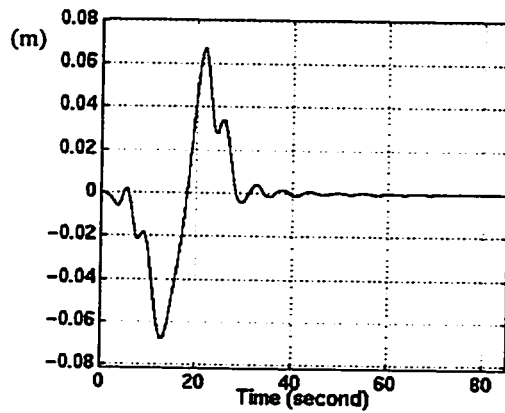
Figure 6.5.c Part II:
End-effector error in Z direction
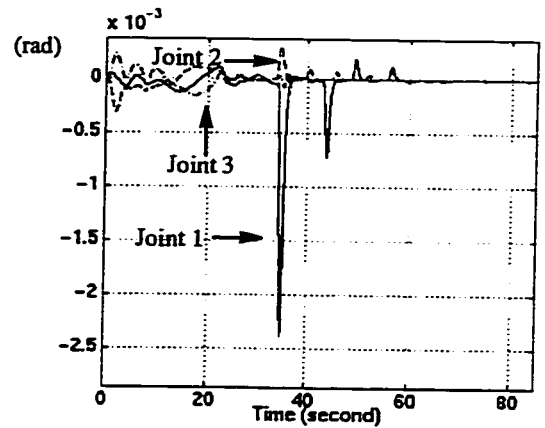
Figure 6.5.d Part II:

Errors in the first three joints
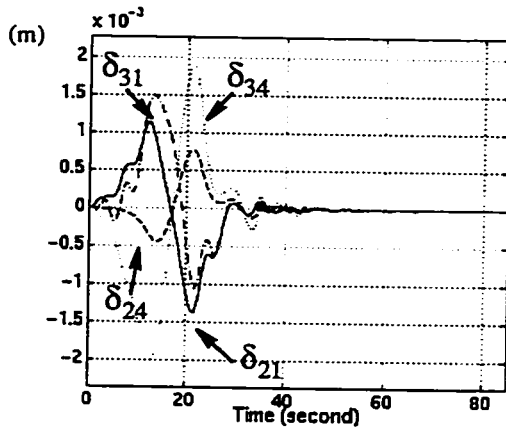
Figure 6.5.e Part II: First-order
"in-plane" and "out-of-plane" elastic coordinates
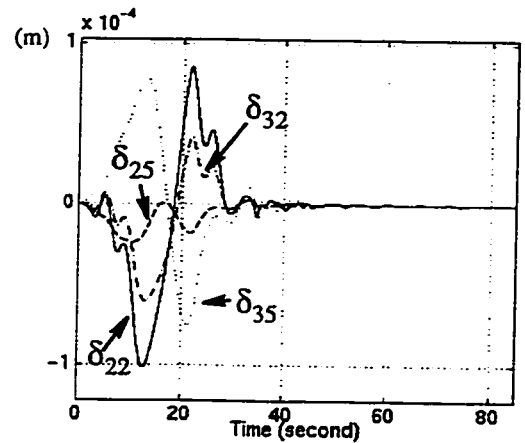
Figure 6.5.f Part II: Second-order
"in-plane" and "out-of-plane" elastic coordinates

After pulse active damping is introduced, the residual vibrations are damped out to negligible level in about 3 vibration periods. The "spike" in Figure 6.5.d is introduced by the application of the pulse active damping at this instant.

Case 4: Without signal pre-shaping, but with pulse active damping

To demonstrate the robustness of the pulse active damping algorithm to the magnitude of residual vibrations, we applied the same control as in Case 1 (without signal pre-shaping), where large residual vibrations were observed.

The simulation results are plotted in Figures 6.6.a-c for end-effector errors in the X, Y and Z directions respectively. Figure 6.6.d shows the errors in the first three joints, Figure 6.6.e and Figure 6.6.f plot the first-order and second-order "in-plane" and "out-of-plane" elastic mode coordinates for links 2 and 3 respectively.
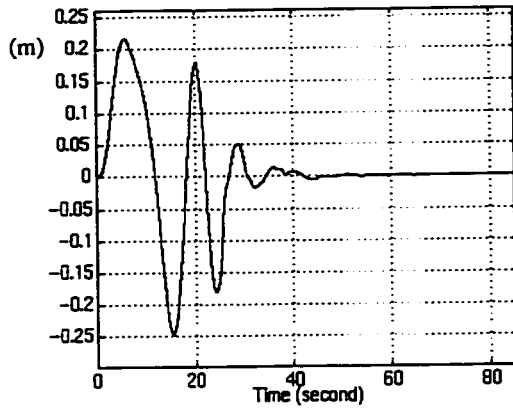
Figure 6.6.a Part II:
End-effector error in X direction
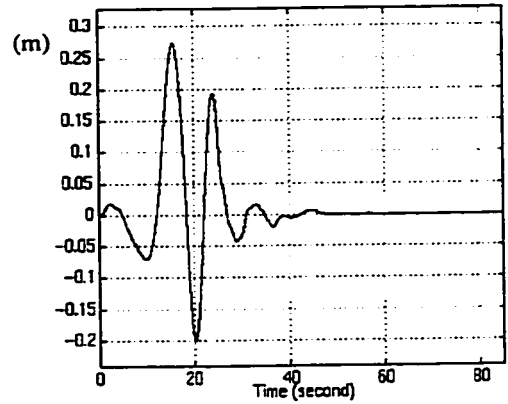
Figure 6.6.b Part II:
End-effector error in Y direction
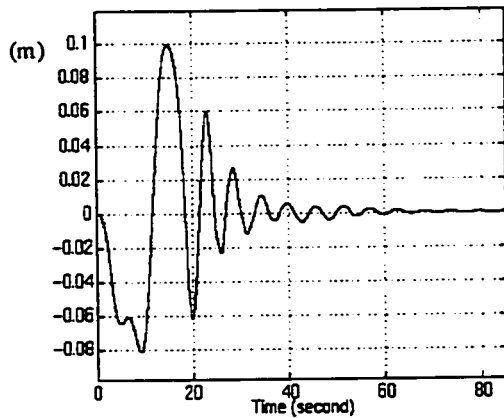
Figure 6.6.c Part II:
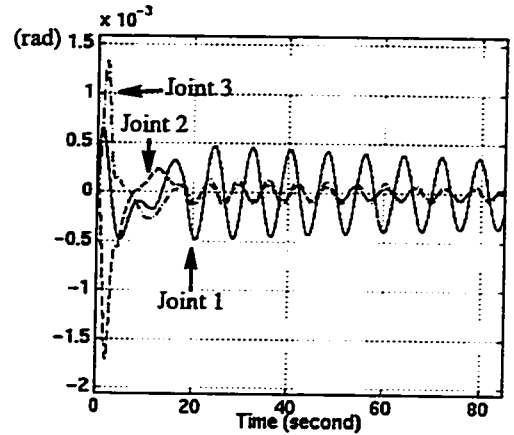End-effector error in Z direction
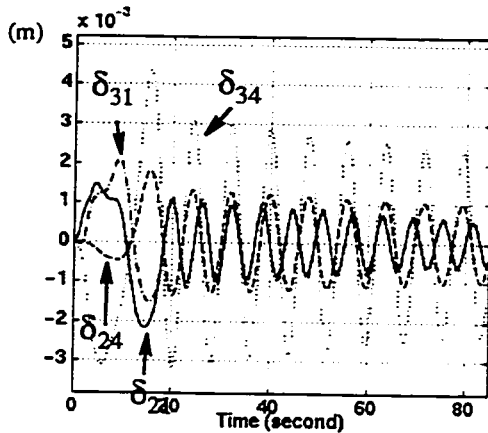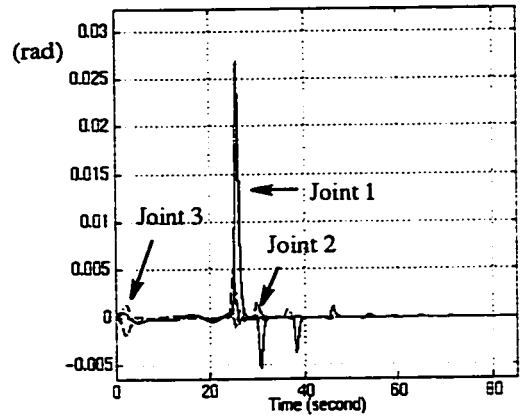
Figure 6.6.d Part II:
Errors in the first three joints
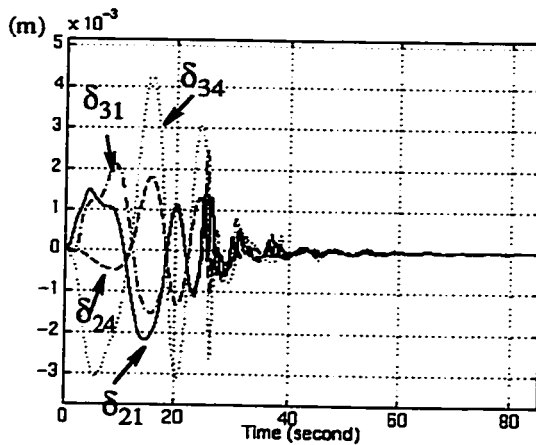
Figure 6.6.e Part II: First-order
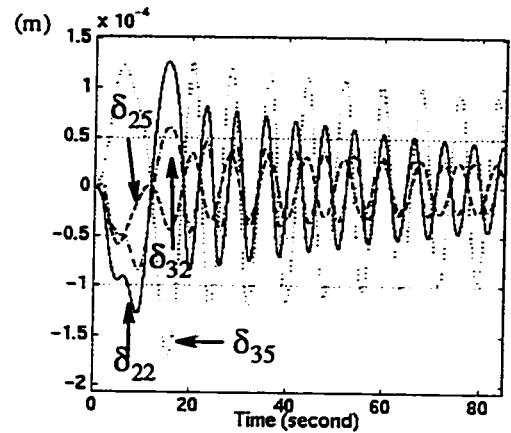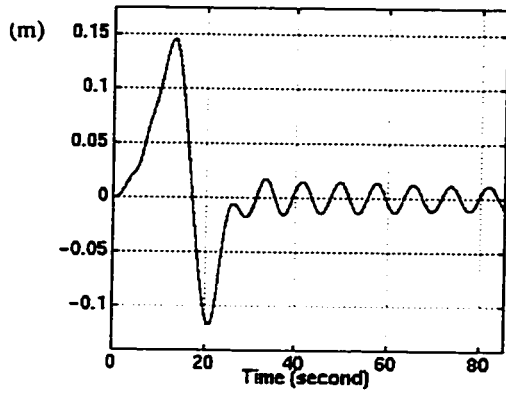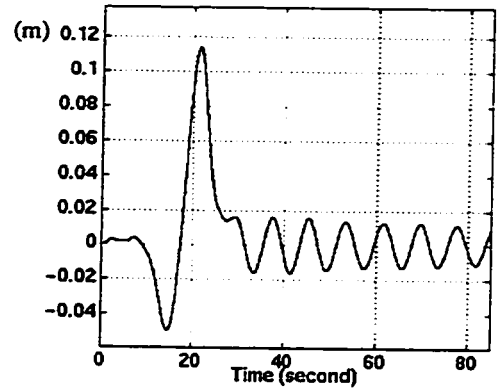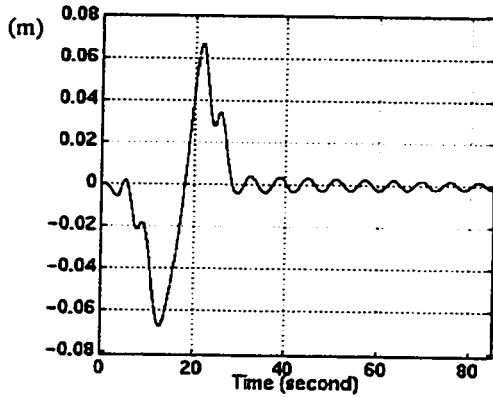"in-plane" and "out-of-plane" elastic coordinates
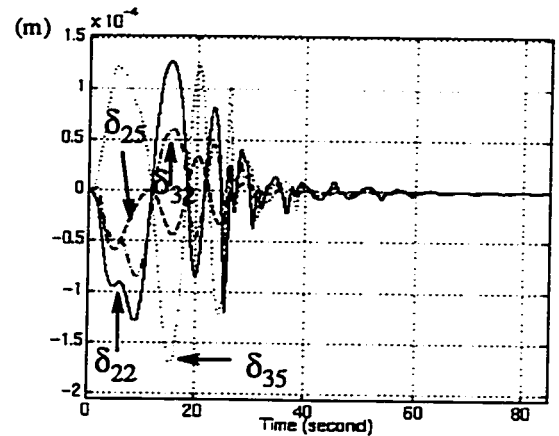
Figure 6.6.f Part II: Second-order
"in-plane" and "out-of-plane" elastic coordinates

Even though the residual vibrations are almost 5-8 times larger than those in Case 3, the same pulse active damping scheme is effective in damping out the residual vibrations in less than 4 vibration periods.

Remarks

We have previously found that heavier payloads and faster slewing motions excite larger end-effector oscillations, so that larger residual vibrations are observed at the end of the maneuver. In this section, we have show that when the payload is light, for example, 500Kg, simply applying signal pre-shaping is enough to filter out most of the system vibrations and no pulse active damping control is necessary. However, with heavier payloads and greater system uncertainty, residual vibrations become larger and it becomes more difficult to damp them out using the system's structural damping itself. Pulse active damping is effective in this situation.

91

6.7 Graphics Animation

To demonstrate the simulation results in a 3D graphics environment, a graphics animator was programmed using Open Inventor running on SGI workstations. The software is able to animate all six joint motions as well as link flexibility as illustrated by the simulation results of the previous sections.

Figure 6.7 and 6.8 show the front and rear camera views in Configuration C. The link flexibility is of the order of 0.5 meter, in comparison with the link lengths of 15 meters; its effect is invisible in the snapshots shown in Figures 6.7 and 6.8. It is visible, however, in the actual animation.
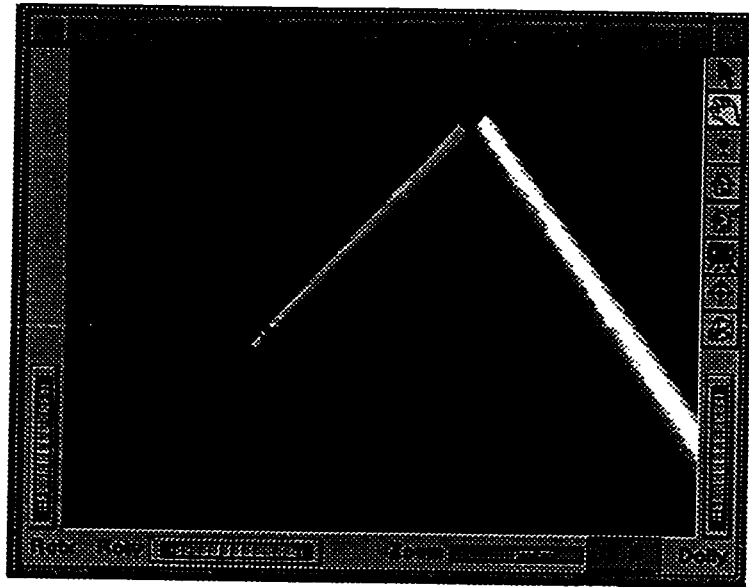
Figure 6.7 Front camera view
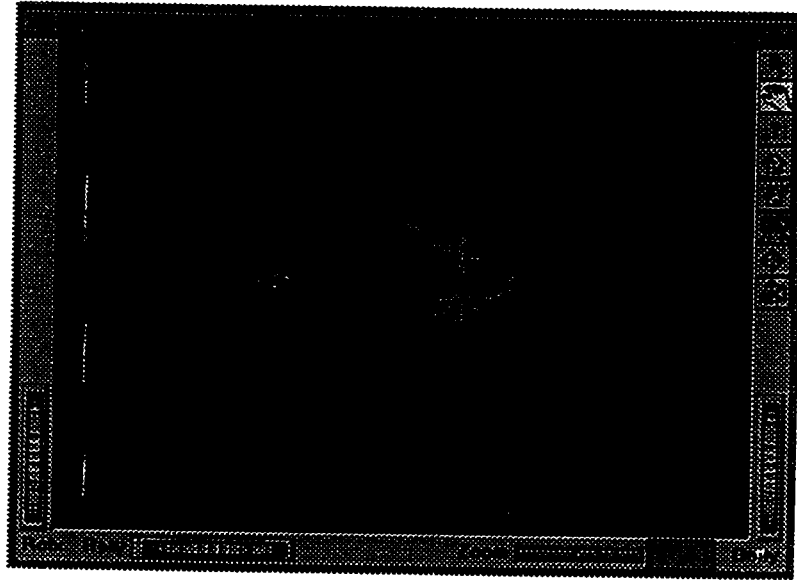
Figure 6.8 Rear camera view

Chapter 7

Conclusions and Future Research

In this thesis, a dynamic model has been constructed incorporating the rigid dynamics, servo dynamics, linear flexible-joint dynamics and flexible-link dynamics of the Remote Manipulator System. In particular, the flexible-link dynamic model includes the coupling effects of the link transverse and torsional vibrations between the two long links of the RMS. The constructed model enable us to model and study the following major characteristics of the RMS dynamics:

(1) Link flexibility and coupling effects of link vibrations.

(2) Low system natural frequencies.

(3) Varying system natural frequencies with varying payload and/or varying configurations.

(4) Joint flexibility.

This model was used to propose a controller design for RMS and provide validation for it.

The aim of the controller design was to design a highly effective controller with low computational cost for handling the vibrations in RMS motions. Three major components of the controller are:

(1) Pre-shaping of the planned trajectories: It was shown that this approach successfully filters out most of the vibration components from the planned trajectories, and as a result,

residual vibrations are reduced significantly.

(2) Rigid body based inverse dynamics control: This control approach gives an "almost" decoupled system, when the assumptions of good rigid model and low flexibility are satisfied.

(3) Pulse active damping control: This activates "opposing" vibrations to cancel out the observed residual vibrations. As verified by experimental results and computer simulations, this control approach can quickly damp out residual vibrations.

The essential characteristics of the dynamics agree with real test data obtained fro the RMS.

The integrated control architecture was successfully tested on the RMS model. This controller design which is efficient and easy to implement, leads to a lower end-effector vibrations and rapid damping of residual vibrations. An experiment was carried out on a Titan II manipulator to test the control efficiency of pulse active damping. Our simulation results for the RMS indicate that pulse active damping control can be applied to the RMS to significantly reduce the waiting time for the residual vibrations to die out. A 3D graphics animator was also developed using Open Inventor on an SGI workstation to visually demonstrate the simulation results.

There are a number of issues that were not addressed in this thesis or were addressed in a limited way. These are as follow:

(1) The controller consists of a rigid-body based inverse dynamics control with additional features to reduce / eliminate the effect of flexibility. In other words, flexibility effects have been regarded as disturbance acting on an essentially rigid system. For the case of larger link elasticity, such a approach will need to be modified.

(2) Application of PAD while damping out the low frequency vibration, may excite higher order vibrations. Therefore, a variation of the PAD approach may be necessary which applies band-limited pulses.

(3) Robustness of the PAD approach can be improved by incorporating an online scheme

for estimating the system vibration frequencies.

(4) We have used linear models for joint flexibility. For greater accuracy, it would be necessary to use nonlinear models.

The above issues are interesting and practically useful topics for further research in this area.

References

[1] T.E. Alberts, H. Xia, and Y. Chen, "Dynamic Analysis to Evaluate Viscoelastic Passive Damping Augmentaion for the Space Shuttle Remote Manipulator System," *ASME Journal of Dynamic Systems, Measurement, and Control*, Vol.114, Sept., 1990, pp.468-475.

[2] S. Ananthakrishnan, "Adaptive Tachometer Feedback Augmentation of the Shuttle Remote Manipulation Control System", *IEEE International Conference on Robotics and Automation*, 1995, pp.39-44.

[3] B. Armstrong-Helouvry, *Control of Machines with Friction*, Kluwer Academic Publishers 1991.

[4] W. Beres, J.Z. Sasiadek and G. Vukovich, "Control and Dynamic Analysis of Multlink Flexible Manipulator", *IEEE International Conference on Robotics and Automation*, 1993, pp.478-483.

[5] W.J. Book, "Recursive Lagrangian Dynamics of Flexible Manipulator Arms", *The International Journal of Robotics Research*, Vol.3, No.3, 1984, pp.87-101.

[6] C. Canudas, H. Olsson, K. J. Astrom and P. Lischinsky, "A New Model for Control of Systems with Friction", *IEEE Transactions on Automatic Control*, Vol.40, No.3, March 1995, pp.419-425.

[7] S. Cetinkunt, W.J. Book,"Symbolic Modeling of Flexible Manipulators", *IEEE International Conference on Robotics and Automation*, 1987, pp.2074-2080.

[8] S. Cetinkunt, W.J. Book, "Flexibility Effects on the Control Systems Performance of Large Scale Robotic Manipulators", *The Journal of the Astronautical Sciences*, Vol.38, No.4, October-December 1990, pp.531-556.

[9] M. Corless, S. Zenieh, "A New Control Design Methodology for Robotic Manipulators with Flexible Joints", *Proceedings of the American Control Conference*, June 1995, pp.4316-4320.

[10] J.J. Craig, *Introduction to Robotics Mechanics and Control*, Addison-Wesley Publishing Company, 2nd edition, 1989.

[11] X. Ding, T.J. Tarn and Bejczy, "A General Dynamic Model of Flexible Robot Arms for Control", *IEEE International Conference on Robotics and Automation*, 1989, pp.1678-1683.

[12] A.R. Fraser, Daniel, Ron W., *Perturbation Techniques for Flexible Manipulators*, Kluwer Academic Publishers 1991.

[13] H. Geniele, R.V. Patel and K. Khorasani, "Control of a Flexible-Link Manipulator", *IEEE International Conference on Robotics and Automation*, 1995, pp.1217-1222.

[14] F. Ghorbel, J.Y. Hung and M.W. Spong, "Adaptive Control of Flexible-Joint Manipulators", *IEEE Control Systems Magazine*, Dec. 1989, pp.9-13.

[15] S.W. Groesberg, "Advanced Mechanics", Wiley, New York, 1968.

[16] K.L. Hillsley, S. Yurkovich, "Vibration Control of a Two-Link Flexible Robot Arm," *Proceedings of the 1991 IEEE International Conference on Robotics and Automation*, Sacramento, California, April 1991, pp. 2121-2126.

[17] J.M. Hyde, W.P. Seering, "Using Input Command Pre-Shaping to Suppress Multiple Mode Vibration," *Proceedings of the 1991 IEEE International Conference on Robotics and Automation*,

Sacramento, California, April 1991, pp. 2604-2609.

[18] P.C. Hughes, "Dynamics of a Chain of Flexible Bodies", *The Journal of the Astronautical Sciences*, Vol.XXVII, No.4, pp.359-380, 1979.

[19] S. Kalaycioglu, "Identification of Stiffness/Damping Matrices and Modal Parameters of SSRMS", CSA-DSM-100, 1994.

[20] S. Kalaycioglu, "Robotics Evaluation and Characterization (REACH) of the SSRMS", *Astronautical*, pp.969-978, 1995.

[21] W. Khalil, F. Boyer, "An Efficient Calculation of Computed torque Control of Flexible Manipulators," *IEEE International Conference on Robotics and Automation*, 1995, pp. 609-614.

[22] K. Khorasani, "Adaptive Control of Flexible Joint Manipulators", *IEEE Transaction on Robotics and Automation*, Vol.8, No.2, pp.250-167, 1992.

[23] F. Khorrami, S. Jain and A. Tzes, "Experiments on Rigid Body-Based Controllers with Input Preshaping for a Two-Link Flexible Manipulator," *IEEE Transactions on Robotics and Automation*, Vol. 10, No. 1, Feb. 1994, pp. 55-65.

[24] F. Khorrami, "Analysis of Multi-Link Flexible Manipulators Via Asymptotic Expansions," *Proceedings of the 28th conference on Decision and Control*, Tampa, Florida, Dec. 1989, pp. 2089-2094.

[25] C.L. Kirk, A. Oria and F. Hammer, "Slewing Dynamics and Vibration Control of Flexible Space Shuttle Remote Manipulator", *AAS/AIAA Astrodynamics Specialist Conference*, August 1995.

[26] P.V. Kokotovic, H.K. Khalil, O'Reilly, *Singular Perturbation Methods in Control: Analysis and Design*, Academic Press, London 1986.

[27] P.T. Kotnik, S. Yurkovich, U. Özgüner, "Acceleration Feedback for Control of a Flexible Manipulator Arm," *Journal of Robotic Systems*, 1988, pp. 181-196.

[28] L-C. Lin, K. Yuan, "A Lagrange-Euler-Assumed Modes Approach to Modeling Flexible Robotic Manipulators", *Journal of the Chinese Institute of Engineers*, Vol. 11, No.4, pp335-347, 1988.

[29] D.P. Magee, W.J. Book, "Filtering Schilling Manipulator Commands to Prevent Flexible Structure Vibration," *Proceedings of the American Control Conference*, Baltimore, Maryland, June 1994, pp. 2538-2542.

[30] D.P. Magee, W.J. Book, "Implementing Modified Command Filtering to Eliminate Multiple Modes of Vibration," *Proceedings of the American Control Conference*, San Francisco, California, June 1993, pp. 2700-2704.

[31] H.W. Mah, V.J. Modi, Y. Morita, H. Yokota, "Dynamics During Slewing and Transportational Maneuvers of the Space Station Based MRMS, *The Journal of the Astronautical Sciences*, Vol.38, N0.4, October-December 1990, pp.557-579.

[32] P.H. Meckl, W.P. Seering, "Controlling Velocity-Limited Systems to Reduce Residual Vibration," *IEEE International Conference on Robotics and Automation*, 1988, pp.1428-1433.

[33] L. Meirovitch, *Analytical Methods in Vibration*, The Macmillan Co., New York, 1967.

[34] B.R. Murphy,I. Watanabe, "Digital Shaping Filters for Reducing Machine Vibration," *IEEE Transactions on Robotics and Automation*, Vol. 8, No. 2, April 1992, pp. 285-289.

[35] NASA, "Payload Deployment and Retrieval System Simulation Database Version 1.0, Flight Support Equipment RMS Operations", Doc. No. JSC-25134, July 1991.

[36] P.K. Nguyen, P.C. Hughes, "Teleoperation: From Space Shuttle to the Space Station", *Teleoperation and Robotics in Space, Progress in Astronautics and Aeronaustics*, 1994.

[37] Y. Sakawa, Z-H. Luo, "Modeling and Control of Coupled Bending and Torsional Vibrations of Flexible Beams," *IEEE Transactions on Automatic Control*, Vol. 34, No. 9, Sep. 1989, pp. 970-977.

[38] I. Sharf, M.T. Gabriele, "Parallel Simulation Dynamics for Elastic Multibody Chains", *IEEE Transaction on Robotics and Automation*, Vol.8, No.5, Oct. 1992.

[39] N.C. Singer, "Residual Vibration Reduction in Computer Controlled Machines", Ph.D thesis, MIT Artificial Intelligence Laboratory 1989.

[40] N.C. Singer, W.P. Seering, "Preshaping Command Inputs to Reduce System Vibration," *ASME Journal of Dynamic Systems, Measurement, and Control*, Vol. 112, Mar. 1990, No.1, pp. 76-82.

[41] N.C. Singer, W.P. Seering, "Experimental Verification of Command Shaping Methods for Controlling Residual Vibration in Flexible Robots," *Proceedings of the 1990 American Control Conference*, Vol.2, 1990, pp. 1738-1744.

[42] N.C. Singer, W.P. Seering, "Using Acausal Shaping Techniques to Reduce Robot Vibration," *Proceedings of the 1988 IEEE International Conference on Robotics and Automation*, 1988, pp.1434-1439.

[43] T. Singh, G.R. Heppler, "Shaped Inputs for a Multimode System," *Proceedings of the 1993 IEEE International Conference on Robotics and Automation*, 1993, pp. 484-489.

[44] W.E. Singhose, W.P. Seering, N.C. Singer, "Shaping Inputs to Reduce Vibration: A Vector Diagram Approach," *Proceedings of the 1990 IEEE International Conference of Robotics and Automation*, 1990, pp. 922-927.

[45] M.W. Spong, M. Vidyasagar, *Robot Dynamics and Control*, John Wiley & Sons, New York, 1989.

[46] L. Tian, A.A. Goldenberg, "Robust Adaptive Control of Flexible Joint Robots with Joint Torque Feedback," *IEEE International Conference on Robotics and Automation*, 1995, pp. 1229-1234.

[47] A.P. Tzes, S. Yurkovich, "A Frequency domain Identification Scheme for Flexible Structure Control," *Proceedings of the 27th Conference on Decision and Control, Austin, Texas*, December 1988, pp. 1627-1632.

[48] A.P. Tzes, S. Yurkovich, "Adaptive Precompensators for Flexible-Link Manipulator Control," *Proceedings of the 28th Conference on Decision and Control, Tampa, Florida*, December 1989, pp. 2083-2088.

[49] J-H. Yang, F-L. Lian and L-C. Fu, "Adaptive Robust Control for Flexible Manipulators", *IEEE International Conference on Robotics and Automation*, 1995, pp.1223-1227.

[50] S. Yurkovich, F.E. Pacheco, "On-Line Frequency Domain Information for Control of a Flexible-Link Robot with Varying Payload," *IEEE Transactions on Automatic Control*, Vol. 34, No. 12, Dec. 1989, pp. 1300-1304.

[51] K. Zuo, D. Wang, "Closed Loop Shaped-Input Control of a Class of Manipulators with a Single Flexible Link," *Proceedings of the 1992 IEEE International Conference on Robotics and Automation*, Nice, France, May 1992, pp. 782-787.

[52] M. Moallem, R. V. Patel and K. Khorasani, "An Inverse Dynamics Control Strategy for Tip Position Tracking of Flexible Multi-Link Manipulators," *International Federation of Automatic Control 13th World Congress*, San Francisco, CA, Vol. A, pp. 85--90, 1996.

[53] M. Moallem, K. Khorasani and R. V. Patel, "Tip Position Tracking of Flexible Multi-Link Manipulators: An Integral Manifold Approach," *IEEE International Conference on Robotics and Automation*, Minneapolis, MN, pp. 2432--2437, 1996; to appear in *IEEE Transactions on Robotics and Automation*, 1997.

[54] M. Moallem, K. Khorasani and R. V. Patel, "Optimum Structure Design for Flexible-Link Manipulators," *IEEE International Conference on Robotics and Automation*, Minneapolis, MN, pp. 798--803, 1996.

[55] M. Moallem, R. V. Patel and K. Khorasani, "An Observer-Based Inverse Dynamics Control Strategy for Flexible Multi-Link Manipulators," *35th IEEE Conference on Decision and Control*, Kobe, Japan, 1996.

[56] G. Naganathan and A. H. Soni, "Coupling Effects of Kinematics and Flexibility in Manipulators," Int. J. Robotics Res., Vol. 6, No. 1, pp. 75-84, 1987

[57] W. H. Sunada and S. Dubowsky, "On the Dynamic Analysis and Behavior of Industrial Robotic Manipulators with Elastic Members", ASME J. Mech. Trans. Autom. Des., Vol. 105, pp. 42-51, 1983.

[58] P. B. Usoro, R. Nadiren and S. S. Mahil, "A finite Element/Lagrange Approach to modeling Light Weight Flexible Manipulators," ASME J. Dyn. Syst. Control, Vol. 108, No. 3, pp. 198-203, 1986.

Appendix A

Kinetic Energy

In order to apply Lagrange's equation (2.1) to derive the RMS link dynamic equations, we need to determine the kinetic and potential energies of the system. The system kinetic energy consists of translational kinetic energy and rotational kinetic energy, i.e.

$$K_{total} = K_{rotational} + K_{translational}$$

A.1 Translational Kinetic Energy

First, we are going to derive the translational kinetic energy.

With (2.3.1) the translational kinetic energy of a point mass on link i can be described as

$$dk_i = \frac{1}{2}dmT_r\left\{{}^0\dot{h}_i{}^0\dot{h}_i{}^T\right\} = \frac{1}{2}dmT_r\left\{\dot{w}_i{}^ih_i{}^ih_i\dot{w}_i{}^T + 2\dot{w}_i{}^ih_i{}^i\dot{h}_i{}^T\dot{w}_i{}^T + w_i{}^i\dot{h}_i{}^i\dot{h}_i{}^Tw_i{}^T\right\}$$

(a.1.1)

104

In our case, with (2.3.2) and (2.3.3), for link i=2,3 we have

$$^i h_i = \left[x, \sum_{j=1}^{3} \phi_{ij}(x)\delta_{ij}(t), \sum_{4}^{6} \phi_{ij}(x)\delta_{ij}(t), 1 \right] \qquad (a.1.2)$$

$$^i \dot{h}_i = \left[0, \sum_{j=1}^{3} \phi_{ij}(x)\dot{\delta}_{ij}(t), \sum_{4}^{6} \phi_{ij}(x)\dot{\delta}_{ij}(t), 0 \right] \qquad (a.1.3)$$

$$K_{translational} = \sum_{i=1}^{n} \int_{0}^{l_i} dk_i = \sum_{i=1}^{n} T_r\{\dot{w}_i B_{3i} \dot{w}_i^T + 2\dot{w}_i B_{2i} w_i^T + w_i B_{1i} w_i^T\} \qquad (a.1.4)$$

where

$$B_{1i} = \frac{1}{2}\int_{0}^{l_i} \mu_i \, ^i\dot{h}_i \, ^i\dot{h}_i^T \, dx$$

$$= \frac{1}{2}\int_{0}^{l_i} \mu_i \begin{bmatrix} 0 \\ \sum\limits_{j=1}^{3} \phi_{ij}(x)\dot{\delta}_{ij}(t) \\ \sum\limits_{j=4}^{6} \phi_{ij}(x)\dot{\delta}_{ij}(t) \\ 0 \end{bmatrix} \begin{bmatrix} 0 & \sum\limits_{j=1}^{3} \phi_{ij}(x)\dot{\delta}_{ij}(t) & \sum\limits_{j=4}^{6} \phi_{ij}(x)\dot{\delta}_{ij}(t) & 0 \end{bmatrix} dx$$

$$= \frac{\mu_i}{2}\int_{0}^{l_i} \begin{bmatrix} 0 & 0 & 0 & 0 \\ 0 & \sum\limits_{j=1}^{3} \phi_{ij}\dot{\delta}_{ij} \sum\limits_{j=1}^{3} \phi_{ij}\dot{\delta}_{ij} & \sum\limits_{j=1}^{3} \phi_{ij}\dot{\delta}_{ij} \sum\limits_{j=4}^{6} \phi_{ij}\dot{\delta}_{ij} & 0 \\ 0 & \sum\limits_{j=4}^{6} \phi_{ij}\dot{\delta}_{ij} \sum\limits_{j=1}^{3} \phi_{ij}\dot{\delta}_{ij} & \sum\limits_{j=4}^{6} \phi_{ij}\dot{\delta}_{ij} \sum\limits_{j=4}^{6} \phi_{ij}\dot{\delta}_{ij} & 0 \\ 0 & 0 & 0 & 0 \end{bmatrix} dx \qquad (a.1.5)$$

using the orthogonality relation

105

$$\frac{1}{2}\int_0^{l_i}\phi_{ci}(x)\phi_{cj}(x)\mu_i\,dx = \frac{1}{2}\mu_i l_i^3 \zeta_{ij} \qquad\qquad \zeta_{ij} = \begin{cases} 1 & i = j \\ 0 & i \neq j \end{cases}$$

(a.1.6)

we re-write (a.1.5) as

$$B_{1i} = \begin{bmatrix} 0 & 0 & 0 & 0 \\ 0 & \displaystyle\sum_{j=1}^{3}\frac{1}{2}\mu_i l_i^3 \dot{\delta}_{ij}^2 & \frac{1}{2}\mu_i l_i^3(\dot{\delta}_{i1}\dot{\delta}_{i4} + \dot{\delta}_{i2}\dot{\delta}_{i5} + \dot{\delta}_{i3}\dot{\delta}_{i6}) & 0 \\ 0 & \frac{1}{2}\mu_i l_i^3(\dot{\delta}_{i4}\dot{\delta}_{i1} + \dot{\delta}_{i5}\dot{\delta}_{i2} + \dot{\delta}_{i6}\dot{\delta}_{i3}) & \displaystyle\sum_{j=4}^{6}\frac{1}{2}\mu_i l_i^3 \dot{\delta}_{ij}^2 & 0 \\ 0 & 0 & 0 & 0 \end{bmatrix}$$

(a.1.7)

In Book's notation

$$B_{1i} = \sum_{j=1}^{m_i}\sum_{k=1}^{m_i} \dot{\delta}_{ij}\dot{\delta}_{ik}C_{ikj}$$

(a.1.8)

where

$$C_{ikj} = \frac{1}{2}\int_0^{l_i}\mu_i\begin{bmatrix}0 & x_{ik} & y_{ik} & z_{ik}\end{bmatrix}^T\begin{bmatrix}0 & x_{ik} & y_{ik} & z_{ik}\end{bmatrix}dx$$

(a.1.9)

Let us define $FMI_i = \frac{1}{2}\mu_i l_i^3$; in our model, we have

$$C_{i11} = C_{i22} = C_{i33} = \begin{bmatrix} 0 & 0 & 0 & 0 \\ 0 & FMI_i & 0 & 0 \\ 0 & 0 & 0 & 0 \\ 0 & 0 & 0 & 0 \end{bmatrix} \qquad (a.1.10)$$

$$C_{i44} = C_{i55} = C_{i66} = \begin{bmatrix} 0 & 0 & 0 & 0 \\ 0 & 0 & 0 & 0 \\ 0 & 0 & FMI_i & 0 \\ 0 & 0 & 0 & 0 \end{bmatrix} \qquad (a.1.11)$$

$$C_{i14} = C_{i25} = C_{i36} = \begin{bmatrix} 0 & 0 & 0 & 0 \\ 0 & 0 & FMI_i & 0 \\ 0 & 0 & 0 & 0 \\ 0 & 0 & 0 & 0 \end{bmatrix} \qquad (a.1.12)$$

$$C_{i41} = C_{i52} = C_{i63} = \begin{bmatrix} 0 & 0 & 0 & 0 \\ 0 & 0 & 0 & 0 \\ 0 & FMI_i & 0 & 0 \\ 0 & 0 & 0 & 0 \end{bmatrix} \qquad (a.1.13)$$

In (a.1.4)

$$B_{2i} = \frac{1}{2}\int_0^{l_i} \mu_i \, {}^i h_i \, {}^i \dot{h}_i^{\,T} dx$$

$$= \frac{1}{2}\int_0^{l_i} \mu_i \begin{bmatrix} x \\ \sum_{j=1}^{3} \phi_{ij}(x)\delta_{ij}(t) \\ \sum_{j=4}^{6} \phi_{ij}(x)\delta_{ij}(t) \\ 1 \end{bmatrix} \begin{bmatrix} 0 & \sum_{j=1}^{3} \phi_{ij}(x)\dot{\delta}_{ij}(t) & \sum_{j=4}^{6} \phi_{ij}(x)\dot{\delta}_{ij}(t) & 0 \end{bmatrix} dx$$

$$= \frac{1}{2}\int_0^{l_i} \mu_i \begin{bmatrix} 0 & \displaystyle\sum_{j=1}^{3} x\phi_{ij}(x)\dot{\delta}_{ij}(t) & \displaystyle\sum_{j=4}^{6} x\phi_{ij}(x)\dot{\delta}_{ij}(t) & 0 \\[2em] 0 & \left(\displaystyle\sum_{j=1}^{3}\phi_{ij}(x)\delta_{ij}(t)\sum_{j=1}^{3}\phi_{ij}(x)\dot{\delta}_{ij}(t)\right) & \left(\displaystyle\sum_{j=1}^{3}\phi_{ij}(x)\delta_{ij}(t)\sum_{j=4}^{6}\phi_{ij}(x)\dot{\delta}_{ij}(t)\right) & 0 \\[2em] 0 & \left(\displaystyle\sum_{j=4}^{6}\phi_{ij}(x)\delta_{ij}(t)\sum_{j=1}^{3}\phi_{ij}(x)\dot{\delta}_{ij}(t)\right) & \left(\displaystyle\sum_{j=4}^{6}\phi_{ij}(x)\delta_{ij}(t)\sum_{j=4}^{6}\phi_{ij}(x)\dot{\delta}_{ij}(t)\right) & 0 \\[2em] 0 & \displaystyle\sum_{j=1}^{3}\phi_{ij}(x)\dot{\delta}_{ij}(t) & \displaystyle\sum_{j=4}^{6}\phi_{ij}(x)\dot{\delta}_{ij}(t) & 0 \end{bmatrix}$$

(a.1.14)

Next, we define

$$FI_{im} = \frac{1}{2}\int_0^{l_i}\mu_i\phi_{im}(x)dx \qquad m = 1...6$$

(a.1.15)

$$FI_{i1} = FI_{i4}, FI_{i2} = FI_{i5}, FI_{i3} = FI_{i6}$$

$$FXI_{im} = \frac{1}{2}\int_0^{l_i}\mu_i x\phi_{im}(x)dx \qquad m = 1...6$$

(a.1.16)

$$FXI_{i1} = FXI_{i4}, FXI_{i2} = FXI_{i5}, FXI_{i3} = FXI_{i6}$$

Using Book's notation, we can write

$$B_{2i} = \sum_{j=1}^{m_i}\dot{\delta}_{ij}C_{ij} + \sum_{k=1}^{m_i}\sum_{j=1}^{m_i}\delta_{ik}\dot{\delta}_{ij}C_{ikj}$$

(a.1.17)

and find

$$C_{i1} = \begin{bmatrix} 0 & FXI_{i1} & 0 & 0 \\ 0 & 0 & 0 & 0 \\ 0 & 0 & 0 & 0 \\ 0 & FI_{i1} & 0 & 0 \end{bmatrix} \quad C_{i2} = \begin{bmatrix} 0 & FXI_{i2} & 0 & 0 \\ 0 & 0 & 0 & 0 \\ 0 & 0 & 0 & 0 \\ 0 & FI_{i2} & 0 & 0 \end{bmatrix} \quad C_{i3} = \begin{bmatrix} 0 & FXI_{i3} & 0 & 0 \\ 0 & 0 & 0 & 0 \\ 0 & 0 & 0 & 0 \\ 0 & FI_{i3} & 0 & 0 \end{bmatrix}$$

$$C_{i4} = \begin{bmatrix} 0 & 0 & FXI_{i4} & 0 \\ 0 & 0 & 0 & 0 \\ 0 & 0 & 0 & 0 \\ 0 & 0 & FI_{i4} & 0 \end{bmatrix} \quad C_{i5} = \begin{bmatrix} 0 & 0 & FXI_{i5} & 0 \\ 0 & 0 & 0 & 0 \\ 0 & 0 & 0 & 0 \\ 0 & 0 & FI_{i5} & 0 \end{bmatrix} \quad C_{i6} = \begin{bmatrix} 0 & 0 & FXI_{i6} & 0 \\ 0 & 0 & 0 & 0 \\ 0 & 0 & 0 & 0 \\ 0 & 0 & FI_{i6} & 0 \end{bmatrix} \tag{a.1.18}$$

In (a.1.4)

$$B_{3i} = \tfrac{1}{2}\int_0^{l_i} \mu_i {}^i h_i {}^i h_i^T \, dx = \tfrac{1}{2}\int_0^{l_i} \mu_i \begin{bmatrix} x \\ \displaystyle\sum_{j=1}^{3} \phi_{ij}\delta_{ij} \\ \displaystyle\sum_{j=4}^{6} \phi_{ij}\delta_{ij} \\ 1 \end{bmatrix} \begin{bmatrix} x & \displaystyle\sum_{j=1}^{3} \phi_{ij}\delta_{ij} & \displaystyle\sum_{j=4}^{6} \phi_{ij}\delta_{ij} \end{bmatrix}$$

$$= \frac{\mu_i}{2}\int_0^{l_i} \begin{bmatrix} x^2 & \displaystyle\sum_{j=1}^{3} x\phi_{ij}\delta_{ij} & \displaystyle\sum_{j=4}^{6} x\phi_{ij}\delta_{ij} & x \\ \displaystyle\sum_{j=1}^{3} x\phi_{ij}\delta_{ij} & \displaystyle\sum_{j=1}^{3}\phi_{ij}\delta_{ij}\sum_{j=1}^{3}\phi_{ij}\delta_{ij} & \displaystyle\sum_{j=1}^{3}\phi_{ij}\delta_{ij}\sum_{j=4}^{6}\phi_{ij}\delta_{ij} & \displaystyle\sum_{j=1}^{3}\phi_{ij}\delta_{ij} \\ \displaystyle\sum_{j=4}^{6} x\phi_{ij}\delta_{ij} & \displaystyle\sum_{j=4}^{6}\phi_{ij}\delta_{ij}\sum_{j=1}^{3}\phi_{ij}\delta_{ij} & \displaystyle\sum_{j=4}^{6}\phi_{ij}\delta_{ij}\sum_{j=4}^{6}\phi_{ij}\delta_{ij} & \displaystyle\sum_{j=4}^{6}\phi_{ij}\delta_{ij} \\ x & \displaystyle\sum_{j=1}^{3}\phi_{ij}\delta_{ij} & \displaystyle\sum_{j=4}^{6}\phi_{ij}\delta_{ij} & 1 \end{bmatrix} \tag{a.1.19}$$

Using Book's notation, we can write (a.1.19) as

$$B_{3i} = C_i + \sum_{j=1}^{m_i} \delta_{ij}[C_{ij} + C_{ij}^T] + \sum_{k=1}^{m_i}\sum_{j=1}^{m_i} \delta_{ik}\delta_{ij}C_{ikj} \tag{a.1.20}$$

109

where for beam like links, i.e., the elastic links 2 and 3 of the RMS, we obtain

$$C_i = \frac{\mu_i}{2}\begin{bmatrix} \int_0^{l_i} x^2 dx & 0 & 0 & \int_0^{l_i} x dx \\ 0 & 0 & 0 & 0 \\ 0 & 0 & 0 & 0 \\ \int_0^{l_i} x dx & 0 & 0 & \int_0^{l_i} 1 dx \end{bmatrix} = \frac{\mu_i}{2}\begin{bmatrix} \frac{l_i^3}{3} & 0 & 0 & \frac{l_i^2}{2} \\ 0 & 0 & 0 & 0 \\ 0 & 0 & 0 & 0 \\ \frac{l_i^2}{2} & 0 & 0 & l_i \end{bmatrix} = \begin{bmatrix} \frac{m_{ai}l_i^2}{6} & 0 & 0 & \frac{m_{ai}l_i}{4} \\ 0 & 0 & 0 & 0 \\ 0 & 0 & 0 & 0 \\ \frac{m_{ai}l_i}{4} & 0 & 0 & \frac{m_{ai}}{2} \end{bmatrix} \qquad (a.1.21)$$

C_i is the generalized moment of inertia. Equation (a.1.21) is only valid for long elastic links such as links 2 and 3 of the RMS. For all other links which are assumed rigid, we have

$$B_{3i} = C_i = \frac{1}{2}\int_v \rho_i\, {}^i h_i\, {}^i h_i^T dv = \frac{1}{2}\int_v \rho_i \begin{bmatrix} x \\ y \\ z \\ 1 \end{bmatrix} \begin{bmatrix} x & y & z & 1 \end{bmatrix} dv = \frac{\rho_i}{2}\int_v \begin{bmatrix} x^2 & xy & xz & x \\ xy & y^2 & yz & y \\ xz & yz & z^2 & z \\ x & y & z & 1 \end{bmatrix} dv \qquad (a.1.22)$$

Since

$$I_{ixx} = \rho_i\int_v (y^2 + z^2)dv, \quad I_{iyy} = \rho_i\int_v (x^2 + z^2)dv, \quad I_{izz} = \rho_i\int_v (x^2 + y^2)dv \qquad (a.1.23)$$

from (a.1.22), we get
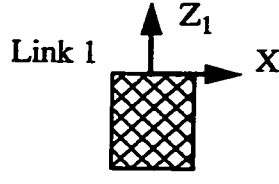
$$C_i = \frac{1}{2}\begin{bmatrix} \dfrac{-I_{ixx}+I_{iyy}+I_{izz}}{2} & I_{ixy} & I_{ixz} & m_{ai}\bar{x}_i \\[2mm] I_{ixy} & \dfrac{I_{ixx}-I_{iyy}+I_{izz}}{2} & I_{iyz} & m_{ai}\bar{y}_i \\[2mm] I_{ixz} & I_{iyz} & \dfrac{I_{ixx}+I_{iyy}-I_{izz}}{2} & m_{ai}\bar{z}_i \\[2mm] m_{ai}\bar{x}_i & m_{ai}\bar{y}_i & m_{ai}\bar{z}_i & m_{ai} \end{bmatrix} \qquad (a.1.24)$$

Next, we use the parallel axis theorem (a.1.25),
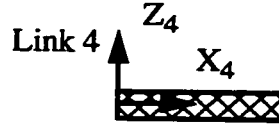
$$I_{ixx} = I_{ixxc} + m_{ai}P_{ci}^2 \qquad (a.1.25)$$

where m_{ai} is the mass of link i and P_{ci} is the distance from the center of mass to the coor-

dinate origin. This procedure is described as below:
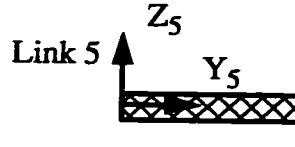
Link 1
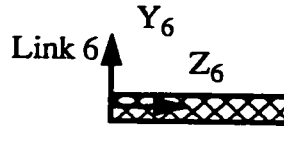
$$I_{1xx} = I_{1xxc} + m_{a1}P_{c1}^2, I_{1yy} = I_{1yyc} + m_{a1}P_{c1}^2, I_{1zz} = I_{1zzc}$$

(a.1.26)

Link 4

$$I_{4xx} = I_{4xxc}, I_{4yy} = I_{4yyc} + m_{a4}P_{c4}^2, I_{4zz} = I_{4zzc} + m_{a4}P_{c4}^2$$

(a.1.27)

Link 5

$$I_{5xx} = I_{5xxc} + m_{a5}P_{c5}^2, I_{5yy} = I_{5yyc}, I_{5zz} = I_{5zzc} + m_{a5}P_{c5}^2$$

(a.1.28)

Link 6

$$I_{6xx} = I_{6xxc} + m_{a6}P_{c6}^2, I_{6yy} = I_{6yyc} + m_{a6}P_{c6}^2, I_{6zz} = I_{6zzc}$$

(a.1.29)

Using the parallel axis theorem, we can convert $I_{ixxc}, I_{iyyc}, I_{izzc}$ which are given in RMS master data set [35] and are relative to the center of mass to the set we need where they would be relative to the "Frame origin".

A.2 Rotational Kinetic Energy

The rotational kinetic energy comes from the torsional deflection of the two elastic links. For links 2 and 3, define $\Omega_i(x)$ as angular displacement for a point on link i, which is equal to $\Theta_{xi}(x)$ in (2.2.3) as shown in Figure 2.3.

$$\Omega_i = w_i^{\,i}\Omega_i$$

$$dK_{rotational} = \frac{1}{2}\frac{I_{ixx}}{l_i}T_r\{\dot{\Omega}_i\dot{\Omega}_i^T\}dl \qquad (a.2.1)$$

where T_r denotes "trace" of a matrix.

$$\therefore dk_i = \frac{1}{2}\frac{I_{ixx}}{l_i}T_r\left\{\dot{w}_i{}^i\Omega_i{}^i\Omega_i^T\dot{w}_i^T + 2\dot{w}_i{}^i\Omega_i{}^i\dot{\Omega}_i^T w_i^T + w_i{}^i\dot{\Omega}_i{}^i\dot{\Omega}_i^T w_i^T\right\}dl \qquad (a.2.2)$$

where

$${}^i\Omega_i = \sum_{j=7}^{9}\left[\phi_{ij}(x)\ 0\ 0\ 0\right]^T\delta_{ij}(t) \qquad (a.2.3)$$

$${}^i\dot{\Omega}_i = \sum_{j=7}^{9}\left[\phi_{ij}(x)\ 0\ 0\ 0\right]^T\dot{\delta}_{ij}(t) \qquad (a.2.4)$$

We can find the total rotational kinetic energy of the system

$$K_{rotational} = \sum_{i=1}^{n}\int_0^{l_i}dk_i = \sum_{i=1}^{n}T_r\{\dot{w}_iB_{3i}{}'\dot{w}_i^T + 2\dot{w}_iB_{2i}{}'w_i^T + w_iB_{1i}{}'w_i^T\} \qquad (a.2.5)$$

where

$$B_{1i}{}' = \frac{I_{ixx}}{2l_i}\int_0^{l_i}{}^i\Omega_i{}^i\Omega_i^T dx = \frac{I_{ixx}}{2l_i}\int_0^{l_i}\begin{bmatrix} \sum_{j=7}^{9}\phi_{ij}^2(x)\delta_{ij}^2 & 0 & 0 & 0 \\ 0 & 0 & 0 & 0 \\ 0 & 0 & 0 & 0 \\ 0 & 0 & 0 & 0 \end{bmatrix}dx = C_{i77}\delta_{i7}^2 + C_{i88}\delta_{i8}^2 + C_{i99}\delta_{i9}^2$$

$$(a.2.6)$$

using the orthorgonality relation

$$\int_0^{l_i}\phi_{ij}(x)\phi_{ik}(x)dx = \begin{cases} 0 & j \neq k \\ \dfrac{l_i}{2} & j = k \end{cases},$$

we obtain

$$C_{i77} = C_{i88} = C_{i99} = \begin{bmatrix} \dfrac{I_{ixx}}{4} & 0 & 0 & 0 \\ 0 & 0 & 0 & 0 \\ 0 & 0 & 0 & 0 \\ 0 & 0 & 0 & 0 \end{bmatrix} \qquad (a.2.7)$$

In (a.2.5), we have

$$B_{2i}{}' = \frac{I_{ixx}}{2l_i} \int_0^{l_i} {}^i\Omega_i \, {}^i\dot{\Omega}_i^T dx = \frac{I_{ixx}}{2l_i} \int_0^{l_i} \begin{bmatrix} \displaystyle\sum_{j=7}^{9} \phi_{ij}\delta_{ij} \\ 0 \\ 0 \\ 0 \end{bmatrix} \begin{bmatrix} \displaystyle\sum_{j=7}^{9} \phi_{ij}\dot{\delta}_{ij} & 0 & 0 & 0 \end{bmatrix} dx$$

$$= \frac{I_{ixx}}{2l_i} \int_0^{l_i} \begin{bmatrix} \displaystyle\sum_{j=7}^{9} \phi_{ij}\delta_{ij}\dot{\delta}_{ij} & 0 & 0 & 0 \\ 0 & 0 & 0 & 0 \\ 0 & 0 & 0 & 0 \\ 0 & 0 & 0 & 0 \end{bmatrix} dx$$

$$= C_{i77}\delta_{i7}\dot{\delta}_{i7} + C_{i88}\delta_{i8}\dot{\delta}_{i8} + C_{i99}\delta_{i9}\dot{\delta}_{i9} \qquad (a.2.8)$$

It is easy to find $C_{ik} = 0$ for $k = 7, 8, 9$.

In (a.2.5), we also have

$$B_{3i}{}' = \frac{I_{ixx}}{2l_i} \int_0^{l_i} {}^i\Omega_i \, {}^i\Omega_i^T dx = \frac{I_{ixx}}{2l_i} \int_0^{l_i} \begin{bmatrix} \displaystyle\sum_{j=7}^{9} \phi_{ij}\delta_{ij} \\ 0 \\ 0 \\ 0 \end{bmatrix} \begin{bmatrix} \displaystyle\sum_{j=7}^{9} \phi_{ij}\delta_{ij} & 0 & 0 & 0 \end{bmatrix} dx$$

$$= \frac{I_{ixx}}{2l_i} \int_0^{l_i} \begin{bmatrix} \displaystyle\sum_{j=7}^{9} \phi_{ij}^2\delta_{ij}^2 & 0 & 0 & 0 \\ 0 & 0 & 0 & 0 \\ 0 & 0 & 0 & 0 \\ 0 & 0 & 0 & 0 \end{bmatrix} dx = C_{i77}\delta_{i7}^2 + C_{i88}\delta_{i8}^2 + C_{i99}\delta_{i9}^2 \qquad (a.2.9)$$

While recognizing the similar format of (a.2.5) and (a.1.4) which represents the translational kinetic energy, we can combine the equations together into one equation with

$$K_{total} = \sum_{i=1}^{n} T_r\{\dot{w}_i B_{3i} \dot{w}_i^T + 2\dot{w}_i B_{2i} w_i^T + w_i B_{1i} w_i^T\}$$

(a.2.10)

where

$$B_{1i} = \sum_{j=1}^{9} \sum_{k=1}^{9} \dot{\delta}_{ij}\dot{\delta}_{ik} C_{ikj}$$

(a.2.10)

$$B_{2i} = \sum_{j=1}^{9} \dot{\delta}_{ij} C_{ij} + \sum_{k=1}^{9} \sum_{j=1}^{9} \delta_{ik}\dot{\delta}_{ij} C_{ikj}$$

(a.2.11)

$$B_{3i} = C_i + \sum_{j=1}^{9} \delta_{ij}[C_{ij} + C_{ij}^T] + \sum_{k=1}^{9} \sum_{j=1}^{9} \delta_{ik}\delta_{ij} C_{ikj}$$

(a.2.12)

114

Appendix B

Potential Energy

The potential energy of the system comes from the beam deflection. It can be described as

$$dV_{ei} = \frac{1}{2}\left\{ E_{yi}\left[I_{iz}\left(\frac{\partial\theta_{zi}}{\partial x}\right)^2 + I_{iy}\left(\frac{\partial\theta_{yi}}{\partial x}\right)^2 \right] + G_{si}I_{ix}\left[\left(\frac{\partial\theta_{xi}}{\partial x}\right)\right]^2 \right\}dx \qquad (b.1)$$

where θ_{xi}, θ_{yi}, θ_{zi} are rotational components of the neutral axis at x about X, Y and Z axes.

In our case

$$\frac{\partial\theta_{zi}}{\partial x} = \sum_{j=1}^{3} \phi_{ij}''\delta_{ij}(t) \qquad \frac{\partial\theta_{yi}}{\partial x} = \sum_{j=4}^{6} \phi_{ij}''\delta_{ij}(t) \qquad \frac{\partial\theta_{xi}}{\partial x} = \sum_{j=7}^{9} \phi_{ij}'\delta_{ij}(t)$$

$$(b.2)$$

where I_{ix} denotes the polar area moment of inertia of the link's cross section about the neutral axis of link i; I_{iy} and I_{iz} denotes the area moment of inertia of the link's cross section about the Y_i and Z_i axes of link i respectively.

Let us define

$$K_{ij} = \int_0^{l_i} G_{si} I_{ix}(\phi_{ij}')^2 dx \qquad j = 7, 8, 9 \qquad \text{(b.3)}$$

$$K_{ij} = \int_0^{l_i} E_{yi} I_{iz}(\phi_{ij}'')^2 dx \qquad j = 1, 2, 3 \qquad \text{(b.4)}$$

$$K_{ij} = \int_0^{l_i} E_{yi} I_{iy}(\phi_{ij}'')^2 dx \qquad j = 4, 5, 6 \qquad \text{(b.5)}$$

$$V_e = \frac{1}{2} \sum_{i=2}^{3} \sum_{j=1}^{9} K_{ij} \delta_{ij}^2(t) \qquad \text{(b.6)}$$

Using the orthogonality relations

$$\frac{1}{2}\int_0^{l_i} E_{yi} I_{iy} \phi_{ij}''(x)\phi_{ik}''(x)dx = \mu_i l_i^3 \omega_{ij}^2 \zeta_{jk}$$

$$\frac{1}{2}\int_0^{l_i} E_{yi} I_{iz} \phi_{ij}''(x)\phi_{ik}''(x)dx = \mu_i l_i^3 \omega_{ij}^2 \zeta_{jk} \qquad \zeta_{jk} = \begin{cases} 1 & k = j \\ 0 & k \neq j \end{cases} \qquad \text{(b.7)}$$

we have

$$K_{ij} = \mu_i l_i^3 \omega_{ij}^2 = m_{ai} l_i^2 \omega_{ij}^2 \qquad j = 1, ..., 6 \qquad \text{(b.8)}$$

and using the orthogonality relation

$$\frac{1}{2}\int_0^{l} G_i I_{ix} \phi_{ij}'(x)\phi_{ik}'(x)dx = \frac{I_{ixx}}{2}\omega_{ij}^2 \zeta_{jk} \qquad \zeta_{jk} = \begin{cases} 1 & k = j \\ 0 & k \neq j \end{cases} \qquad \text{(b.9)}$$

we have

$$K_{ij} = \frac{I_{ixx}}{2}\omega_{ij}^2 \qquad j = 7, 8, 9 \qquad \text{(b.10)}$$

where I_{ixx} is the moment of inertia of link i. Therefore, we have

$$\frac{\partial V_e}{\partial \delta_{im}} = K_{im}\delta_{im} \qquad \text{(b.11)}$$

Appendix C

Dynamic Equations

Here, we use the Euler-Lagrange equation (2.1) to derive the RMS link dynamics. First, we recognize that

$$\frac{\partial \dot{w}_i}{\partial \dot{\theta}_j} = \frac{\partial w_i}{\partial \theta_j} \qquad \frac{d}{dt}\left(\frac{\partial \dot{w}_i}{\partial \dot{\theta}_j}\right) = \frac{\partial \dot{w}_i}{\partial \theta_j} \qquad\qquad (c.1)$$

and

$$\frac{\partial \dot{w}_i}{\partial \dot{\delta}_{jf}} = \frac{\partial w_i}{\partial \delta_{jf}} \qquad \frac{d}{dt}\left(\frac{\partial \dot{w}_i}{\partial \dot{\delta}_{jf}}\right) = \frac{\partial \dot{w}_i}{\partial \delta_{jf}} \qquad\qquad (c.2)$$

In order to find $\frac{d}{dt}\left(\frac{\partial K_{total}}{\partial \dot{\theta}_j}\right) - \frac{\partial K_{total}}{\partial \theta_j}$ in (2.1), from (a.2.10) we calculate

$$\frac{\partial K_{total}}{\partial \theta_j} = \sum_{i=j}^{n} T_r \left\{ 2\frac{\partial \dot{w}_i}{\partial \theta_j}B_{3i}\dot{w}_i^T + 2\frac{\partial \dot{w}_i}{\partial \theta_j}B_{2i}w_i^T + 2\dot{w}_i B_{2i}\frac{\partial w_i^T}{\partial \theta_j} + 2\frac{\partial w_i}{\partial \theta_j}B_{1i}w_i^T \right\} \quad (c.3)$$

and

$$\frac{\partial K_{total}}{\partial \dot{\theta}_j} = \sum_{i=j}^{n} T_r \left\{ 2\frac{\partial \dot{w}_i}{\partial \dot{\theta}_j}B_{3i}\dot{w}_i^T + 2\frac{\partial \dot{w}_i}{\partial \dot{\theta}_j}B_{2i}w_i^T \right\} \qquad\qquad (c.4)$$

This gives

117

$$\frac{d}{dt}\left(\frac{\partial K_{total}}{\partial \dot{\theta}_j}\right) = \sum_{i=j}^{n} Tr\left\{2\frac{\partial \dot{w}_i}{\partial \theta_j}B_{3i}\dot{w}_i^{\ T} + 2\frac{\partial \dot{w}_i}{\partial \dot{\theta}_j}B_{3i}w_i^T + 2\frac{\partial w_i}{\partial \theta_j}\dot{B}_{3i}\dot{w}_i^{\ T}\right.$$

$$\left. + 2\frac{\partial \dot{w}_i}{\partial \theta_j}B_{2i}w_i^T + 2\frac{\partial w_i}{\partial \theta_j}\dot{B}_{2i}w_i^T + 2\frac{\partial w_i}{\partial \theta_j}B_{2i}\dot{w}_i^{\ T}\right\} \tag{c.5}$$

Then (c.3) and (c.5) give

$$\frac{d}{dt}\left(\frac{\partial K_{total}}{\partial \dot{\theta}_j}\right) - \frac{\partial K_{total}}{\partial \theta_j} = \sum_{i=j}^{n} Tr\left\{2\frac{\partial w_i}{\partial \theta_j}(B_{3i}\ddot{w}_i^{\ T} + (\dot{B}_{3i} + B_{2i} - B_{2i}^T)\dot{w}_i^{\ T} + \dot{B}_{2i}w_i^T)\right\} \tag{c.6}$$

where

$$B_{3i} = C_i + \sum_{j=1}^{m_i}\delta_{ij}[C_{ij} + C_{ij}^T] + \sum_{k=1}^{m_i}\sum_{j=1}^{m_i}\delta_{ik}\delta_{ij}C_{ikj} \tag{c.7}$$

$$\dot{B}_{3i} = \sum_{j=1}^{m_i}\dot{\delta}_{ij}[C_{ij} + C_{ij}^T] + \sum_{k=1}^{m_i}\sum_{j=1}^{m_i}\delta_{ik}\dot{\delta}_{ij}C_{ikj} + \sum_{k=1}^{m_i}\sum_{j=1}^{m_i}\dot{\delta}_{ik}\delta_{ij}C_{ikj} \tag{c.8}$$

and

$$\dot{B}_{2i} - B_{1i} = \sum_{j=1}^{m_i}\ddot{\delta}_{ij}C_{ij} + \sum_{k=1}^{m_i}\sum_{j=1}^{m_i}\dot{\delta}_{ik}\dot{\delta}_{ij}C_{ikj} + \sum_{k=1}^{m_i}\sum_{j=1}^{m_i}\delta_{ik}\ddot{\delta}_{ij}C_{ikj} - \sum_{j=1}^{m_i}\sum_{k=1}^{m_i}\dot{\delta}_{ij}\dot{\delta}_{ik}C_{ikj}$$

$$= \sum_{j=1}^{m_i}\ddot{\delta}_{ij}\left(C_{ij} + \sum_{k=1}^{m_i}\delta_{ik}C_{ikj}\right) \tag{c.9}$$

Therefore, (c.6) becomes

$$\frac{d}{dt}\left(\frac{\partial K_{total}}{\partial \dot{\theta}_j}\right) - \frac{\partial K_{total}}{\partial \theta_j} = \sum_{i=j}^{n} 2Tr\left\{\frac{\partial w_i}{\partial \theta_j}\left[\left[C_i + \sum_{j=1}^{m_i}\delta_{ij}\left(C_{ij} + C_{ij}^T + \sum_{k=1}^{m_i}\delta_{ik}C_{ikj}\right)\right]\ddot{w}_i^{\ T} + \right.\right.$$

$$\left.\left.\left[\sum_{j=1}^{m_i}\ddot{\delta}_{ij}\left(C_{ij} + \sum_{k=1}^{m_i}\delta_{ik}C_{ikj}\right)\right]w_i^T + \left[2\sum_{j=1}^{m_i}\dot{\delta}_{ij}\left(C_{ij} + \sum_{k=1}^{m_i}\delta_{ik}C_{ikj}\right)\right]\dot{w}_i^{\ T}\right]\right\}$$

$$= \sum_{i=j}^{n} 2T_r \left\{ \frac{\partial w_i}{\partial \theta_j} \left[G_i \ddot{w}_i^T + \sum_{k=1}^{m_i} \ddot{\delta}_{ik} D_{ik} w_i^T + 2 \sum_{k=1}^{m_i} \dot{\delta}_{ik} D_{ik} \dot{w}_i^T \right] \right\} \qquad \text{(c.10)}$$

Here we define

$$D_{ij} = C_{ij} + \sum_{k=1}^{m_i} \delta_{ik} C_{ikj} \qquad \text{(c.11)}$$

and

$$G_i = C_i + \sum_{j=1}^{m_i} \delta_{ij} \left(C_{ij} + C_{ij}^T + \sum_{k=1}^{m_i} \delta_{ik} C_{ikj} \right) \qquad \text{(c.12)}$$

Note that

1) w_i $(i = j + 1 \ldots)$ are functions of δ_{jf}, but not for $i \leq j$;

2) B_{2j}, B_{3j} are functions of δ_{jf}, not for B_{1j};

3) B_{3j} are not functions of $\dot{\delta}_{jf}$;

4) w_i are not functions of $\dot{\delta}_{jf}$;

On the other hand, in order to find $\dfrac{d}{dt}\left(\dfrac{\partial K_{toatl}}{\partial \dot{\delta}_{jf}} \right) - \dfrac{\partial K_{total}}{\partial \delta_{jf}}$ in (2.1), we calculate

$$\frac{\partial K_{total}}{\partial \dot{\delta}_{jf}} = \sum_{i=1}^{n} T_r \left\{ 2 \frac{\partial \dot{w}_i}{\partial \dot{\delta}_{jf}} B_{3i} \dot{w}_i^T + \dot{w}_i \frac{\partial B_{3i}}{\partial \dot{\delta}_{jf}} \dot{w}_i^T + 2 \frac{\partial \dot{w}_i}{\partial \dot{\delta}_{jf}} B_{2i} w_i^T + 2 \dot{w}_i \frac{\partial B_{2i}}{\partial \dot{\delta}_{jf}} w_i^T + \right.$$
$$\left. 2 \dot{w}_i B_{2i} \frac{\partial w_i^T}{\partial \dot{\delta}_{jf}} + 2 \frac{\partial w_i}{\partial \dot{\delta}_{jf}} B_{1i} w_i^T + w_i \frac{\partial B_{1i}}{\partial \dot{\delta}_{jf}} w_i^T \right\} \qquad \text{(c.13)}$$

and

$$\frac{\partial K_{total}}{\partial \dot{\delta}_{jf}} = \sum_{i=1}^{n} T_r \left\{ 2\frac{\partial \dot{w}_i}{\partial \dot{\delta}_{jf}} B_{3i} \dot{w}_i^T + \dot{w}_i \frac{\partial B_{3i}}{\partial \dot{\delta}_{jf}} \dot{w}_i^T + 2\frac{\partial \dot{w}_i}{\partial \dot{\delta}_{jf}} B_{2i} w_i^T \right.$$

$$\left. + 2\dot{w}_i \frac{\partial B_{2i}}{\partial \dot{\delta}_{jf}} w_i^T + 2\dot{w}_i B_{2i} \frac{\partial w_i^T}{\partial \dot{\delta}_{jf}} + 2\frac{\partial w_i^T}{\partial \dot{\delta}_{jf}} B_{1i} w_i^T + w_i \frac{\partial B_{1i}}{\partial \dot{\delta}_{jf}} w_i^T \right\}$$

therefore

$$\frac{d}{dt}\left(\frac{\partial K_{total}}{\partial \dot{\delta}_{jf}}\right) = \sum_{i=1}^{n} T_r \left\{ 2\frac{\partial \dot{w}_i}{\partial \delta_{jf}} \dot{B}_{3i} \dot{w}_i^T + 2\frac{\partial w_i}{\partial \delta_{jf}} \dot{B}_{3i} \dot{w}_i^T + 2\frac{\partial w_i}{\partial \delta_{jf}} B_{3i} \ddot{w}_i^T + 2\frac{\partial \dot{w}_i}{\partial \delta_{jf}} B_{2i} w_i^T \right.$$

$$+ 2\frac{\partial w_i}{\partial \delta_{jf}} \dot{B}_{2i} w_i^T + 2\frac{\partial w_i}{\partial \delta_{jf}} B_{2i} \dot{w}_i^T + 2\ddot{w}_i \frac{\partial B_{2i}}{\partial \dot{\delta}_{jf}} w_i^T + 2\dot{w}_i \frac{d\left(\frac{\partial B_{2i}}{\partial \dot{\delta}_{jf}}\right)}{dt} w_i^T + 2\dot{w}_i \frac{\partial B_{2i}}{\partial \dot{\delta}_{jf}} \dot{w}_i^T$$

$$\left. + 2\dot{w}_i \frac{\partial B_{1i}}{\partial \dot{\delta}_{jf}} w_i^T + w_i \frac{d\left(\frac{\partial B_{1i}}{\partial \dot{\delta}_{jf}}\right)}{dt} w_i^T \right\} \qquad (c.14)$$

$$\frac{d}{dt}\left(\frac{\partial K_{total}}{\partial \dot{\delta}_{jf}}\right) - \frac{\partial K_{total}}{\partial \delta_{jf}} =$$

$$\sum_{i=j+1}^{n} T_r \left\{ 2\frac{\partial w_i}{\partial \delta_{jf}} [\dot{B}_{3i} \dot{w}_i^T + B_{3i} \ddot{w}_i^T + \dot{B}_{2i} w_i^T + B_{2i} \dot{w}_i^T - B_{2i}^T \dot{w}_i^T - B_{1i} w_i^T] \right\}$$

$$+ T_r \left\{ \left[\begin{array}{c} 2\ddot{w}_j \frac{\partial B_{2j}}{\partial \dot{\delta}_{jf}} + 2\dot{w}_j \frac{d\left(\frac{\partial B_{2j}}{\partial \dot{\delta}_{jf}}\right)}{dt} + 2\dot{w}_j \frac{\partial B_{1j}}{\partial \dot{\delta}_{jf}} + w_i \frac{d\left(\frac{\partial B_{1j}}{\partial \dot{\delta}_{jf}}\right)}{dt} - 2\dot{w}_j \frac{\partial B_{2j}}{\partial \delta_{jf}} \end{array} \right] w_i^T \right.$$

$$\left. + 2\dot{w}_j \frac{\partial B_{2j}}{\partial \dot{\delta}_{jf}} \dot{w}_j^T - \dot{w}_j \frac{\partial B_{3j}}{\partial \delta_{jf}} \dot{w}_j^T \right\} \qquad (c.15)$$

Here, with (a.1.17) and (a.1.20), we have

$$B_{3i} + B_{2i} - B_{2i}^T = 2 \sum_{k=1}^{m_i} \dot{\delta}_{ik} D_{ik} \qquad (c.16)$$

$$\dot{B}_{2i} - B_{1i} = \sum_{j=1}^{m_i} \ddot{\delta}_{ij} C_{ij} + \sum_{k}^{m_i}\sum_{j}^{m_i} \dot{\delta}_{ik}\dot{\delta}_{ij} C_{ikj} + \sum_{k}^{m_i}\sum_{j}^{m_i} \delta_{ik}\ddot{\delta}_{ij} C_{ikj} - \sum_{k}^{m_i}\sum_{j}^{m_i} \ddot{\delta}_{ij}\dot{\delta}_{ik} C_{ikj}$$

$$= \sum_{j=1}^{m_i} \ddot{\delta}_{ij}\left(C_{ij} + \sum_{k=1}^{m_i} \delta_{ik} C_{ikj}\right) = \sum_{j=1}^{m_i} \ddot{\delta}_{ij} D_{ij} \qquad (c.17)$$

$$\frac{2d\left(\dfrac{\partial B_{2j}}{\partial \dot{\delta}_{jf}}\right)}{dt} + 2\frac{\partial B_{1j}}{\partial \dot{\delta}_{jf}} - 2\frac{\partial B_{2j}}{\partial \dot{\delta}_{jf}} =$$

$$2\frac{d\left(C_{jf} + \sum\limits_{k=1}^{m_i} \delta_{jk} C_{ikf}\right)}{dt} + 2\sum_{k=1}^{m_i} \dot{\delta}_{jk} C_{ikf} + 2\sum_{l=1}^{m_i} \delta_{jl} C_{ifl} - 2\sum_{l=1}^{m_i} \delta_{il} C_{ifl}$$

$$= 4\sum_{k=1}^{m_i} \dot{\delta}_{jk} C_{jkf} \qquad (c.18)$$

$$2\frac{\partial B_{2j}}{\partial \dot{\delta}_{jf}} - \frac{\partial B_{3j}}{\partial \delta_{jf}} = 2\left(C_{jf} + \sum_{k=1}^{m_i} \delta_{jk} C_{ikf}\right) - \left(C_{jf} + C_{jf}^T + \sum_{k=1}^{m_i} \delta_{if} C_{ikf} + \sum_{k=1}^{m_i} \delta_{if} C_{ifk}\right)$$

$$= C_{if} - C_{jf}^T + \sum_{k=1}^{m_i} \delta_{jk}(C_{jkf} - C_{jfk}) \qquad (c.19)$$

We can rewrite (c.15) as

$$\frac{d}{dt}\left(\frac{\partial K_{total}}{\partial \dot{\delta}_{jf}}\right) - \frac{\partial K_{total}}{\partial \delta_{jf}} = 2\sum_{i=j+1}^{n} T_r\left\{\frac{\partial w_i}{\partial \delta_{jf}}\left[G_i\ddot{w}_i^T + \sum_{k=1}^{m_i}\ddot{\delta}_{ik}D_{ik}w_i^T + 2\sum_{k=1}^{m_i}\dot{\delta}_{ik}D_{ik}\dot{w}_i^T\right]\right\}$$

$$+ T_r\left\{2\left[\ddot{w}_j D_{jf} + 2\dot{w}_j\sum_{k=1}^{m_i}\dot{\delta}_{jk}C_{jkf} + w_j\sum_{k=1}^{m_i}\ddot{\delta}_{jk}C_{jkf}\right]w_j^T\right\} \tag{c.20}$$

Using Book's notation:

$${}^{i}\hat{w}_j = A_{i+1}E_{i+1}...A_jE_j \qquad\qquad j\geq i+1 \tag{c.21}$$

$${}^{0}\hat{w}_i = \hat{w}_i = A_1E_1A_2E_2...A_iE_i \tag{c.22}$$

$${}^{i}w_j = A_{i+1}E_{i+1}...A_{j-1}E_{j-1}A_j \qquad j\geq i+1 \tag{c.23}$$

$${}^{0}w_i = A_1E_1...A_{i-1}E_{i-1}A_i \tag{c.24}$$

$${}^{i}\overline{w}_j = E_iA_{i+1}E_{i+1}...A_jE_j \qquad\qquad j\geq i+1; i\geq 1 \tag{c.25}$$

$${}^{1}\overline{w}_i = E_1A_2E_2...A_iE_i \tag{c.26}$$

$${}^{i}\tilde{w}_j = E_iA_{i+1}E_{i+1}...A_{j-1}E_{j-1}A_j \qquad j\geq i+1; i\geq 1 \tag{c.27}$$

$${}^{1}\tilde{w}_i = E_1A_2E_2...A_{i-1}E_{i-1}A_i \tag{c.28}$$

We also note that:

$$w_j = w_{j-1}E_{j-1}A_j = \hat{w}_{j-1}A_j \Rightarrow \dot{w}_j = \dot{\hat{w}}_{j-1}A_j + \hat{w}_{j-1}\dot{A}_j \Rightarrow$$

$$\ddot{w}_j = \ddot{\hat{w}}_{j-1}A_j + 2\dot{\hat{w}}_{j-1}\dot{A}_j + w_{j-1}\ddot{A}_j \tag{c.29}$$

$$\hat{w}_j = w_jE_j \Rightarrow \dot{\hat{w}}_j = \dot{w}_jE_j + w_j\dot{E}_j \Rightarrow \ddot{\hat{w}}_j = \ddot{w}_jE_j + 2\dot{w}_j\dot{E}_j + w_j\ddot{E}_j \tag{c.30}$$

Alternatively, we can write

$$\hat{w}_i = A_1 E_1 A_2 E_2 \ldots A_h E_h \ldots A_i E_i = \hat{w}_{h-1} A_h{}^h \bar{w}_i = w_h E_h{}^h \hat{w}_i \qquad \text{(c.31)}$$

$$\ddot{\hat{w}}_i = \sum_{h=1}^{i} \left(\hat{w}_{h-1} \mu_h{}^h \bar{w}_i \ddot{\theta}_h + \sum_{k=1}^{m_h} w_h M_{hk}{}^h \hat{w}_i \ddot{\delta}_{hk} \right) + \ddot{\hat{w}}_{vi} \qquad \text{(c.32)}$$

$$w_i = A_1 E_1 A_2 E_2 \ldots A_h E_h \ldots E_{i-1} A_i = \hat{w}_{h-1} A_h{}^h \bar{w}_i = w_h E_h{}^h w_i \qquad \text{(c.33)}$$

$$\ddot{w}_i = \sum_{h=1}^{i} \hat{w}_{h-1} \mu_h{}^h \bar{w}_i \ddot{\theta}_h \sum_{h=1}^{i-1} \sum_{k=1}^{m_i} w_h M_{hk}{}^h w_i \ddot{\delta}_{hk} + \ddot{w}_{vi} \qquad \text{(c.34)}$$

From (c.29) and (c.30), $\ddot{\hat{w}}_{vi}$ and $\ddot{w}_{vi}$ can be calculated recursively as

$$\ddot{w}_{vj} = \ddot{\hat{w}}_{v,j-1} A_j + 2\dot{\hat{w}} \dot{A}_j + \hat{w}_{j-1} U_{2j} \dot{\theta}_j^2 \qquad \text{(c.35)}$$

$$\ddot{\hat{w}}_{vj} = \ddot{w}_{vj} E_j + 2\dot{w}_j \dot{E}_j \qquad \text{(c.36)}$$

where

$$U_{2j} = \frac{\partial^2 A_j}{\partial \theta_j^2}$$

With the "camped-free" mode assumption $\phi'(0) = 0$, the generalized force for deflection variables will be zero. Considering equation (2.1) where $L = K_{total} - V_e$. If we separate (2.1) into two groups according to the type of coordinates on which the differentiation is applied, we can have one group of equations where the differentiation is applied on rigid coordinates and the other group of equations where the differentiation is applied on elastic coordinates.

Joint Equation "j"

Where the differentiation is applied on rigid coordinates θ_j, RMS is a six joint robot, we have $j = 1 \ldots 6$

$$\frac{d}{dt}\left(\frac{\partial K_{total}}{\partial \dot{\theta}_j}\right) - \frac{\partial K_{total}}{\partial \theta_j} + \frac{\partial V_e}{\partial \theta_j} = F_j \qquad \text{(c.37)}$$

Deflection Equations "jf"

$$\frac{d}{dt}\left(\frac{\partial K_{total}}{\partial \dot{\delta}_{jf}}\right) - \frac{\partial K_{total}}{\partial \delta_{jf}} + \frac{\partial V_e}{\partial \delta_{jf}} = 0 \qquad \text{(c.38)}$$

We can re-write (c.37) and (c.38) by collecting all the $\ddot{\theta}, \ddot{\delta}$ terms so that (c.37) becomes

$$\sum_{h=1}^{6} J_{jh}\ddot{\theta}_h + \sum_{l=1}^{9} J_{j2l}\ddot{\delta}_{2l} + \sum_{l=1}^{9} J_{j3l}\ddot{\delta}_{3l} = R_j \qquad j = 1 \ldots 6$$

$$\text{(c.39)}$$

and (c.38) becomes

$$\sum_{h=1}^{6} J_{2fh}\ddot{\theta}_h + \sum_{l=1}^{9} J_{2f2l}\ddot{\delta}_{2l} + \sum_{l=1}^{9} J_{2f3l}\ddot{\delta}_{3l} = R_{2f} \qquad f = 1 \ldots 9$$

$$\sum_{h=1}^{6} J_{3fh}\ddot{\theta}_h + \sum_{l=1}^{9} J_{3f2l}\ddot{\delta}_{2l} + \sum_{l=1}^{9} J_{3f3l}\ddot{\delta}_{3l} = R_{3f} \qquad f = 1 \ldots 9$$

$$\text{(c.40)}$$

We write the complete dynamics equations in the form

$$J\ddot{z} = R \qquad \text{(c.41)}$$

where z is the vector of the generalized coordinates

$$z = [\theta_1, \theta_2, \theta_3, \theta_4, \theta_5, \theta_6, \delta_{21}, \delta_{22}, \ldots, \delta_{29}, \delta_{31}, \delta_{32}, \ldots, \delta_{39}]^T$$

The term R is of the form $R = [R_1, R_2, R_3, R_4, R_5, R_6, R_{21}, R_{22}, \ldots, R_{29}, R_{31}, \ldots, R_{39}]^T$

124

which contains the remaining dynamics. The inertial matrix J is of the form

$$
J = \begin{bmatrix}
\begin{bmatrix} J_{11} & J_{12} & \cdots & J_{16} \\ J_{21} & J_{22} & & \\ \vdots & & & \\ J_{61} & & & J_{66} \end{bmatrix} &
\begin{bmatrix} J_{121} & J_{122} & \cdots & J_{129} \\ J_{221} & & & \\ \vdots & & & \\ J_{621} & & & J_{629} \end{bmatrix} &
\begin{bmatrix} J_{131} & J_{132} & \cdots & J_{139} \\ J_{231} & & & \\ \vdots & & & \\ J_{631} & & & J_{639} \end{bmatrix} \\
\begin{bmatrix} J_{211} & J_{212} & \cdots & J_{216} \\ J_{221} & & & \\ \vdots & & & \\ J_{291} & & & J_{296} \end{bmatrix} &
\begin{bmatrix} J_{2121} & J_{2122} & \cdots & J_{2129} \\ J_{2221} & & & \\ \vdots & & & \\ J_{2921} & & & J_{2929} \end{bmatrix} &
\begin{bmatrix} J_{2131} & J_{2132} & \cdots & J_{2139} \\ J_{2231} & & & \\ \vdots & & & \\ J_{2931} & & & J_{2939} \end{bmatrix} \\
\begin{bmatrix} J_{311} & J_{312} & \cdots & J_{316} \\ J_{321} & & & \\ \vdots & & & \\ J_{391} & & & J_{396} \end{bmatrix} &
\begin{bmatrix} J_{3121} & J_{3122} & \cdots & J_{3129} \\ J_{3221} & & & \\ \vdots & & & \\ J_{3921} & & & J_{3929} \end{bmatrix} &
\begin{bmatrix} J_{3131} & J_{3132} & \cdots & J_{3139} \\ J_{3231} & & & \\ \vdots & & & \\ J_{3931} & & & J_{3939} \end{bmatrix}
\end{bmatrix}
\tag{c.42}
$$

Inertia coefficients of joint variables in the joint equations

Note that all occurrences of $\ddot{\theta}_j$ in (c.10) are in the expression for $\ddot{w}_i^T$

i.e., in the term with $\ddot{w}_i$ which is $2 \sum_{i=j}^{n} T_r \left\{ \dfrac{\partial w_i}{\partial \theta_j} G_i \ddot{w}_i^T \right\}$. Using (c.33) and (c.34), this term becomes

$$
2 \sum_{i=j}^{n} T_r \left\{ \hat{w}_{j-1} \frac{\partial A_{jj}}{\partial \theta_j} \tilde{w}_i G_i \left(\sum_{h=1}^{i} \hat{w}_{h-1} U_h{}^h \tilde{w}_i \ddot{\theta}_h \right)^T \right\}
\tag{c.43}
$$

where $\quad U_j = \dfrac{\partial A_j}{\partial \theta_j}$

Since

$$\sum_{i=j}^{n} \sum_{h=1}^{i} = \sum_{h=1}^{n} \sum_{i=max(h,\,j)}^{n} \tag{c.44}$$

(c.43) becomes

$$\sum_{h=1}^{n} \left(2T_r \left\{ \hat{w}_{j-1} \mu_j \left[\sum_{i=max(h,\,j)}^{n} ({}^j\tilde{w}_i G_i {}^h\tilde{w}_i^T) \right] U_h^T \hat{w}_{h-1}^T \ddot{\theta}_h \right\} \right) \tag{c.45}$$

The coefficients of $\ddot{\theta}_h$ in equation "j" are

$$J_{jh} = 2T_r \{ \hat{w}_{j-1} U_j {}^j\tilde{F}_h U_h^T \hat{w}_{h-1}^T \} \tag{c.46}$$

where

$${}^j\tilde{F}_h = \sum_{i=max(h,\,j)}^{n} ({}^j\tilde{w}_i G_i {}^h\tilde{w}_i^T) \tag{c.47}$$

Inertial coefficients of the deflection variables in the joint equations

The defection variables appear both in the expression for $\ddot{w}_i^T$ and explicitly in (c.20)
Notice that

$$\sum_{i=j}^{n} \sum_{h=1}^{i-1} = \sum_{h=1}^{n-1} \sum_{i=max(h+1,\,j)}^{n} \tag{c.48}$$

For equation "j", the terms contain $\ddot{\delta}$ are:

$$2 \sum_{i=j}^{n} T_r \left\{ \frac{\partial w_i}{\partial \theta_j} \left[G_i \ddot{w}_i^T + \sum_{l=1}^{m} \ddot{\delta}_{il} D_{il} w_i^T \right] \right\} \tag{c.49}$$

which can be written as

.

126

$$2 \sum_{i=j}^{n} T_r \left\{ \frac{\partial w_i}{\partial \theta_j} \left[G_i \left(\sum_{h=1}^{i-1} \sum_{l=1}^{m_i} w_h M_{hl}{}^h w_i \ddot{\delta}_{hl} \right)^T + \sum_{l=1}^{m_i} \ddot{\delta}_{il} D_{il} w_i^T \right] \right\}$$

$$= 2 \sum_{h=1}^{n-1} \sum_{i=max(h+1,j)}^{n} T_r \left\{ \frac{\partial w_i}{\partial \theta_j} G_i \left(\sum_{l=1}^{m_i} w_h M_{hl}{}^h w_i \ddot{\delta}_{hl} \right)^T \right\} + 2 \sum_{i=j}^{n} T_r \left\{ \frac{\partial w_i}{\partial \theta_j} \left(\sum_{l=1}^{m_i} \ddot{\delta}_{il} D_{il} w_i^T \right) \right\}$$

$$= 2 \sum_{h=1}^{n-1} \sum_{i=max(h+1,j)}^{n} T_r \left\{ \frac{\partial w_i}{\partial \theta_j} G_i \left(\sum_{l=1}^{m_i} w_h M_{hl}{}^h w_i \ddot{\delta}_{hl} \right)^T \right\} + 2 \sum_{h=j}^{n} T_r \left\{ \frac{\partial w_h}{\partial \theta_j} \left(\sum_{l=1}^{m_i} \ddot{\delta}_{hl} D_{hl} w_h^T \right) \right\}$$

$$(c.50)$$

Note that

1. $h = n, j = 1 \dots n$

$$J_{jhl} = 2 T_r \left\{ \frac{\partial w_h}{\partial \theta_j} D_{hl} w_h^T \right\} = 2 T_r \{ \hat{w}_{j-1} \mu_j{}^j \tilde{w}_h D_{hl} w_h^T \} \qquad (c.51)$$

2. $h = j \dots n-1, j = 1 \dots n-1$

$$J_{jhl} = 2 \sum_{i=max(h+1,j)}^{n} \left\{ \frac{\partial w_i}{\partial \theta_j} G_i \left(\sum_{l=1}^{m_i} w_h M_{hk}{}^h w_i \ddot{\delta}_{hl} \right) \right\} + 2 T_r \left\{ \frac{\partial w_h}{\partial \theta_j} \left(\sum_{l=1}^{m_i} \ddot{\delta}_{hl} D_{hl} w_h^T \right) \right\}$$

$$= 2 T_r \left\{ \sum_{i=max(h+1,j)}^{n} \hat{w}_{j-1} U_j{}^j \tilde{w}_i G_i{}^h w_i^T M_{hl}^T w_h^T + \hat{w}_{j-1} U_j{}^j \tilde{w}_h D_{hl} w_h^T \right\}$$

$$= 2 T_r \{ \hat{w}_{j-1} U_j ({}^j F_h M_{hl}^T + {}^j \tilde{w}_h D_{hl}) w_h^T \} \qquad (c.52)$$

127

where

$$^jF_n = \sum_{i=max(h+1,\,j)}^{n} (^j\tilde{w}_i G_i{}^h w_i{}^T)$$

(c.53)

3. $h = 1...j-1, \; j = 2...n$

$$J_{jhl} = 2 \sum_{i=max(h+1,\,j)}^{n} T_r\left\{\frac{\partial w_i}{\partial \theta_j}G_i(w_h M_{hl}{}^h w_i \ddot{\delta}_{hl})^T\right\} = 2T_r\{\hat{w}_{j-1}U_j[^jF_h M_{hl}^T w_h^T]\}$$

(c.54)

Note: The inertia coefficients for joint variables $\ddot{\theta}_j$ in the deflection equation "hl" are the same as the inertia coefficients for $\ddot{\delta}_{hl}$ in the joint equation j due to the symmetry property of inertial matrix J, i.e., $J_{jhl} = J_{hlj}$.

Inertia coefficients of the deflection variables in the deflection equations

Noting that

$$T_r\{ABC\} = T_r\{CAB\} = T_r\{BCA\}$$

(c.55)

we have:

1) $j = h = n$

Only $\ddot{w}_i$ has contribution of $\ddot{\delta}_{hk}$ $(h = 1...i-1)$. Therefore, the coefficient

$$J_{nfnk} = 2T_r\{w_n C_{nkf} w_n^T\} = 2T_r\{C_{nfk} w_n^T w_n\} = 2T_r\{C_{nkf}\}$$

(c.56)

2) $j = h = 1...n-1$ terms with $\ddot{\delta}$ in the deflection equation for equation "jf" are of the form

128

$$2 \sum_{i=j+1}^{n} T_r \left\{ \frac{\partial w_i}{\partial \delta_{jf}} \left[G_i \ddot{w}_i^T + \sum_{k=1}^{m_i} \ddot{\delta}_{ik} D_{ik} w_i^T \right] \right\} + 2T_r \left\{ \left[\ddot{w}_j D_{jf} + w_j \sum_{k=1}^{m_i} \ddot{\delta}_{jk} C_{jkf} \right] w_j^T \right\}$$

<div align="right">(c.57)</div>

Substituting terms with $\ddot{\delta}$ in $\ddot{w}_j$, we have

$$2 \sum_{i=j+1}^{n} T_r \left\{ \frac{\partial w_i}{\partial \delta_{jf}} \left[G_i \sum_{h=1}^{i-1} \sum_{k=1}^{m_h} (w_h M_{hk}{}^h w_i \ddot{\delta}_{hk})^T + \sum_{k=1}^{m_i} \ddot{\delta}_{ik} D_{ik} w_i^T \right] \right\}$$

$$+ 2T_r \left\{ \sum_{h=1}^{j-1} \sum_{k=1}^{m_h} w_h M_{hk}{}^h w_i \ddot{\delta}_{hk} + w_j \sum_{k=1}^{m_j} \ddot{\delta}_{jk} C_{jkf} w_j^T \right\}$$

<div align="right">(c.58)</div>

Since

$$\sum_{i=j+1}^{n} \sum_{h=1}^{i-1} = \sum_{h=1}^{n-1} \sum_{i=max(h+1, j+1)}^{n}$$

<div align="right">(c.59)</div>

we can write (c.58) as

$$2 \sum_{h=1}^{n-1} T_r \left\{ \sum_{i=max(h+1, j+1)}^{n} \frac{\partial w_i}{\partial \delta_{jf}} \left[G_i \sum_{k=1}^{m_h} (w_h M_{hk}{}^h w_i \ddot{\delta}_{hk})^T \right] \right\} +$$

$$2 \sum_{i=j+1}^{n} T_r \left\{ \frac{\partial w_i}{\partial \delta_{jf}} \sum_{k=1}^{m_i} \ddot{\delta}_{ik} D_{ik} w_i^T \right\} + 2T_r \left\{ \sum_{h=1}^{j-1} \sum_{k=1}^{m_h} w_h M_{hk}{}^h w_i \ddot{\delta}_{hk} + w_j \sum_{k=1}^{m_j} \ddot{\delta}_{jk} C_{jkf} w_j^T \right\}$$

<div align="right">(c.60)</div>

The first part and the last part which satisfy $j = h = 1 \ldots n-1$ can be written as

<div align="center">129</div>

$$J_{jfhk} = 2T_r\left\{ \sum_{i=max(h+1,\,j+1)}^{n} \frac{\partial w_i}{\partial \delta_{jf}} G_i(w_h M_{hk}{}^h w_i)^T \right\} + 2T_r\{w_j C_{jkf} w_j^T\}$$

$$= 2T_r\left\{ \sum_{i=max(h+1,\,j+1)}^{n} w_j \frac{\partial E_j}{\partial \delta_{jf}}{}^j w_i G_i{}^h w_i{}^T M_{hk}^T w_h^T \right\} + 2T_r\{C_{jkf}\}$$

$$= 2T_r\{w_j M_{jf}{}^j \Phi_h M_{hk}^T w_h^T\} + 2T_r\{C_{jkf}\}$$

$$= 2T_r\{w_j M_{jf}{}^j \Phi_j M_{jk}^T w_j^T + C_{jkf}\} \qquad\qquad \text{(c.61)}$$

where

$$^j\Phi_h = \sum_{i=max(h+1,\,j+1)}^{n} {}^j w_i G_i{}^h w_i{}^T \qquad\qquad \text{(c.62)}$$

3) $h = n, j = 1 \ldots n-1$

$$2T_r\left\{ \frac{\partial w_n}{\partial \delta_{jf}} D_{nk} w_n^T \right\} = 2T_r\{w_j M_{jf}{}^j w_n D_{nk} w_n^T\} \qquad\qquad \text{(c.63)}$$

4) $j = 1 \ldots n-1, h = j+1 \ldots n-1$

$$2T_r\left\{ \sum_{i=max(h+1,\,j+1)}^{n} \frac{\partial w_i}{\partial \delta_{jf}} [G_i(w_h M_{hk}{}^h w_i)^T] \right\} + 2T_r\left\{ \frac{\partial w_h}{\partial \delta_{jf}} D_{hk} w_h^T \right\}$$

$$= 2T_r\left\{ w_j M_{jf}\left(\sum_{i=max(j+1,\,h+1)}^{n} {}^j w_i G_i{}^h w_i{}^T \right) M_{hk}^T w_h^T \right\} + 2T_r\{w_j M_{jf}{}^j w_h D_{hk} w_h^T\}$$

$$= 2T_r\{w_j M_{jf}{}^j \Phi_h M_{hk}^T w_h^T\} + 2T_r\{w_j M_{jf}{}^j w_h D_{hk} w_h^T\}$$

$$= 2T_r\{w_j M_{jf}({}^j \Phi_h M_{hk}^T + {}^j w_h D_{hk}) w_h^T\} \qquad\qquad \text{(c.64)}$$

Remaining Dynamics

$$R_1 = -2T_r\{u_1 Q_1\} + F_1 \tag{c.65}$$

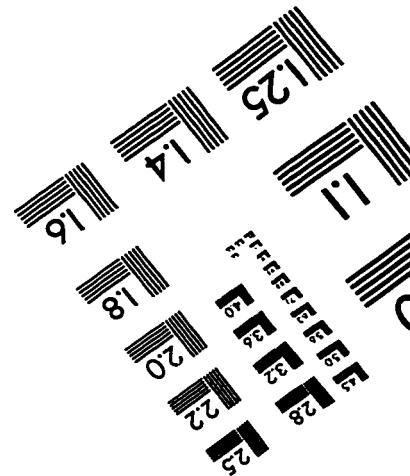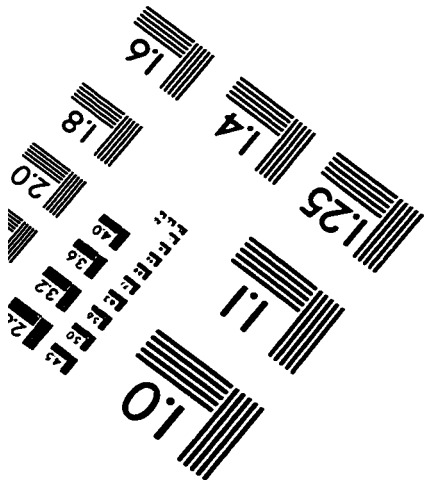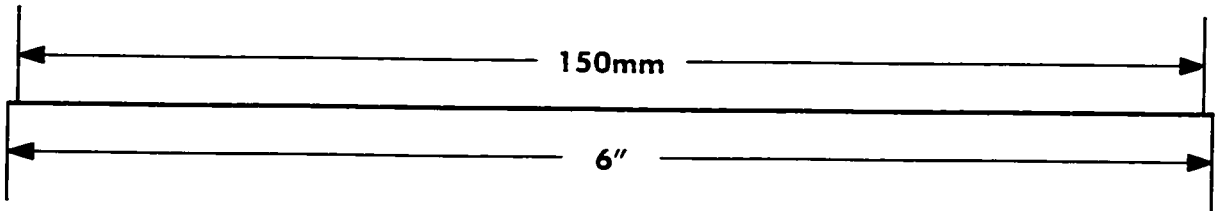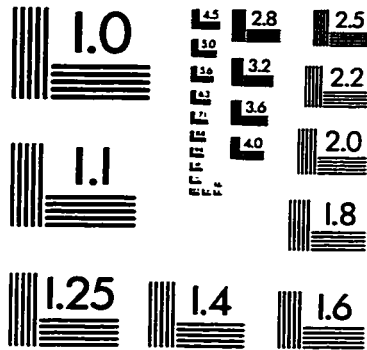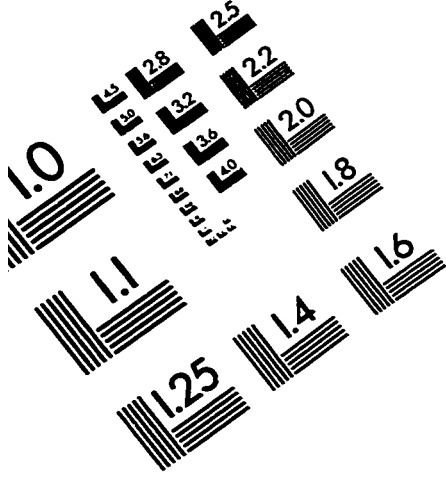$$R_j = -2T_r\{\hat{w}_{j-1} u_j Q_j\} + F_j \qquad j = 2\ldots6 \tag{c.66}$$

where

$$Q_n = G_n \ddot{w}_{vn}^T + 2\left(\sum_{k=1}^{m_n} \dot{\delta}_{nk} D_{nk}\right)\dot{w}_n^T \tag{c.67}$$

$$Q_j = G_j \ddot{w}_{vj}^T + 2\left(\sum_{k=1}^{m_j} \dot{\delta}_{jk} D_{jk}\right)\dot{w}_j^T + E_j A_{j+1} Q_{j+1} \tag{c.68}$$

$$R_{jf} = -2T_r\left\{w_j M_{jf} A_{j+1} Q_{j+1} + \left[\ddot{w}_{vj} D_{jf} + 2\dot{w}_j \sum_{k=1}^{m_i} \dot{\delta}_{jk} C_{jkf}\right]w_j^T\right\} - \delta_{jf} K_{jf} \tag{c.69}$$

1.0 1.1 1.25 1.4 1.6 1.8 2.0 2.2 2.5 2.8 3.2 3.6 4.0 4.5 5.0

150mm

6"

APPLIED IMAGE . Inc
1653 East Main Street
Rochester, NY 14609 USA
Phone: 716/482-0300
Fax: 716/288-5989